LOW LOSS OPTICAL WAVEGUIDES AND POLARIZATION SPLITTERS WITH OXIDIZED $Al_xGa_{1-x}As$ LAYERS

A THESIS

SUBMITTED TO THE DEPARTMENT OF PHYSICS

AND THE INSTITUTE OF ENGINEERING AND SCIENCE

OF BILKENT UNIVERSITY

IN PARTIAL FULFILLMENT OF THE REQUIREMENTS

FOR THE DEGREE OF

MASTER OF SCIENCE

by

Alpan Bek

August 1998

QC
661
.B45
1998

LOW LOSS OPTICAL WAVEGUIDES AND POLARIZATION SPLITTERS WITH OXIDIZED $Al_xGa_{1-x}As$ LAYERS

A THESIS
SUBMITTED TO THE DEPARTMENT OF PHYSICS
AND THE INSTITUTE OF ENGINEERING AND SCIENCE
OF BILKENT UNIVERSITY
IN PARTIAL FULFILLMENT OF THE REQUIREMENTS
FOR THE DEGREE OF
MASTER OF SCIENCE

Alpan BEK

by
Alpan Bek

August 1998

QC
661
.B45
1998

B 044005

I certify that I have read this thesis and that in my opinion it is fully adequate, in scope and in quality, as a dissertation for the degree of Master of Science.

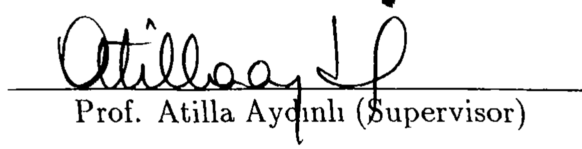

Prof. Atilla Aydınlı (Supervisor)

I certify that I have read this thesis and that in my opinion it is fully adequate, in scope and in quality, as a dissertation for the degree of Master of Science.

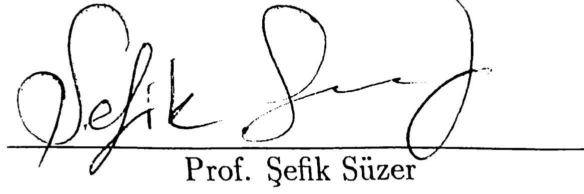

Prof. Şefik Süzer

I certify that I have read this thesis and that in my opinion it is fully adequate, in scope and in quality, as a dissertation for the degree of Master of Science.

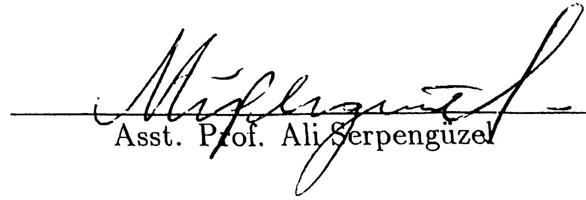

Asst. Prof. Ali Serpengüzel

Approved for the Institute of Engineering and Science:

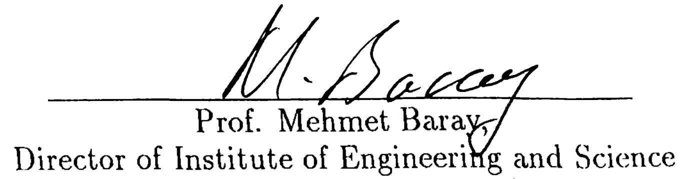

Prof. Mehmet Baray,
Director of Institute of Engineering and Science

Abstract

LOW LOSS OPTICAL WAVEGUIDES AND POLARIZATION SPLITTERS WITH OXIDIZED $Al_xGa_{1-x}As$ LAYERS

Alpan Bek
M. S. in Physics
Supervisor: Prof. Atilla Aydınlı
August 1998

Low propagation loss waveguides, operating at 1.55 μm optical wavelength, are fabricated utilizing oxidized $Al_xGa_{1-x}As$ layers. MBE grown multilayer semiconductor heterostructures are characterized before and after oxidation by ellipsometric techniques. In fabrication of optical waveguides, reactive ion etching method is used extensively. Loss measurements are performed, involving a fiber input-coupled laser source setup using Fabry-Perot resonance technique. Propagation loss of an AlGaAs based multilayer rib waveguide with oxidized $Al_xGa_{1-x}As$ top layer is observed to reduce from 6 dB/cm to as low as 1 dB/cm for TM and from 3.7 dB/cm to as low as 0.6 dB/cm for TE polarizations in the presence of metal electrodes on top of the rib. These results are compared with loss measurements on standard rib waveguides. Polarization splitters are also fabricated with the same material. Effect of the oxide layer on the polarization splitter's coupling length for TE and TM polarizations are measured. Polarization extinction ratios as high as 12.4 dB are obtained. Polarization extinction ratios are also attempted to be controlled by the use of electro-optic effect in

$Al_xGa_{1-x}As$ system. Only AC fields are found to be effective.

Keywords: Optical loss, waveguide, coupler, oxidation, reactive ion etching, ellipsometry, Fabry-Perot, polarization splitter

Özet

$Al_xGa_{1-x}As$ TABAKALARIN OKSİTLENMESİYLE GELİŞTİRİLEN DÜŞÜK KAYIPLI OPTİK DALGA KILAVUZLARI VE KUTUPLULUK AYRAÇLARI

Alpan Bek
Fizik Yüksek Lisans
Tez Yöneticisi: Prof. Atilla Aydınlı
Ağustos 1998

$Al_xGa_{1-x}As$ tabakaların oksitlenmesi metoduyla 1.55 μm dalgaboyunda çalışan, düşük optik kayıplı dalga-kılavuzları üretildi. Üretimde kullanılan MBE ile büyütülmüş çok tabakalı hetero-yapıların oksitlenmeden önceki ve sonraki özellikleri elipsometrik yöntemlerle ölçüldü. Optik dalga-kılavuzlarının üretim aşamasında, büyük ölçüde etkin iyon aşındırıcıdan yararlanıldı. Optik kayıp değerleri, optik-lif çiftleyicili lazer kaynağı kullanılan bir deney düzeneğiyle Fabry-Perot çınlamaları gözlemlenerek bulundu. Metal elektrotla kaplı, oksitlenmiş $Al_xGa_{1-x}As$ üst tabakalı AlGaAs çok tabaka tabanlı bir optik dalga-kılavuzunda optik kaybın; TM kutuplu optik alanlar için 6 dB/cm değerinden 1 dB/cm, TE kutuplu optik alanlar için 3.7 dB/cm değerinden 0.6 dB/cm kadar düşük değerlere indiği saptandı. Bu sonuçlar standart yapıdaki dalga kılavuzlarının kayıp ölçümlerinden elde edilenlerle karşılaştırıldı. Aynı malzeme ile kutupluluk ayırıcılar da üretildi. Oksit tabakanın TE ve TM kutupları için çiftlenme uzunluğu üzerindeki etkileri ölçüldü. 12.4 dB kadar yüksek sönüm oranları elde edildi. Elektro-optik etki sayesinde kutupluluk ayrım uzunlukları voltaj

uygulanarak yönetilmeye çalışıldı. Yalnızca AC alanların etkin olduğu gözlendi.

Anahtar sözcükler: Optik kayıp, dalga-kılavuzu, çiftleyici, oksitlenme, etkin iyon aşındırma, elipsometre, Fabry-Perot, kutupluluk ayırıcı

Acknowledgement

I would like to express my deepest gratitude to Prof. Atilla Aydınlı for his supervision in research, encouragement, understanding, and friendship throughout the entire work. My special thanks go to Prof. Nadir Dağlı for supplying financial aid for laboratory facilities, helpful suggestions on many aspects of this work and hospitality. I also would like to thank Prof. Ekmel Özbay for providing necessary motivation during the early periods of this project. My thanks go to Prof. Cemal Yalabık for providing moral support and obtaining financial support for my travel abroad.

I would like to address my thanks to Baki Açıkel for his help in fabrication, Dr. Y. T. Byun for his help in wet etch characterization and measurements, and Dr. Andrea Fiore, Dr. Ali Shakouri, Dr. Ceyhun Bulutay and Cem Öztürk for the fruitful discussions on various subjects and computational aid. I also would like to thank Mr. James Champlain and Mr. Ryan Naone for the MBE growth of the structures.

Many thanks to my dear friends Koray Atasoy, Erol Sağol, Arıkan Açar, Ersin Keçecioğlu, Kaan Güven, Mete Atatüre, Hakan Fenderya, and Burak Temelkuran for being who they are and meaning what they mean to me.

It is my pleasure to dedicate this work to the warmest love of my family and to the lovely memory of my grandmother...

This work is supported by a NATO CRG grant and NSF Division of International Programs.

Contents

Abstract i

Özet i

Acknowledgement i

Contents i

List of Figures iii

List of Tables vi

1 Introduction 1

1.1 Optical Integrated Circuits 1

1.2 Reducing Excess Propagation Loss and its Applications 3

2 Theory and Design 5

2.1 Single Mode Waveguide 5

2.2 Multilayer Waveguide Structure 14

2.3 Optical Loss 20

2.3.1 Loss Mechanisms 21

2.3.2 Loss Characterization Techniques 23

2.3.3 Simulations of Loss Due to Metal Overlayer 25

2.4 Low Loss Waveguide Design 28

2.5 Polarization Splitter 32

3 Fabrication **41**

3.1 Epitaxial Growth 41
3.2 Sample Cleaning 42
3.3 Photolithography 42
3.4 Wet Etching 43
3.5 Reactive Ion Etching (RIE) 46
3.6 Oxidation of $Al_{0.98}Ga_{0.02}As$ 56
3.7 Metal Deposition 56
3.8 Lift-off 58

4 Characterization and Measurements **60**

4.1 Characterization 60
4.1.1 Spectroscopic Ellipsometry 60
4.1.2 Oxide Characterization 64
4.1.3 RIE Depth Profiling 69
4.2 Measurements 70
4.2.1 Optical Propagation Loss Measurements 70
4.2.2 Characterization of Polarization Splitters 77
4.2.3 AC and DC Bias Measurements 82

5 Conclusions **85**

List of Figures

2.1 The Slab Waveguide 6

2.2 The Symmetric Slab Waveguide Modes 9

2.3 The Rib Waveguide 12

2.4 The Effective Index Calculation Steps 12

2.5 Field Distribution of Zeroth and First Order Modes in the y-direction 13

2.6 Dependence of Confinement on Rib Width 14

2.7 The Four Layer Rib Waveguide 15

2.8 Confinement of the Optical Field Under the Rib 16

2.9 Metal Coated Four Layer Rib Waveguide 17

2.10 Dependence of Refractive Index on Aluminum Composition (x) of $Al_xGa_{1-x}As$ at $\lambda = 1.55\ \mu m$ 17

2.11 $Al_xGa_{1-x}As/Al_yGa_{1-y}As$ Multilayers 18

2.12 Single Mode AlGaAs Rib Waveguide 19

2.13 Mode Calculation with BPM 20

2.14 The Vertical Field Distribution in the Absence of a Metal Layer . 26

2.15 The Vertical Field Distribution in the Presence of a Metal Layer . 27

2.16 Calculated Loss as a Function of Top Cladding Thickness 27

2.17 Loss Calculation-1 28

2.18 Loss Calculation-2 30

2.19 Final Design of WG1 Waveguide 31

2.20 Final Design of WG2 Waveguide 31

2.21 Final Design of WG3 Waveguide 32

2.22 Electic Field Distribution of the Odd and Even Modes of a Polarization Splitter . . . 33
2.23 Waveguide Coupler Polarization Splitter . . . 34
2.24 Coupling Ratio $L_{c_{TM}}/L_{c_{TE}}$ versus Core Layer Thickness . . . 35
2.25 Coupling Ratio versus Rib Width . . . 36
2.26 Coupling Ratio versus Top Cladding Thickness d_t as in Fig. 2.12 . 36
2.27 Coupling Ratio versus Δn . . . 37
2.28 Multiple Coupling of TE Mode between the two Waveguides . . . 38
2.29 Coupling of TE Polarized Light . . . 39
2.30 Coupling of TM Polarized Light . . . 40
3.1 Wet Etched Surface of AlAs Crystal in Citric Acid Solution . . . 45
3.2 Wet Etched Surface of AlAs Crystal in Hydrochloric Acid Solution 45
3.3 Wet Etched Surface of AlAs Crystal in Phosphoric Acid Solution . 45
3.4 Components of RIE System . . . 47
3.5 Photoresist Loss during the Etch 48
3.6 Rounded Photoresist Profile . . . 48
3.7 Sputtered Photoresist . . . 49
3.8 Penetration of Energetic Ions 49
3.9 Wriggled Sidewalls . . . 49
3.10 Photoresist Covered with Ti prior to RIE of the Rib . . . 50
3.11 Grass Formation . . . 51
3.12 Rough Etched Surface . . . 51
3.13 Polymer Deposition during RIE . . . 52
3.14 RIE Etched Waveguide Profile . . . 53
3.15 RIE Etched Waveguide Sidewalls . . . 53
3.16 Simulation of RIE Interference Pattern for WG1 . . . 54
3.17 Simulation of RIE Interference Pattern for WG3 . . . 54
3.18 Monitored RIE Interference Pattern for WG3 55
3.19 Photoresist Profile I . . . 57
3.20 Photoresist Profile II . . . 57
3.21 E-beam Evaporator . . . 58

3.22 Schematic of Fabrication Steps 59
4.1 The Ellipsometer Instrument 61
4.2 Ellipsometric Measurement of the AlAs Wafer 63
4.3 Ellipsometric Measurement of the Thick Top-cladding Wafer . . . 64
4.4 Microscope View of AlAs Wafer Edge Oxidized for 20 Minutes . . 66
4.5 Microscope View of AlAs Wafer Edge Oxidized for 60 Minutes . . 66
4.6 Lateral Oxidation Depth versus Time 67
4.7 Refractive Index of Oxidized AlAs 68
4.8 The Zeroth Order Mode of AlAs Waveguide 72
4.9 The First Order Mode of AlAs Waveguide 72
4.10 Loss Measurement Setup 73
4.11 Single Mode Waveguide Fabry-Perot Resonances 74
4.12 Double Mode Waveguide Fabry-Perot Resonances 74
4.13 SEM Picture of a BCB Covered $Al_{0.98}Ga_{0.02}As$ Waveguide Rib . . 75
4.14 The Loss Coefficients and Facet Reflectivities of WG1 and WG2 Waveguides 76
4.15 The Loss Coefficient and Facet Reflectivity of WG3 Waveguides . 77
4.16 Optical Field Output at the Left Output Port 79
4.17 Optical Field Half-and-half at Both Output Ports 79
4.18 Optical Field Output at the Right Output Port 79
4.19 Coupling Ratio of WG2 Polarization Splitter for gap = $3.00\mu m$ 80
4.20 Coupling Ratio of WG2 Polarization Splitter for gap = $3.25\mu m$ 81
4.21 Coupling Lengths of WG2 Polarization Splitters 82
4.22 TE Modulation at One Output Port of the Waveguide 84
4.23 TE Modulation at the Other Output Port of the Waveguide . . . 84

List of Tables

4.1 The Ellipsometric Data of WG1 wafer 64

4.2 The Ellipsometric Data of WG3 wafer 65

4.3 Ellipsometric Measured Thicknesses of AlAs 67

4.4 Cauchy Coefficients for AlOx 68

4.5 Coupling Length Ratios of WG2 Determined by Experiment, Effective Index Method, and BPM 81

Chapter 1

Introduction

The idea of optical signal transmission and processing has developed after a coherent light source, the laser, was developed at 1960's. It was possible to transmit laser beams through the air, yet inefficiently, because of the unpredictable changes in ambient conditions. It was also possible to manipulate laser beams by the usual optical components such as lenses, prisms, and mirrors. Making use of such systems for practical purposes were expensive and hardly stable. The concept of integrated optics[1–5] emerged, replacing air with the waveguiding optical fibers and conventional electrical systems with the optical integrated circuits. The advantages of optical integrated circuits over electrical circuitry would be immunity from electromagnetic interference, freedom from electrical short circuits or ground loops, safety in combustive environment, security from monitoring, low-loss operation, low power consumption, improved reliability, large bandwidth, small size, and immunity to mechanical vibration.

1.1 Optical Integrated Circuits

Optical integrated circuits can be designed in two major forms. Hybrid integration forms[6] are composed of two or more different substrate materials bonded to each other to optimize performance of different devices. Monolithic integration of optical integrated circuits require an optically active material,

usually one of the following direct band-gap semiconductors like GaAs, AlGaAs, GaAsP, GaInAs and other III-IV and II-VI semiconductors. These materials offer plenty of applications in various aspects of integrated optics. High-speed low drive-voltage modulators[7] and switches, are some of these. In optical devices, ternary and quaternary compounds are particularly useful because the refractive index of the material can be tuned by altering the relative compositions of elements.

Ever since the fiber-optic technology has come out with the development of high bandwidth, low-loss, single-mode fibers for optical telecommunication, the need for suitable integrated optical element was born, to efficiently couple to the optical field from these fibers. The evolution of rib, strip, and channel optical waveguides has began with the extensive studies of refractive index profile, waveguide dispersion, and propagation loss on Ti-diffused $LiNbO_3$. However, since the monolithic integration was possible only on the optically active substrates, the studies have extended to the implementation of $Al_xGa_{1-x}As$/GaAs systems. The fact that $Al_xGa_{1-x}As$ fabrication technology is already well developed, makes its use advantageous. Also this system has a unique property that the lattice constants of GaAs and AlAs are very close (5.654 and 5.660 Å respectively[41]). Thus the layers of $Al_xGa_{1-x}As$ with greatly different Al concentrations can be epitaxially grown on top of each other with little strain. The possibility of light generation and detection in $Al_xGa_{1-x}As$ systems is another advantage. However, all the named advantages of $Al_xGa_{1-x}As$ systems were screened due to high insertion loss. Significant progress in fabrication techniques has reduced the effect of high insertion loss to the $LiNbO_3$ levels. The other difficulty in the use of AlGaAs substrate has been the propagation loss. While propagation loss due to scattering from imperfections in the as grown material and roughness introduced during fabrication process (such as sidewall roughness) have been minimized by superior growth and fabrication techniques, polarization dependent propagation loss due to presence of a lossy medium (such as a metal electrode) in close proximity of the propagating light has remained as a problem. Metal electrodes are almost always present as a lossy media

in active devices to make use of the bulk electro-optic effect.[8] Furthermore, this loss turns out to be polarization dependent due to lower symmetry of the heterostructures as the device medium. TE and TM modes of propagation experience different boundary conditions in satisfying Maxwell's equations, hence result in polarization dependent loss and polarization dependent device operation. While polarization dependent optical loss due to metal electrodes has been used to fabricate various types of polarization dependent devices, it also caused a major problem in the progress of polarization independent devices. Thus, in trying to achieve active devices with high speed operation, excess polarization dependent optical propagation loss becomes a major problem and needs a solution.

1.2 Reducing Excess Propagation Loss and its Applications

A significant part of this work was devoted to reduce the metal electrode induced optical propagation loss for polarization independent device applications of AlGaAs based integrated optical circuits. We have followed two methodologies to achieve our goal.

One way to reduce the optical loss is to increase the semiconductor cladding layer thickness under the metal electrodes. Although application of this method results in significant reduction of the electrode loss, it also requires excessive amount of epitaxial growth time, and excess applied voltage. Moreover, it causes planarization problems during fabrication.

Another possibility is to introduce a low index material under the metal electrode to effectively suppress the optical field before it reaches the electrode. Thus, oxidized $Al_xGa_{1-x}As$ layers (AlOx) were introduced into $Al_yGa_{1-y}As/Al_zGa_{1-z}As$ optical waveguides with metal electrodes.

Prior to fabrication and measurement of waveguides with AlOx layers, the index and thickness measurements of AlOx material were done by spectroscopic ellipsometry.

AlOx has recently been used extensively in vertical cavity surface-emitting laser (VCSEL). Also, latest results in GaAs based metal-oxide-semiconductor field effect transistor (MOSFET) with thin AlOx layers offer hope of applying voltage to active optical waveguide devices. Therefore, low-loss directional coupler polarization splitters are fabricated for characterization of the effects of the oxide layer in a polarization dependent device. The coupling ratios as a function of coupler gaps and polarization extinction ratios were measured. The coupling lengths of these splitters were determined from the measurement data. Both effective index calculations and simulations using a 3-D semi-vectorial finite difference algorithm were done which showed good agreement with the measured data. The application of DC bias to further tune the polarization extinction ratio was found to be ineffective. On the other hand, AC bias measurements resulted in a modest response from the coupler in a limited range of frequencies.

In the following chapters, the theory of waveguiding in semiconductor based substrate materials using effective index analysis is summarized. A model single mode waveguide design with the appropriate properties is established. The simulations of expected behavior of this model and expected behavior of application to polarization splitters, the detailed description of the fabrication steps, the measurement methods, measured loss reduction and polarization splitting results are presented.

Chapter 2

Theory and Design

The basic idea of optical waveguides is to confine and propagate light in dielectrics or semiconductors, as opposed to free space optics.[22] This can be managed by handling light in properly designed geometries of semiconductor (multilayer in general) structures. Propagation of light is not unique in a cavity, but varies with polarization and spatial distribution of the field components due to geometry and refractive index of the media. At a given wavelength, an optical waveguide may support one or more modes of light. Single mode operation and low propagation loss are the main characteristics of waveguides, that are desired for most of the active and passive waveguide applications in photonic integrated circuits (PIC). Therefore, the determination of parameters to assure these properties in guided wave optics becomes essential. Our design is based on the calculations of the necessary conditions for single mode operation by the use of effective index approach in waveguide theory.

2.1 Single Mode Waveguide

The principles that govern the behavior of light in optical waveguides, stem from well-known Maxwell's equations under appropriate boundary conditions.

As an example, let us consider a structure that is composed of three different layers, stacked together on top of each other, such that the middle layer has the

highest refractive index, and the most of the field intensity is confined in the middle (core) layer due to total internal reflections. In this geometry, the top layer is called the cladding and the bottom layer is called the substrate. This structure is called a *slab waveguide.*

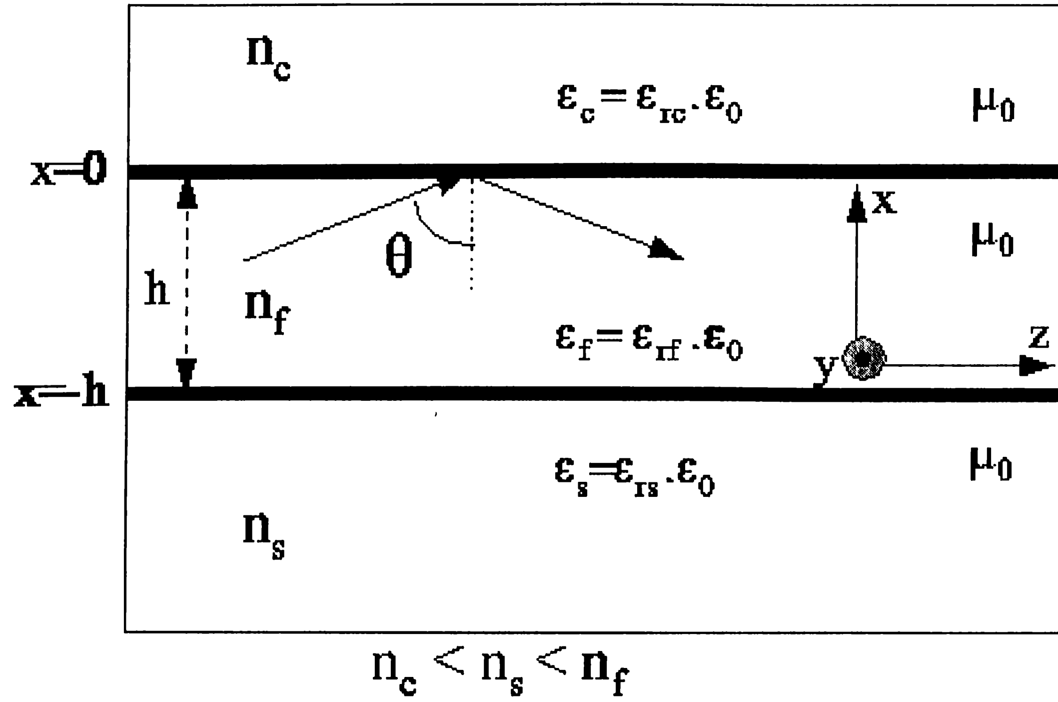

Figure 2.1: The Slab Waveguide

Maxwell's Equations for isotropic, lossless, dielectric medium are,

$$\vec{\nabla} \times \vec{E} = -\mu_0 \frac{\partial \vec{H}}{\partial t} \qquad \vec{\nabla} \times \vec{H} = \epsilon_0 n^2 \frac{\partial \vec{E}}{\partial t} \tag{2.1}$$

where ϵ_0 and μ_0 are the dielectric permittivity and magnetic permeability of the free space respectively and n is the refractive index of the medium. The scalar wave equation for the field then turns out to be

$$\nabla^2 \psi + k_0^2 n^2 \psi = 0 \tag{2.2}$$

where ψ represents any of the field components $\vec{E}$ or $\vec{H}$. Choosing z-direction as the propagation direction of the field, one can denote the electromagnetic field as

$$\vec{E} = \vec{E}(x,y)e^{i(\omega t-\beta t)} \qquad \vec{H} = \vec{H}(x,y)e^{i(\omega t-\beta t)} \tag{2.3}$$

β representing the propagation constant in z-direction and ω representing the angular frequency $w = \frac{2\pi c}{\lambda}$. Here, λ is the wavelength of the field and $c = \frac{1}{\sqrt{\mu_0 \epsilon_0}}$ is the speed of light in free space. One should note that in all regions, propagation constant β is the same due to phase matching condition and the fields are independent of y due to symmetry along y-direction. Keeping that in mind, we can substitute these forms of field into Eqs. 2.3. The operators $\frac{\partial}{\partial t}$, $\frac{\partial}{\partial z}$ and $\frac{\partial}{\partial y}$ then become equivalent to $i\omega$, $-i\beta$ and 0 respectively. There comes the striking fact that Eqs. 2.1 yield two *modes* of electromagnetic field with mutually orthogonal polarizations. The one with the field components E_y, H_x and H_z is called the TE mode and the one with the field components E_x, H_y and E_z is called the TM mode. The reason we refer to two different sets of field components is that, their wave equations, are coupled to each other within the same set, while they are totally independent of the other set's variables :

$$\frac{\partial^2 E_y}{\partial x^2} + (k_0^2 n_i^2 - \beta^2)E_y = 0 \qquad H_x = -\frac{\beta E_y}{\omega \mu_0} \qquad H_z = -\frac{1}{i\omega\mu_0}\frac{\partial E_y}{\partial x} \tag{2.4}$$

$$\frac{\partial^2 H_y}{\partial x^2} + (k_0^2 n_i^2 - \beta^2)H_y = 0 \qquad E_x = -\frac{\beta H_y}{\omega \epsilon_0 n^2} \qquad E_z = \frac{1}{i\omega\epsilon_0 n^2}\frac{\partial H_y}{\partial x} \tag{2.5}$$

The scalar wave equation for E_y gives us a clue about the form of field component E_y :

$$\frac{\partial^2 E_y}{\partial x^2} + \frac{\partial^2 E_y}{\partial z^2} + k_0^2 n_i^2 E_y = 0$$

Assuming $E_y(x,z) = Ah(k_x,x)h(k_z,z)$, where h is a harmonic function like $e^{\alpha x}$ and α is an arbitrary propagation constant, then the general form of E_y becomes,

$$
\begin{aligned}
E_y &= Ae^{-\alpha_c x}e^{-ik_{zc}z} && x > 0 \\
E_y &= (Be^{-ik_x x} + Ce^{ik_x x})e^{-ik_{zf}z} && -h < x < 0 \\
E_y &= De^{\alpha_s(x+h)}e^{ik_{zs}z} && x < -h
\end{aligned} \tag{2.6}
$$

where $k_{zc} = k_{zf} = k_{zs} = \beta$ due to phase matching boundary conditions as mentioned before. Putting this form into Eq. 2.4 we obtain a set of equations relating α_i to n_i as follows :

$$
\begin{aligned}
-\alpha_c^2 + \beta^2 &= k_0^2 n_c^2 \\
k_x^2 + \beta^2 &= k_0^2 n_f^2 \\
-\alpha_s^2 + \beta^2 &= k_0^2 n_s^2
\end{aligned} \tag{2.7}
$$

By the same procedure we can find H_z to be;

$$
\begin{aligned}
H_z &= \frac{\alpha_c}{i\omega\mu_0}Ae^{-\alpha_c x} && x > 0 \\
H_z &= \frac{k_x}{\omega\mu_0}(Be^{-ik_x x} - Ce^{ik_x x}) && -h < x < 0 \\
H_z &= -\frac{\alpha_s}{i\omega\mu_0}De^{\alpha_s(x+h)} && x < -h
\end{aligned} \tag{2.8}
$$

and imposing the necessary boundary conditions we can obtain the eigenvalue equation :

$$
\tan k_x h = \frac{\alpha_c + \alpha_s}{k_x\left(1 - \frac{\alpha_s\alpha_c}{k_x^2}\right)} \tag{2.9}
$$

Remembering that, until here, we have made use of only the first set of components for TE polarization, we can extend this approach to the second set of field components for TM polarization and obtain yet another eigenvalue equation as follows :

$$
\tan k_x h = \frac{\frac{n_f^2}{n_s^2}\frac{\alpha_s}{k_x} + \frac{n_f^2}{n_c^2}\frac{\alpha_c}{k_x}}{1 - \left(\frac{n_f^2}{n_s^2}\frac{\alpha_s}{k_x}\right)\left(\frac{n_f^2}{n_c^2}\frac{\alpha_c}{k_x}\right)} \tag{2.10}
$$

Now, we have all the necessary parameters to determine the number of modes that a slab waveguide can support. For this, let us investigate two possible geometrical configurations. First, let us take a *symmetric* slab guide such that $n_c = n_s$ and

$\alpha_c = \alpha_s = \alpha$. Taking the sign of the field in the substrate to be negative for odd (sine) modes and positive for even (cosine) modes, the eigenvalue equations for TE and TM modes become :

$$\tan\left(\frac{k_x h}{2}\right) = \begin{cases} \frac{\alpha}{k_x} & \text{for even modes} \\ -\frac{k_x}{\alpha} & \text{for odd modes} \end{cases} \tag{2.11}$$

and

$$\tan\left(\frac{k_x h}{2}\right) = \begin{cases} \left(\frac{n_f}{n_s}\right)^2 \frac{\alpha}{k_x} & \text{for even modes} \\ -\left(\frac{n_s}{n_f}\right)^2 \frac{k_x}{\alpha} & \text{for odd modes} \end{cases} \tag{2.12}$$

respectively. Using the Eqs. 2.7 and 2.9 for TE polarization, we finally arrive at the most significant relation in determination of number of modes as,

$$\left(\frac{k_x h}{2}\right)^2 + \left(\frac{\alpha_x h}{2}\right)^2 = \frac{k_0^2 h^2}{4}(n_f^2 - n_c^2) \tag{2.13}$$

The number of guided modes in the symmetric slab waveguide, depends on the quantity on the right-hand side of Eq. 2.13.

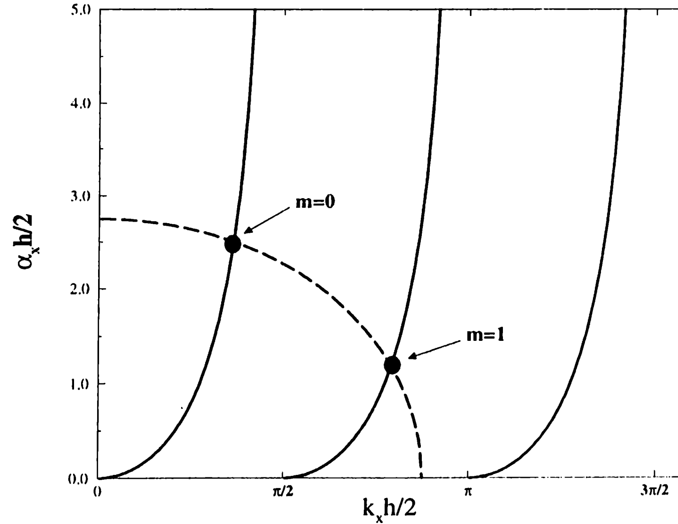

Figure 2.2: The Symmetric Slab Waveguide Modes

The circle in figure 2.2 shows this quantity, where the other curves are the solutions of the eigenvalue equation. The curves starting from 0 and the integer

multiples of π represent the symmetric modes where the curves starting from half integer multiples of π represent the antisymmetric modes. The modes that a certain symmetric slab can support, are the modes that the circle intersects as in the Fig. 2.2.

The propagation constants of guided modes lie in the interval $k_0 n_s < \beta < k_0 n_f$. If we normalize β to k_0, then we have the relation $n_s < n_{eff} < n_f$, where $n_{eff} = \frac{\beta}{k_0}$. This index is called *the effective index*. The guided modes' propagation constants behave as if they were propagating in a medium, having refractive indices equal to their effective indices. Having developed the necessary relations for a symmetric slab waveguides, we can generalize this formalism to *asymmetric* slab waveguides as well. For this aim, an asymmetry parameter is defined,

$$a = \frac{n_s^2 - n_c^2}{n_f^2 - n_s^2} \tag{2.14}$$

such that this parameter takes values,

$$a = \begin{cases} 0 & \text{for symmetric slab waveguides} \\ 0 < a < \infty & \text{for asymmetric slab waveguides} \end{cases} \tag{2.15}$$

For the numerical calculation purposes, it is beneficial to introduce the normalized thickness V and guide index b as follows,

$$V = k_0 h \sqrt{n_f^2 - n_s^2} \tag{2.16}$$

and

$$b = \frac{n_e f f^2 - n_s^2}{n_f^2 - n_s^2} \tag{2.17}$$

so as to get to the normalized eigenvalue equation for TE polarization :

$$V\sqrt{1-b} = \tan^{-1}\sqrt{\frac{a+b}{1-b}} + \tan^{-1}\sqrt{\frac{b}{1-b}} + m\pi \tag{2.18}$$

by the use of Eqs. 2.9, 2.14, 2.16 and 2.17. The normalized eigenvalue equation for TM polarization can be found by following the same kind of analysis :

$$V\sqrt{1-b} = \tan^{-1}\frac{c+1}{c-a}\sqrt{\frac{a+b}{1-b}} + \tan^{-1}\frac{c+1}{c}\sqrt{\frac{b}{1-b}} + m\pi \qquad (2.19)$$

where c is defined as $c = \frac{n_s^2}{n_f^2 - n_s^2}$. In Eqs. 2.18 and 2.19, m denotes an integer corresponding to the mode order and comes as a natural consequence of the periodicity of the normalized eigenvalue equations.

The generalization of the preceding mode calculations to 3-D geometries is called *the effective index method.* Let us investigate the following waveguide structure, which is called a *rib waveguide* (Fig. 2.3). While the material index profile in the vertical direction provides vertical confinement, the rib etched into the top layer breaks lateral symmetry and introduces horizontal confinement due to an effective index experienced by the field.

The effective index method calculates this effective index experienced by the propagating light by first dividing the rib waveguide geometry vertically along the symmetry lines (Fig. 2.3). Then the effective index of the resulting slab waveguides are solved. The resulting effective indices for the slab waveguides, then form a 3 layer slab waveguide, whose effective index is the desired result. Effective indices for TE and TM modes are calculated separately as they satisfy different boundary conditions. If the TM(TE) effective index is desired, one calculates the TM(TE) effective in the first step and then uses these effective indices in forming the final slab waveguide structure but solves for the TE(TM) set of equations (Fig. 2.4).
After having calculated the effective indices, the single mode conditions for symmetric and asymmetric geometries can be stated as :

$$\begin{aligned} &0 < V < \pi && \text{for symmetric waveguides} \\ &\tan^{-1}(\sqrt{a}) < V < \tan^{-1}(\sqrt{a}) + \pi && \text{for asymmetric waveguides} \end{aligned} \qquad (2.20)$$

The field distribution of the guided modes in rib waveguides differ from the slab waveguides. The lateral confinement of the light due to the physical step of the rib results the propagation of light possible only in z-direction and the

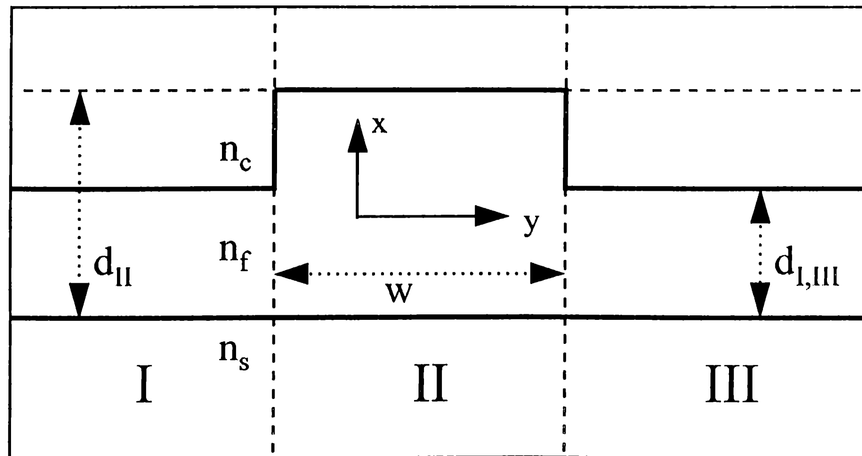

Figure 2.3: The Rib Waveguide

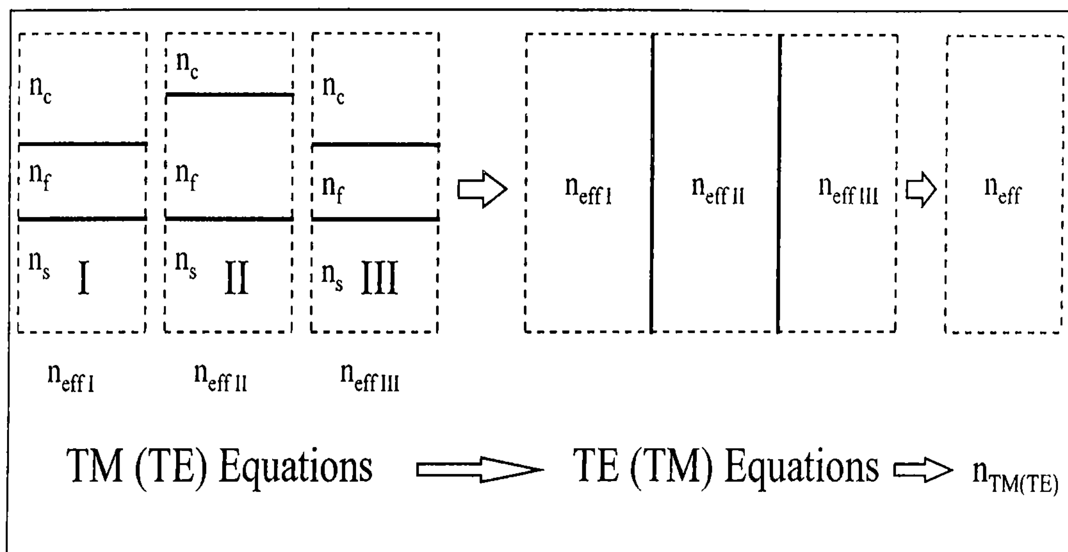

Figure 2.4: The Effective Index Calculation Steps

maximum intensity of field lies just under the rib. The waveguide structures, that do not obey the conditions of Eq. 2.20, may not support any propagating modes or support more than one mode. In the first case, the waveguide does not support any modes, meaning that light radiates out of the waveguide, where

in the second case, supports more than one mode and is called a multimode waveguide. The propagating modes of light in those waveguides start from the zeroth order ($m = 0$, TE_0 or TM_0) mode and continue to first, second order modes ($m = 1 : TE_1, TM_1$; $m = 2 : TE_2, TM_2$) and so on. A demonstration of this situation is given in Fig. 2.5.

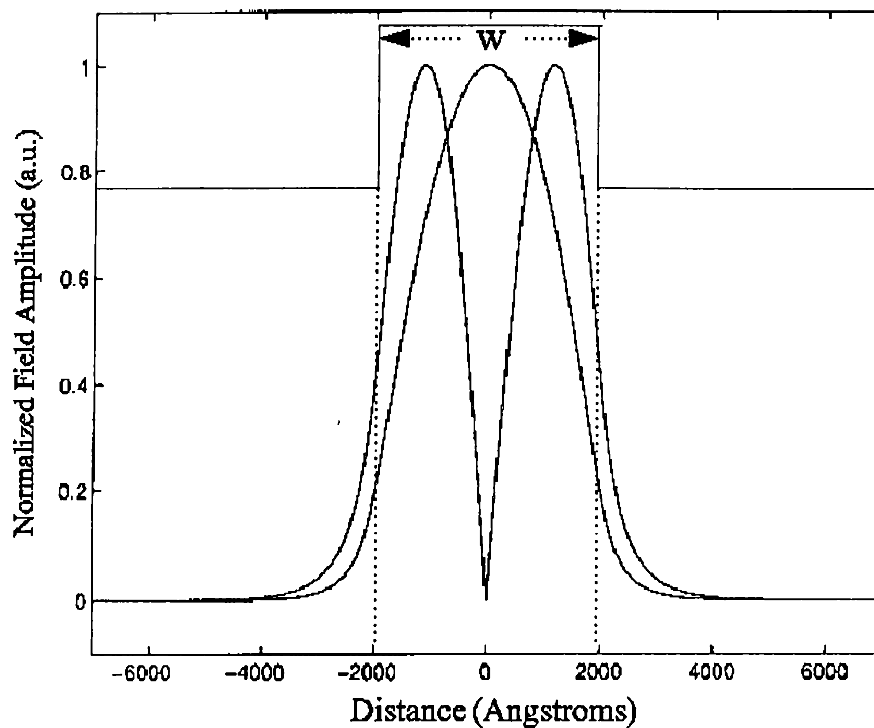

Figure 2.5: Field Distribution of Zeroth and First Order Modes in the y-direction

There is yet another property concerning the confinement of the optical mode in the waveguide. The confinement strongly depends on the parameter w (width of the rib). This effect is demonstrated in Fig. 2.6. The full width half maximum (FWHM) of the field intensity narrows down, as a consequence of increasing width of the rib. Hence the confinement factor is larger in the sharper peaks.

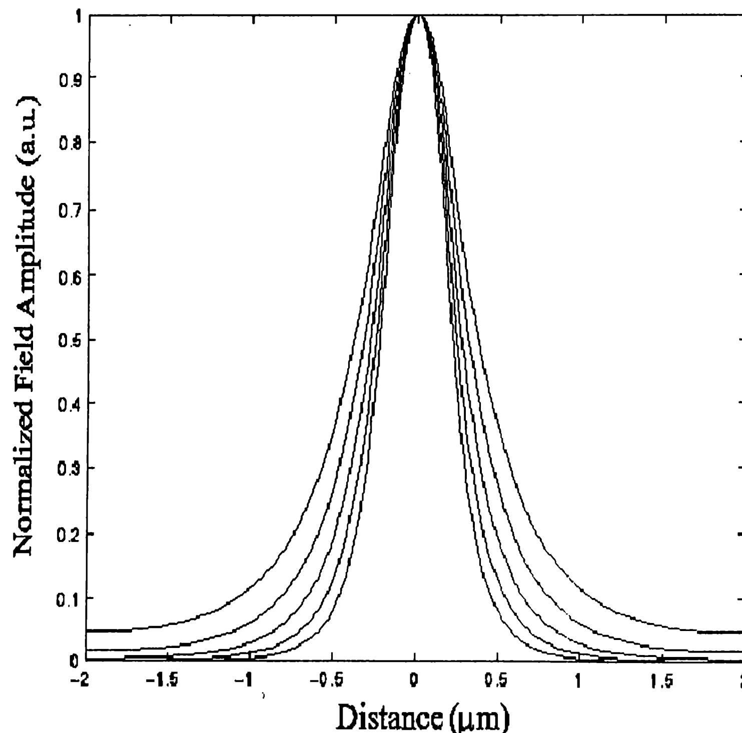

Figure 2.6: Dependence of Confinement on Rib Width
FWHM of first order modes in y-direction narrow as w decreases.

2.2 Multilayer Waveguide Structure

In the fabrication of three layer rib waveguides, generally the top cladding layer is taken to be the air. This makes a sharp index step. Therefore most of the mode field is expanded into the rib itself. However, as the light is confined to the top layer below air, the field extending to the surface experiences loss due to surface roughness as well as loss due to strong interaction with any nearby lossy medium such as a metal electrode. Because of this reason, it is preferable to develop a more sophisticated structure. A four layer rib waveguide gives the advantage of minimizing loss of optical field, while the mathematical formulations are very similar to the three layer rib waveguide analysis. Fig. 2.7 sketches a four layer rib waveguide with the uppermost cladding layer being the air. Fig. 2.8 demonstrates schematically how the field is distributed in the rib waveguide structure.

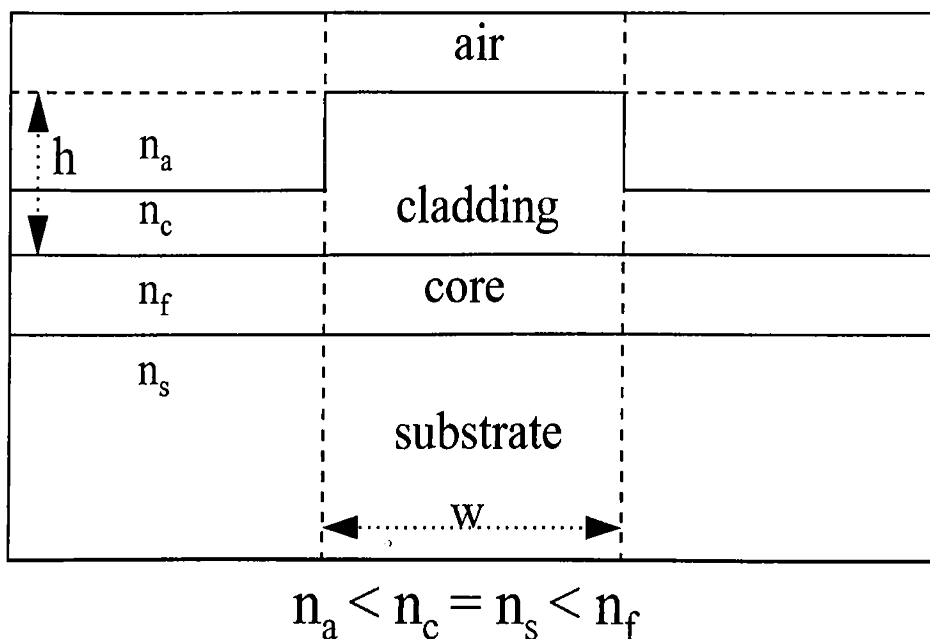

Figure 2.7: The Four Layer Rib Waveguide

The top cladding introduced above the core allows for space for the optical field to quench further before significant optical power reaches to the air interface resulting in a structure less susceptible to surface loss mechanisms.[20] As active devices require metal electrodes in the vicinity of the optical field to control the device electrically through the electro-optic effect, the four layer structure provides a further advantage for metal electrode induced loss, keeping in mind that metals have large absorption in the wavelengths of the interest for telecommunication. Most of the photonic integrated circuits are designed to operate at the wavelengths of fiber-optic communication for compatibility. These wavelengths are chosen to be 1.3 μm and 1.55 μm for maintaining minimum dispersion and minimum loss, respectively. A major aim in this work is to develop a method to prevent the metal induced loss in a metal coated rib waveguide structure as in Fig. 2.9.

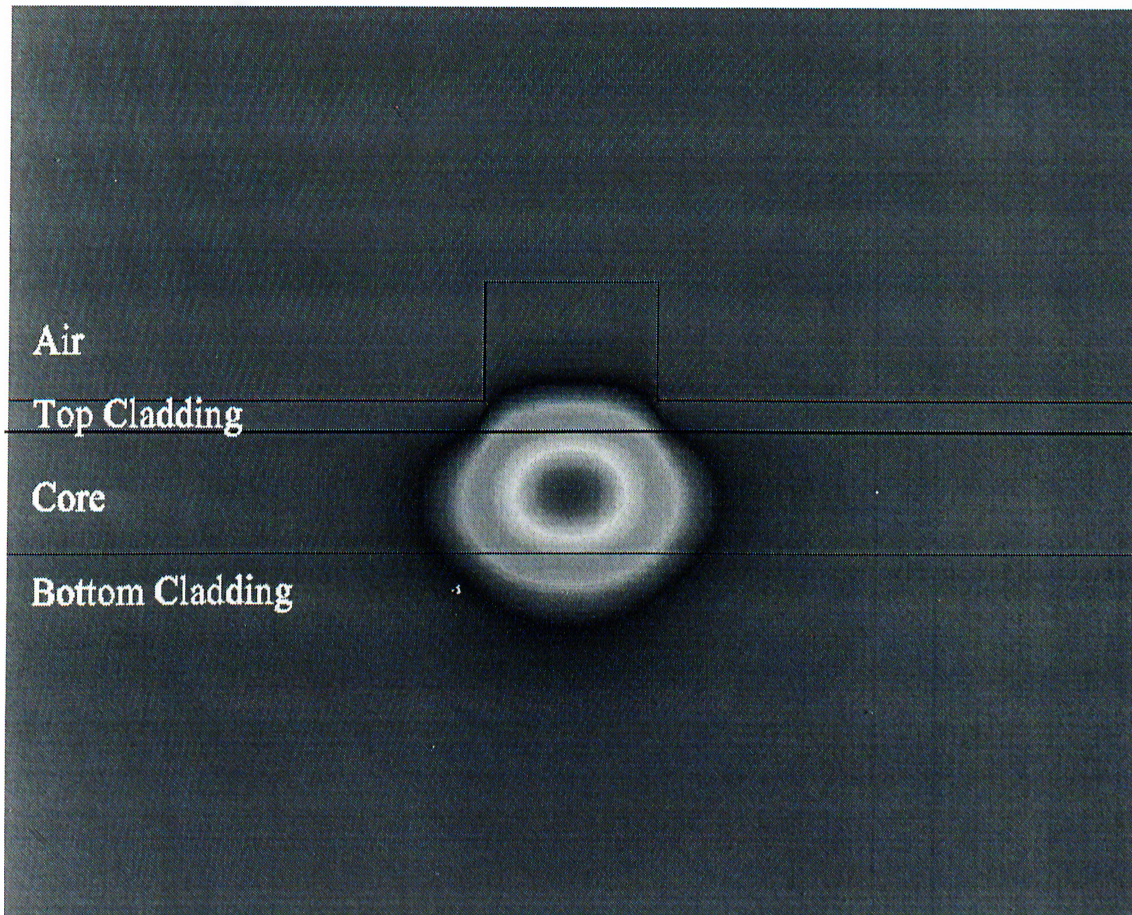

Figure 2.8: Confinement of the Optical Field Under the Rib

The final heterostructure used for the design and fabrication of single mode waveguide is composed of alternating layers of AlGaAs. It is well known that addition of Al lowers the index of refraction and hence control of composition allows for precise control of the refractive index[13] (Fig. 2.10). Since commercially available substrates are GaAs, which has the highest refractive index in the AlGaAs system, it becomes necessary to introduce a bottom cladding with a refractive index lower than the confining core layer but thick enough to quench the optical field before it reaches the substrate (Fig. 2.11).

As seen in Fig. 2.10, the index value decreases as the composition ratio of Al increases. So, the core region Al composition y has to be smaller than x in

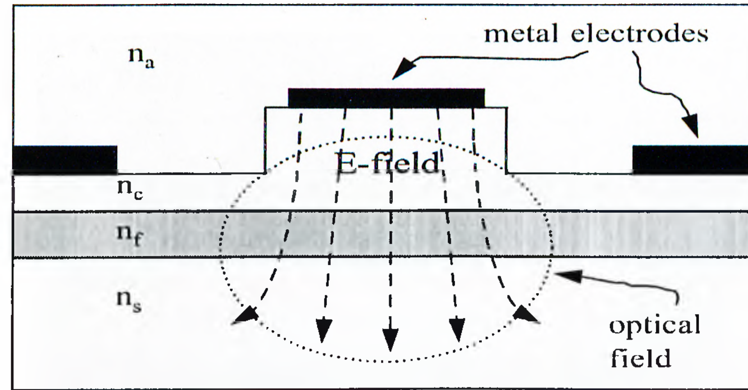

Figure 2.9: Metal Coated Four Layer Rib Waveguide

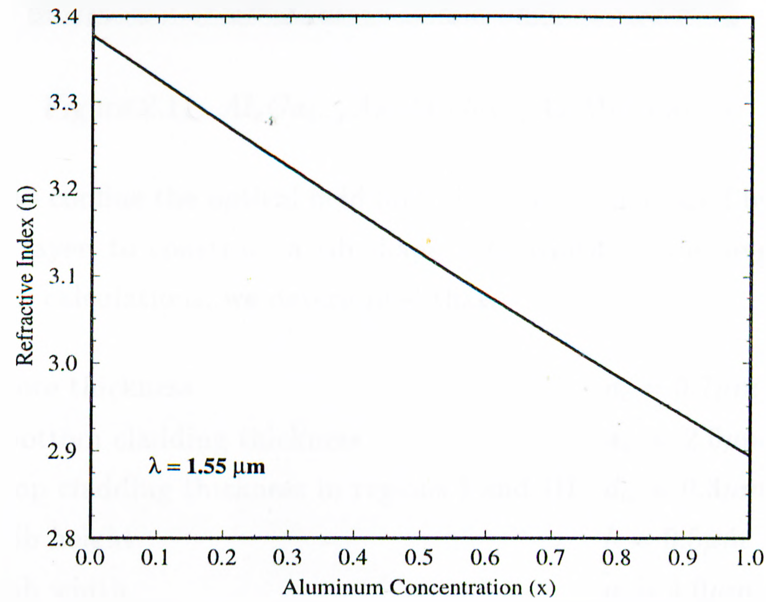

Figure 2.10: Dependence of Refractive Index on Aluminum Composition (x) of $Al_xGa_{1-x}As$ at $\lambda = 1.55\ \mu m$

Fig. 2.11 to have an adequately higher index and so as to confine the optical mode vertically. The necessary values of x and n are chosen to be :

$$x = 0.61 \quad n_{Al_{0.61}Ga_{0.39}As} = 3.225$$

$$y = 0.30 \quad n_{Al_{0.30}Ga_{0.70}As} = 3.072$$

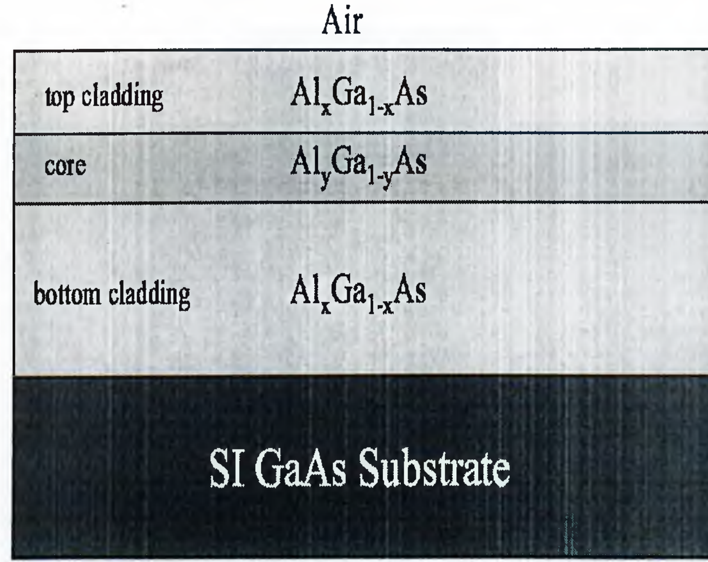

Figure 2.11: $Al_xGa_{1-x}As/Al_yGa_{1-y}As$ Multilayers

Next step is to confine the optical field laterally. This is managed by etching the top cladding layer, to construct a rib shape with width w and height h. Using effective index calculations, we determined that,

core thickness	$d_c = 0.7\mu m$
bottom cladding thickness	$d_{bc} = 2.0\mu m$
top cladding thickness in regions I and III	$d_{tc} = 0.3\mu m$
rib height	$h = 0.5\mu m$
rib width	$w = 4.0\mu m$

would satisfy single mode operation at $\lambda = 1.55\ \mu m$ (Fig. 2.12).

Since our object was to investigate the loss characteristics of such a waveguide with metal overlayer, the single mode operation was essential. Waveguide characteristics can also be calculated using numerical algorithms to solve the scalar wave equation with general $n = n(x, y, z)$. Such methods are called *Beam Propagation Methods*[14-18] (BPM). In this work, a commercial BPM simulator was occasionally used to confirm various waveguide properties such as the mode spectrum and shape. BPM assumes small index differences along propagation

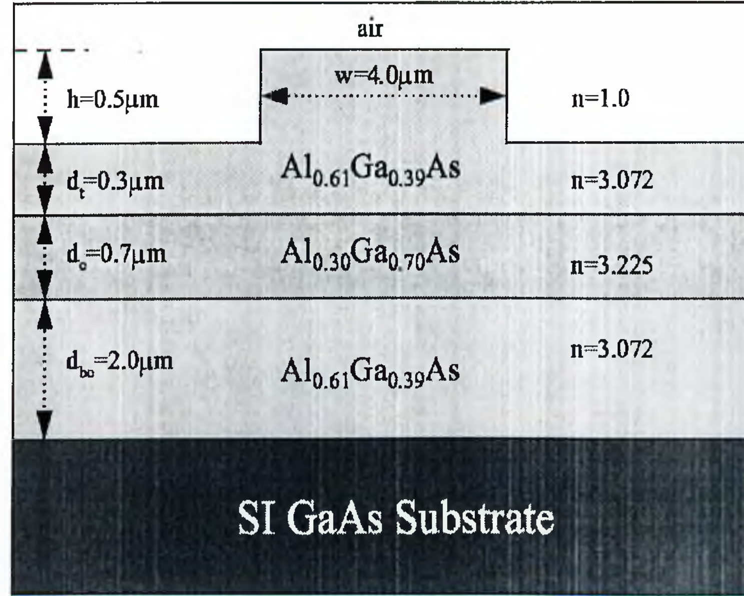

Figure 2.12: Single Mode AlGaAs Rib Waveguide

direction and no back reflected waves in waveguide. Under these conditions Eq. 2.3 reduces to :

$$2ik_0 n_r \frac{\partial \psi}{\partial z} = \frac{\partial^2 \psi}{\partial x^2} + \frac{\partial^2 \psi}{\partial y^2} + k_0^2[n^2(x, y, z) - n_r^2]\psi \tag{2.21}$$

where n_r stands for a refractive index describing the average phase velocity of the wave. Numerical calculation with this method works reasonably for z-invariant waveguides, as in our design, if the x and y axes are divided into sufficiently small grid size with respect to z axis grid size.

In Fig. 2.13, parameter n_{bar} stands for the computed index for the zeroth order mode and n_{eff} stands for the effective index, computed by BPM. In this graph, y-axis shows the ratio of optical power distribution over index to the total power. The sharp and intense peak at $n_{eff} - n_{bar} = 0$ is the signature of a single mode waveguide. The other small peaks are due to virtual localization of the optical field at the index step boundaries, as a result of finite grid size, and are insignificant. As a result, BPM computations also yield single mode operation.

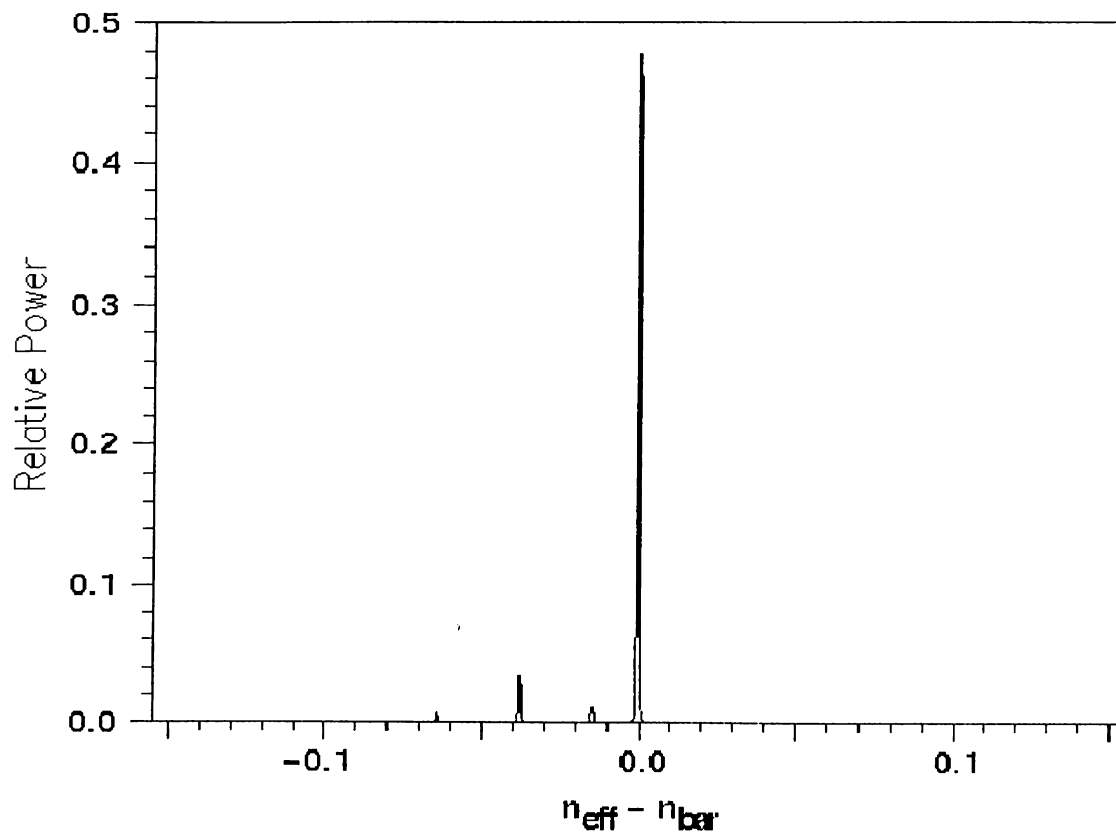

Figure 2.13: Mode Calculation with BPM

2.3 Optical Loss

The waveguide parameters such as widths and thicknesses can be calculated to reflect the demands of a particular design. But the non-ideal material properties and processing imperfections also affect the performance of the waveguides. An outstanding effect of these is the optical intensity attenuation of the mode as it propagates along the waveguide due to waveguide optical loss.[11,12] Letting I_0 to be the initial intensity, optical intensity has to be a function of z, z being the propagation direction, such that $I(z) = I_0 e^{-\alpha z}$ where α is the loss factor, or extinction coefficient, with units $[cm^{-1}]$. Optical loss itself is often measured in units of dB/cm, where we define dB as the ratio of the transmitted to incident intensity (or power),

$$
\begin{aligned}
dB &= 10\log(\tfrac{I_{trans}}{I_{inc}}) \quad \text{in terms of intensity} \\
dB &= 20\log(\tfrac{I_{trans}}{I_{inc}}) \quad \text{in terms of power}
\end{aligned} \tag{2.22}
$$

Using the definition of dB, dB loss and loss factor can be related as,

$$
\alpha_{dB} = \frac{10}{\ln 10}\alpha \tag{2.23}
$$

where α_{dB} has units of dB/cm and α has units of cm^{-1}. The total loss factor is simply the superposition of optical losses from a number of sources.

2.3.1 Loss Mechanisms

Band-Edge Absorption Loss

The photons having energy close to the band-gap of the semiconductor, i.e, the energy difference between the valence and conduction bands, may be absorbed promoting an electron from the valence band to the conduction band. Absorption increases drastically, as the energy of the propagating photon approaches the band-gap energy of the material. The fundamental lower wavelength limit for the light propagation in semiconductor materials is therefore a natural consequence of band-edge absorption. Moreover due to existence of band-tails the operating wavelength of the low-loss waveguides should be well isolated from the band-edges. The operating wavelength of 1.55 μm satisfies this condition well.

Free-Carrier Absorption Loss

The absorption of carriers within the same band can also be significant as a loss component. The electrons (holes) can gain a higher energy level in the same band by absorbing a photon. It is predictable that, this kind of absorption increases as the electron (hole) concentration and photon wavelength increases. Free-carrier absorption is formulated as;

$$
\alpha_{fc} = \frac{q^3\lambda_0^2 n_e}{4\pi^2 c^3 n_0 \epsilon_0 \mu m^{*2}}
$$

where n_e is the electron density, q is the electron charge, ϵ_0 is the permittivity of the free space, μ is the mobility, m^* is the effective mass of electron, c is the speed of light, n_0 is the refractive index of the material without the free carriers and λ_0 is the wavelength. This kind of loss mechanism becomes significant at high doping concentrations. For demonstration it will be adequate to quote that a doping of 10^{18} cm^{-3} yields a free-carrier absorption loss on the order of 1 dB/cm in GaAs. The use of undoped layers makes this mechanism negligible in our waveguide.

Scattering Loss

Any kind of roughness or disorder in the waveguide, possibly created while growth and/or processing, lead to optical loss due to scattering. When the guided mode is distorted by an irregular change in refractive index, it may result in some portion of the guided mode to scatter out of the waveguide. This may even cause the optical field to couple to the higher order modes or to leak into the slab. The MBE and MOCVD layer growth techniques in semiconductors yield vertical boundaries flat within a monolayer of material, so that scattering in the crystal plane is usually negligible. Lateral boundaries that are made up of etched rib and ridge geometries, may be very problematic due to sidewall roughnesses serving as scattering centers. Optimization of wet or dry etching is required to minimize this loss component.

Radiation Loss

Radiation implies the leakage of energy from the guided mode either into the substrate or into the air above the waveguide. For well-designed waveguides, radiation loss is not an issue; nevertheless in some cases it becomes inevitable. The waveguides having sharp bends and curved sections also play role in high radiative loss. The curvature of any deviation from z-direction has to be carefully designed in order to reduce the radiation loss. The bottom cladding thickness of 2 μm is large enough to minimize radiation loss to SI GaAs substrate.

2.3.2 Loss Characterization Techniques

We had previously stated the importance of loss reduction in our design. So we need the methods to measure the waveguide optical loss to demonstrate that quantitatively. For this reason the methodology of loss measurement techniques are presented in the following sections. There are two main approaches to measure optical loss called the cut-back technique and the Fabry-Perot resonance technique.

Cut-back Technique

This is the simplest approach to measure the optical loss in a waveguide. If we measure the amount of transmitted light through a set of identical waveguides having different lengths with a constant input power, we can deduce the loss coefficient. To guarantee the identical waveguides we can start with an initially relatively long waveguide and measure its transmitted optical intensity. Then, we cut a small slice from the end of the waveguide wafer and measure the transmitted light intensity again. Repeating this many times we can obtain the transmitted light intensity versus waveguide length curve, hence the name cut-back.

For the output intensities I_1 and I_2 measured for waveguide lengths L_1 and L_2 the loss of the waveguide can be expressed as

$$\alpha = \left(\frac{1}{L_1 - L_2}\right) \ln\left(\frac{I_2}{I_1}\right) \tag{2.24}$$

where L_1 is taken to be the longer waveguide length. For a more precise result, output intensity has to be measured for a number of different waveguide lengths and $\ln(I_{out}/I_{in})$ has to be plotted as a function of L. The resulting linear plot then yields a slope of $-\alpha$.

Although the method is quite simple, its accuracy is questionable since the reproducibility of input coupling can hardly be guaranteed experimentally. Moreover in low-loss waveguides it may not be possible to distinguish the intensity change for a small change of waveguide length.

Fabry-Perot Resonance Technique

Waveguides having mirror like input and output facets can be regarded as waveguide cavities, thus resonators. The transmission through this resonator is then a function of the loss in between the mirrors. Therefore the input and output facets of the waveguide has to be good quality cleaved facets.

The ratio of transmitted optical intensity (I_t) to the incident optical intensity (I_i) can be written in terms of amplitudes,

$$\frac{I_t}{I_i} = \frac{A_t^* A_t}{A_i^* A_i} = \frac{1 - Re^{-\alpha L}}{1 - Re^{i\delta} e^{-\alpha L}} \cdot \frac{1 - Re^{-\alpha L}}{1 - Re^{-i\delta} e^{-\alpha L}} = \frac{(1 - Re^{-\alpha L})^2}{(1 - Re^{-\alpha L})^2 + 4Re^{-\alpha L} \sin^2\left(\frac{\delta}{2}\right)} \tag{2.25}$$

where R is the facet reflectance, α is the loss coefficient, L is the cavity length and δ is the phase difference between adjacent waves in the resonator. The maximum transmission $\frac{I_{max}}{I_0} = 1$ takes place when $\delta = 0$ and minimum transmission takes place when $\delta = \pi$ of the value,

$$\frac{I_{min}}{I_0} = \frac{(1 - Re^{-\alpha L})^2}{(1 - Re^{-\alpha L})^2 + 4Re^{-\alpha L}} \tag{2.26}$$

We can then define a dimensionless contrast ratio κ as

$$\kappa = \frac{I_{max}}{I_{min}} = \frac{(1 + Re^{-\alpha L})^2}{(1 - Re^{-\alpha L})^2} \tag{2.27}$$

by which the waveguide loss can be derived as,

$$\alpha = -\frac{1}{L} \ln\left[\frac{1}{R} \frac{\sqrt{\kappa} - 1}{\sqrt{\kappa} + 1}\right] \tag{2.28}$$

We see that the optical loss may be evaluated from the contrast of Fabry-Perot resonances,[10,19] facet reflectivity, and the cavity length of a single waveguide device independent of input or output coupling. As the cavity length during the measurement is fixed, Fabry-Perot resonances are obtained by temperature tuning the wavelength of the excitation source, from which κ can directly be measured. Alternatively, the waveguide cavity resonator length can be slightly modified by

a small change in waveguide temperature. As the effective facet reflectivity may not necessarily known, inspection of Eq. 2.28 allows us to introduce a further step to determine α and R independently. This, we achieve by taking a series of κ measurements by successively shortening the physical length of the waveguide by cleaving it at one end. With the knowledge of resonance contrast and waveguide length data of a set of various lengths of identical waveguides it is possible to deduce the facet reflectivity and loss at the same time by plotting the value :

$$10 \cdot \log_{10}\left(\frac{1+\sqrt{\kappa}}{1-\sqrt{\kappa}}\right)$$

as a function of L. Extrapolating the value intersecting the loss axis at $L = 0$ will supply the necessary information for the facet reflectivity while the slope of the linear plot will give the loss coefficient.

This technique is superior for the characterization of low loss waveguides.

2.3.3 Simulations of Loss Due to Metal Overlayer

Finally, the metal electrodes to be used for active electrical control of the devices need to be considered. In this work, we study metal electrodes deposited directly on rib waveguides as in Fig. 2.9. The gold layer serving as an electrode, has a high absorption coefficient, $k = 10.21$ at $\lambda = 1.55$ μm, while its refractive index is as small as $n = 0.18$.[45] This lossy medium superposed on the structure can be regarded as an additional propagation loss.

Being equipped with the knowledge of optical constants of this medium makes us able to include this one more layer while solving the scalar wave equation (Eq. 2.3) and evaluating the mode field distribution. Once the vertical field distribution is evaluated, the overlapping portions of the field with the metal could be interpreted as loss due to a large absorption constant. A 1-D finite difference algorithm was used to estimate the relative magnitude of the loss. Figs. 2.14 and 2.15 show how the field gets attenuated by the metal layer for both TE and TM polarizations. The x-axis in the figures is the vertical waveguide cross-section in nm. The y-axis stands for normalized field intensities and index distributions.

We see that the optical field is mainly confined in the core layer with a peak value centered in the middle of this layer. However it has extensions through the top and bottom claddings. The bottom cladding is sufficiently thick (2 μm) to prevent the leakage to the GaAs substrate as opposed to the top cladding layer. The top cladding layer with a thickness of 0.8 μm gives rise to the extension of the light into the air when metal electrode is not present.

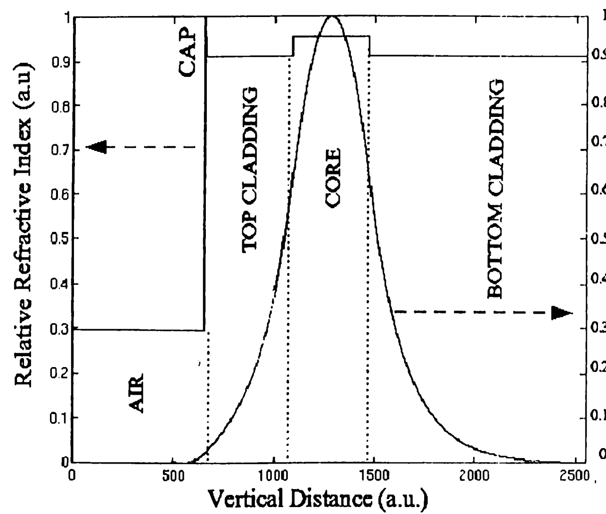

Figure 2.14: The Vertical Field Distribution in the Absence of a Metal Layer

In case of metal electrodes, the calculated loss values of 0.18 dB/cm and 8.5 dB/cm for TE and TM polarizations respectively, show that metal loss is an essential problem in waveguide operation especially for TM polarized light. This problem may partly be solved by increasing the top cladding thickness from 0.8 μm up to some large value such as 2.0 μm as the bottom cladding so that the optical field may be well isolated from metal overlayers. Therefore idea of increasing top cladding thickness remains as an option for a low TM loss optical waveguide. In Fig. 2.16 the dependence of loss on top cladding thickness is displayed.

A thick top cladding layer in a waveguide is generally not favored since the E-field intensity will be weaker at the core layer - where most of the optical power is carried - as the distance from the core to the electrode increases. Moreover the

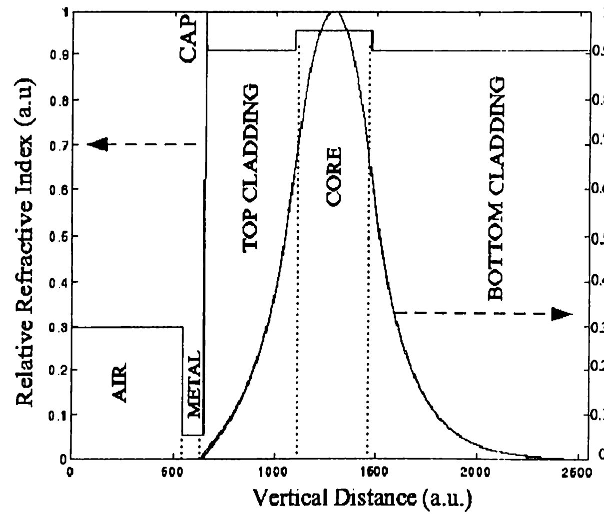

Figure 2.15: The Vertical Field Distribution in the Presence of a Metal Layer

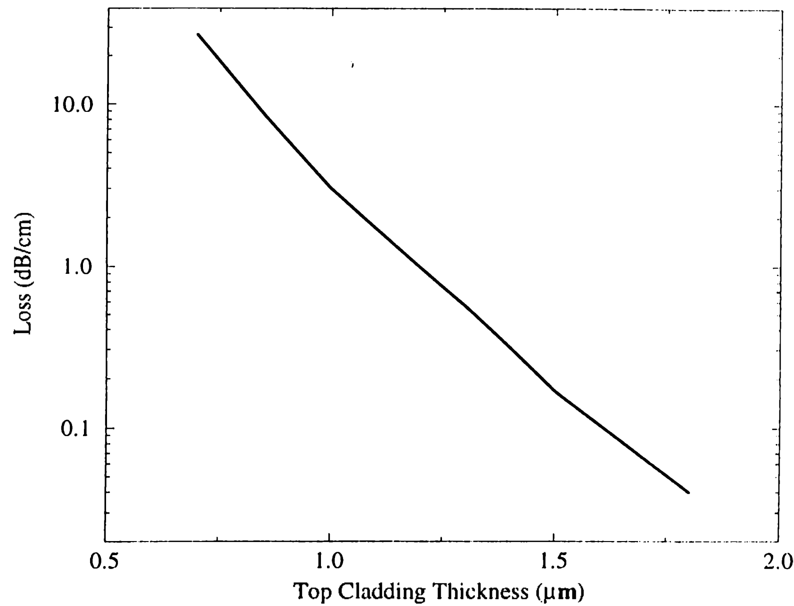

Figure 2.16: Calculated Loss as a Function of Top Cladding Thickness

Schottky type metal contacts stand up to a certain value of the applied voltage before the Schottky barrier breaks-down. So in this respect, waveguide designers are forced to find a way to prevent metal loss while keeping top cladding layer thickness small. Vertical confinement of optical field in the core layer can also be

achieved with thinner top cladding layer by converting some portion of the rib to a lower index material for a higher index contrast.

Dependence of refractive index of $Al_xGa_{1-x}As$ on x composition (Fig. 2.10), gives a clue about the choice of a low index material. Pure AlAs having an index of $n = 2.9$ at our operating wavelength is a step in the right direction.

2.4 Low Loss Waveguide Design

We have studied the effect of converting a 0.4 μm thickness of 0.8 μm top $Al_{0.61}Ga_{0.39}As$ layer to AlAs. 1-D finite difference simulations yield encouraging results (Fig. 2.17).

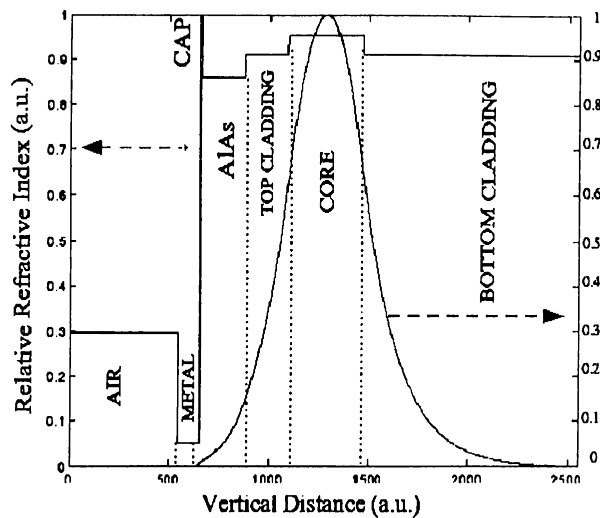

Figure 2.17: Loss Calculation-1
Loss calculation of waveguide with 0.4 μm $AlAs$ / 0.4 μm $Al_{0.61}Ga_{0.39}As$ top cladding

The calculated value of 2.2 dB/cm for TM loss is a large step in eliminating metal loss with respect to the previously calculated loss value of 8.5 dB/cm but this is still unacceptable for operation of most PIC's.

Recently, there has been much progress in utilization of oxidized $Al_xGa_{1-x}As$ layers in optoelectronic devices. Much of this has been in the area of vertical

cavity surface emitting lasers (VCSELs) where the electrical insulation and low index of the oxidized layers lead to low threshold lasers. This technology has also been used to demonstrate metal-oxide-semiconductor field effect transistor (MOSFET) operation where thin layers of oxidized $Al_xGa_{1-x}As$ layers have been used under the gate.[30] The fact that this application shows the possibility of applying electric field to underlying active layers through oxidized $Al_xGa_{1-x}As$ (AlOx) layers is technologically very important. While passive optical waveguide devices is slowly forthcoming, the real advantage of these layers in active devices lie in the possibility of applying electric fields through them. The low index combined with this possibility is very promising for a variety of devices including polarization sensitive devices.

It has been previously reported that the refractive index of AlAs drops drastically from 2.9 to about ~ 1.6 when oxidized.[21] The reason for this change in refractive index is the total reconstruction of the chemical composition. Thus AlOx layers provide an even lower index than AlAs layers and hence lead to stronger quenching of the field before it reaches the metal overlayers. We have included AlOx layers of various thickness into our 1-D finite difference calculations to see the effect on loss. We have found that a thickness of 0.4 μm was sufficient and reduced the metal loss down to below 1 dB/cm for TM polarization which is satisfactory (Fig. 2.18).

Although the lattice constants of $Al_xGa_{1-x}As$ and $Al_yGa_{1-y}As$ crystals for any x and y, are known to be very close, their thermal expansion coefficients were reported to be quite different, giving rise to interface stress on the order of 10^8 dyn/cm^2, when grown successively on GaAs substrates.[42] In addition, interface stress was known to be an increasing function of the temperature. Thus, our multilayer structure, having a 0.4 μm x=1.00 layer on top of a y=0.61 layer, was expected to experience high stress, while being oxidized at 400^0C. To minimize the possible stress related problems such as surface cracks, we have inserted a 100 Å graded x $Al_xGa_{1-x}As$ layer at the $Al_{0.61}Ga_{0.39}As$/AlAs interface. Furthermore, we have changed the top AlAs layer to $Al_{0.98}Ga_{0.02}As$ to improve lattice matching.

From this point on, the waveguide structures with $Al_{0.98}Ga_{0.02}As$ top layer, its

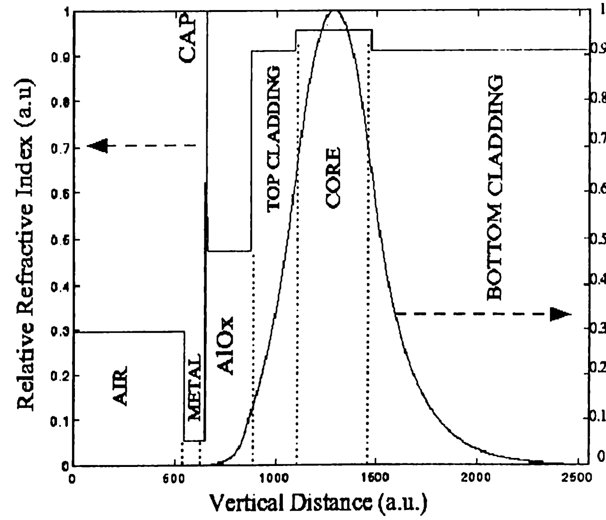

Figure 2.18: Loss Calculation-2

Loss calculation of waveguide with 0.4 μm $AlOx$ / 0.4 μm $Al_{0.61}Ga_{0.39}As$ top cladding

oxidized version and waveguide structure with a thick $Al_{0.61}Ga_{0.39}As$ top cladding layer will be called as WG1, WG2 and WG3 respectively, for convenience.

Changing the index of the material in the rib of the waveguide exposes no risk on single mode operation since the effective index of the waveguide shifted to lower values and normalized parameter V in condition 2.20 tended to take a smaller value. But a slight tuning in the rib height has been necessary to enhance the lateral confinement of light.

At the end we have reached our final waveguide designs as in the figures 2.19, 2.20 and 2.21.

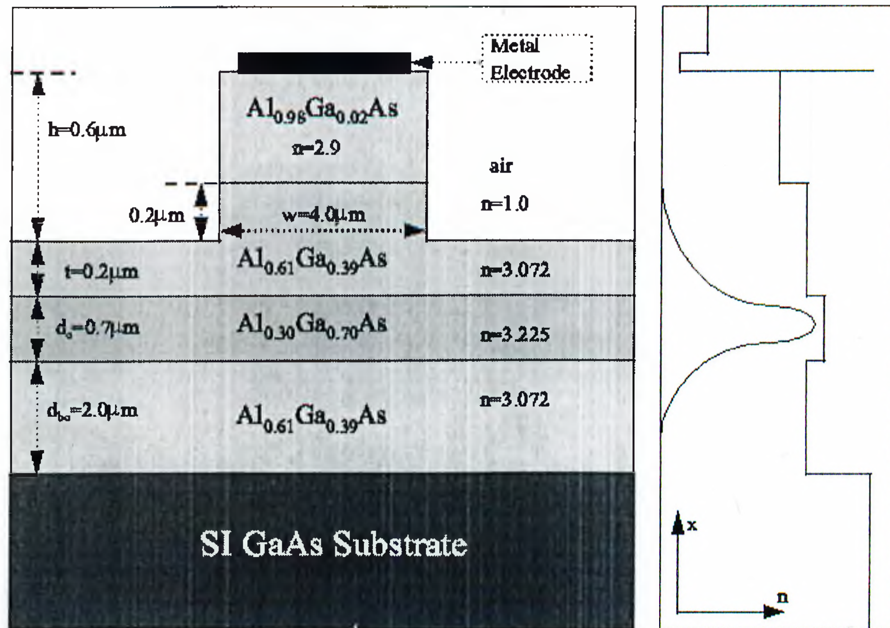

Figure 2.19: Final Design of WG1 Waveguide

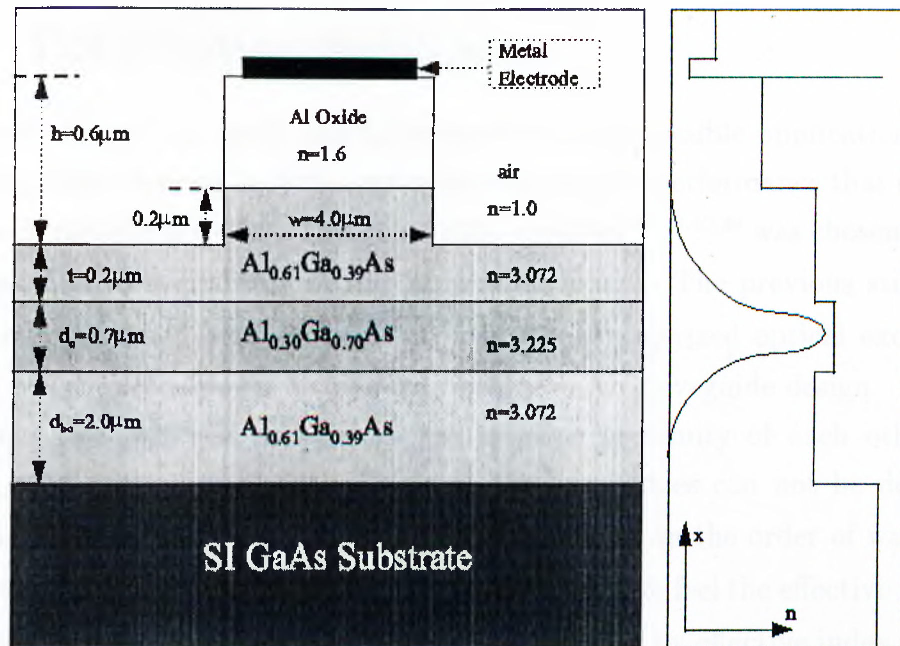

Figure 2.20: Final Design of WG2 Waveguide

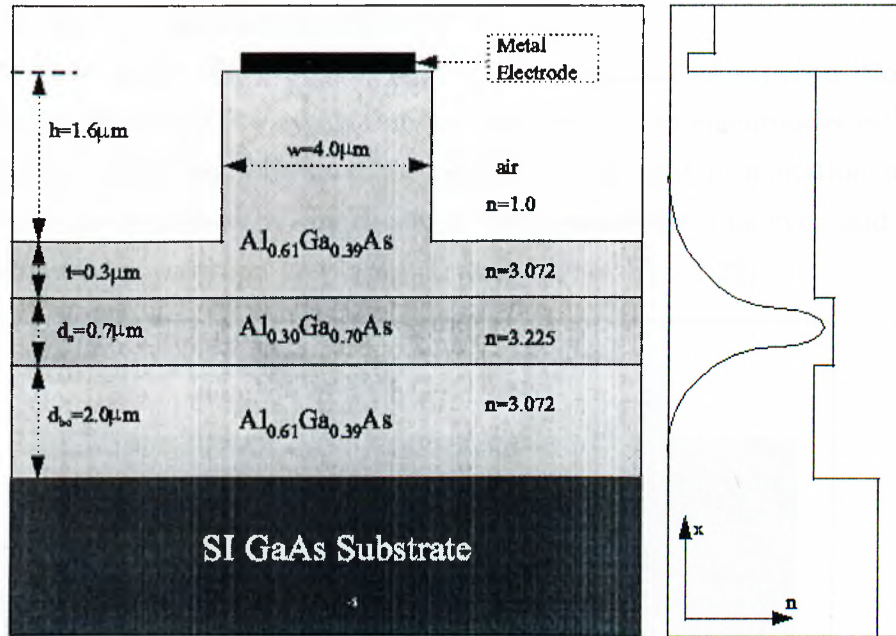

Figure 2.21: Final Design of WG3 Waveguide

2.5 Polarization Splitter

The next step of our study was to demonstrate the possible application of loss reducing AlOx layer on an active optoelectronic device performance that required the use of metal electrodes. The polarization splitter[36-38,40,39] was chosen for this purpose, due to availability of the fabrication masks. The previous studies on this device reported high propagation loss of TM polarized optical excitations due to metal electrodes on a standard multilayer rib waveguide design.

When two identical waveguides are in close proximity of each other, the propagation properties of optical field in the waveguides can not be described separately. When the separation of two waveguides is on the order of waveguide width, the light propagating in any one of them starts to feel the effective index of the other. The structure should be treated as a whole by effective index method and/or BPM. The medium, where the optical field propagates will be composed of two index steps, rather than one. This double waveguide structure will be called a coupler based *polarization splitter*. The operation principle of the polarization

splitter can be summarized as follows :

The mode shape of the optical field will be composed of superposition of two eigenmodes. But the complex system should have its own eigenmodes rather than the eigenmodes of the individual waveguides.[9] The light propagation in such a system can be described by the choice of two eigenmodes, one even and one odd with different propagation constants β_e and β_o (See Fig. 2.22).

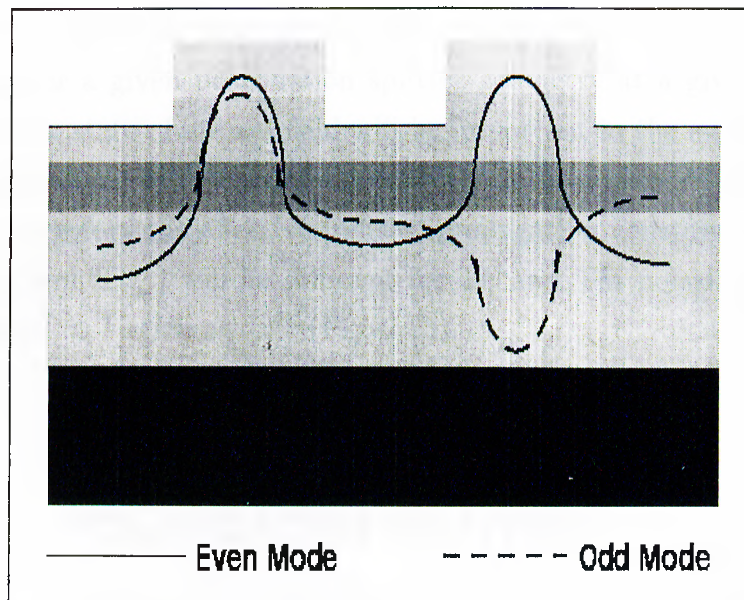

Figure 2.22: Electic Field Distribution of the Odd and Even Modes of a Polarization Splitter

The wave equations used to describe this system are called the coupled wave equations. Since the propagation constants of the two modes are different, the field energy will not always be carried in the waveguide, into which it was initially incident. Let us assume that light is initially incident on only one of the waveguides in Fig. 2.22. If we describe the optical field in the coupler's eigenmode space, the two modes interfere constructively at the input waveguide and destructively in the neighboring waveguide. As the light propagates through the coupler system, the location of constructive interference in y direction will shift since a phase delay between even and odd modes will develop in propagation (z) direction. The optical energy will be totally shifted to the neighboring guide

when the phase difference becomes π. Hence we can say that the optical field will be totally moved (coupled) to the other waveguide. The total physical length traversed by the optical field until it is coupled to the other guide will be called the *coupling length* (L_c). Then, the coupling length can be written as :

$$L_c = \frac{\pi}{\beta_e - \beta_o} \tag{2.29}$$

With the help of effective index method, the parameters β_e and β_o, thus L_c, can be calculated for a given polarization splitter geometry at a given wavelength. The polarization state of optical field will be important in the analysis since two different polarizations will yield different effective indices because of the boundary conditions. Therefore the effective indices, propagation constants and coupling lengths ($L_{c_{TE}}$ and $L_{c_{TM}}$) will be different for TE and TM polarized fields. This can be regarded as *birefringence*[41] (Fig. 2.23).

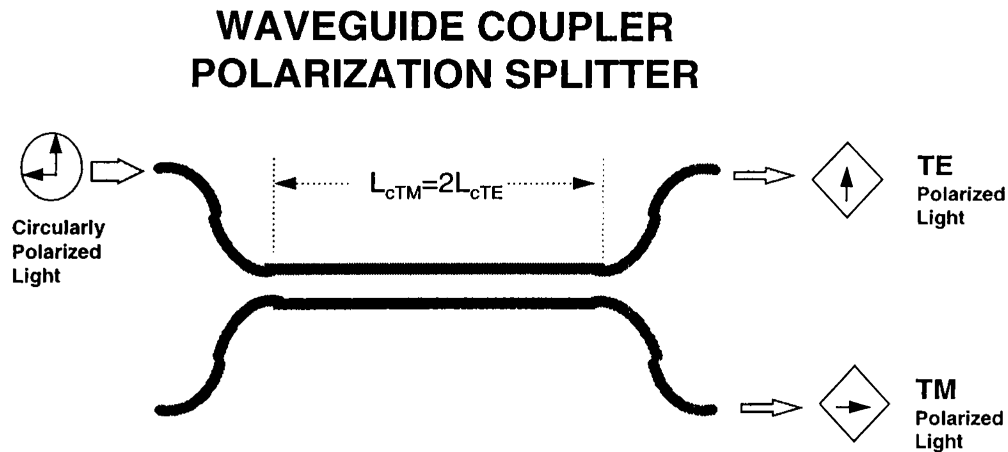

Figure 2.23: Waveguide Coupler Polarization Splitter

As we intend to investigate the effects of AlOx layers on polarization splitting, we have simulated the dependence of various geometrical parameters on coupling length ratios as in Figs. 2.24, 2.25, 2.26, and 2.27.

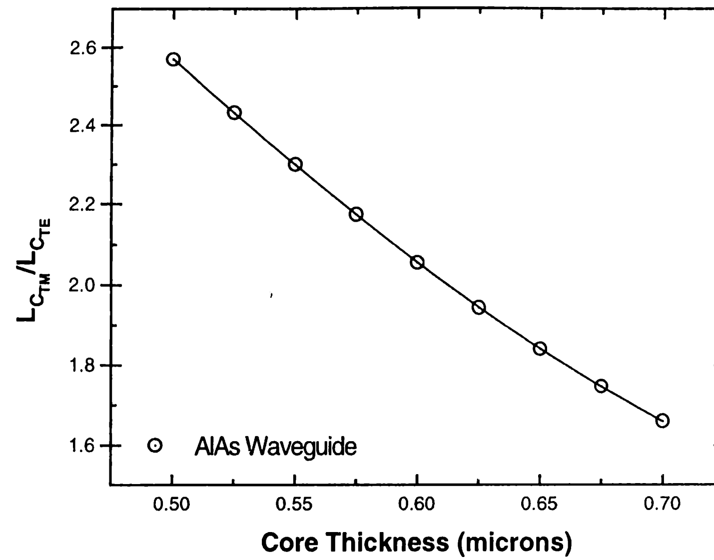

Figure 2.24: Coupling Ratio $L_{C_{TM}}/L_{C_{TE}}$ versus Core Layer Thickness

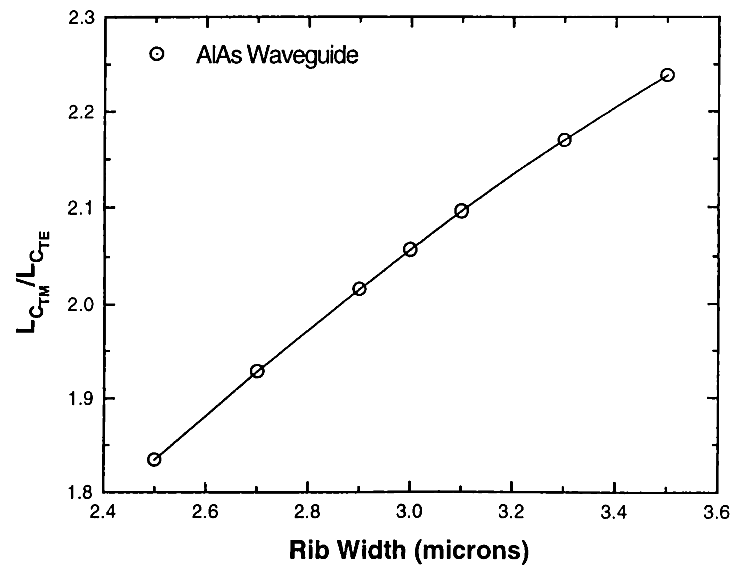

Figure 2.25: Coupling Ratio versus Rib Width

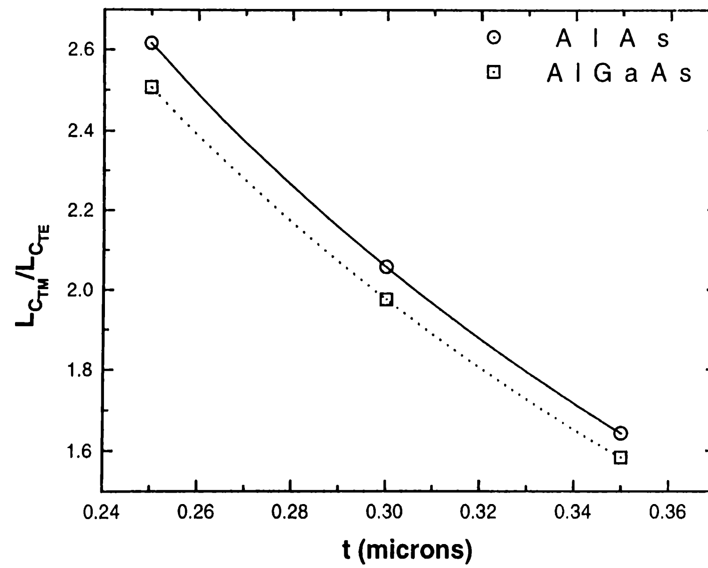

Figure 2.26: Coupling Ratio versus Top Cladding Thickness d_t as in Fig. 2.12

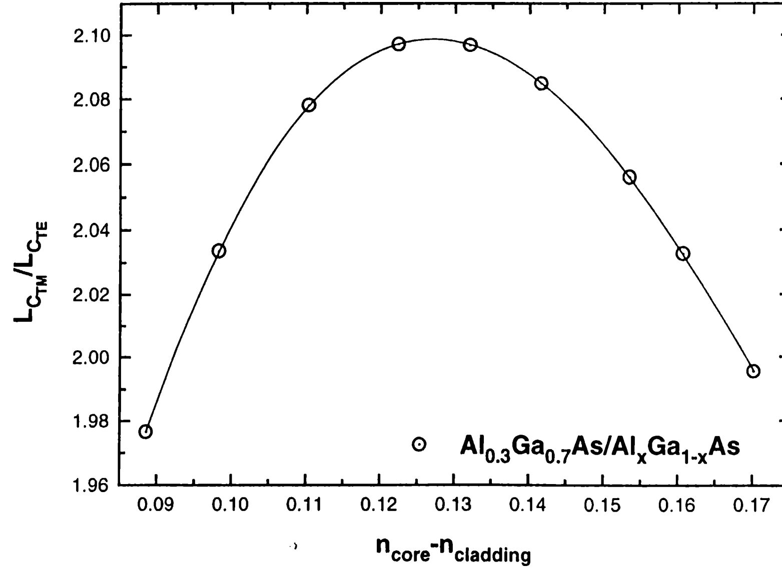

Figure 2.27: Coupling Ratio versus Δn
Δn is the index difference between core and cladding layers.

These simulations were done by effective index method. We have also done simulations by the commercial BPM program.

The figure 2.28 demonstrates multiple coupling of the TE mode between the two waveguides. Light couples back and forth in the straight section, since the coupling length is smaller than the straight sections of the polarization splitter. The figures 2.29 and 2.30 are for demonstration of polarization splitting. TE polarized light couples twice as TM polarized light couples once, propagating the same length. Hence, when a circularly polarized light is inserted at one of the input ports of the coupler, the TE and TM polarized optical fields exit at different output ports of the device.

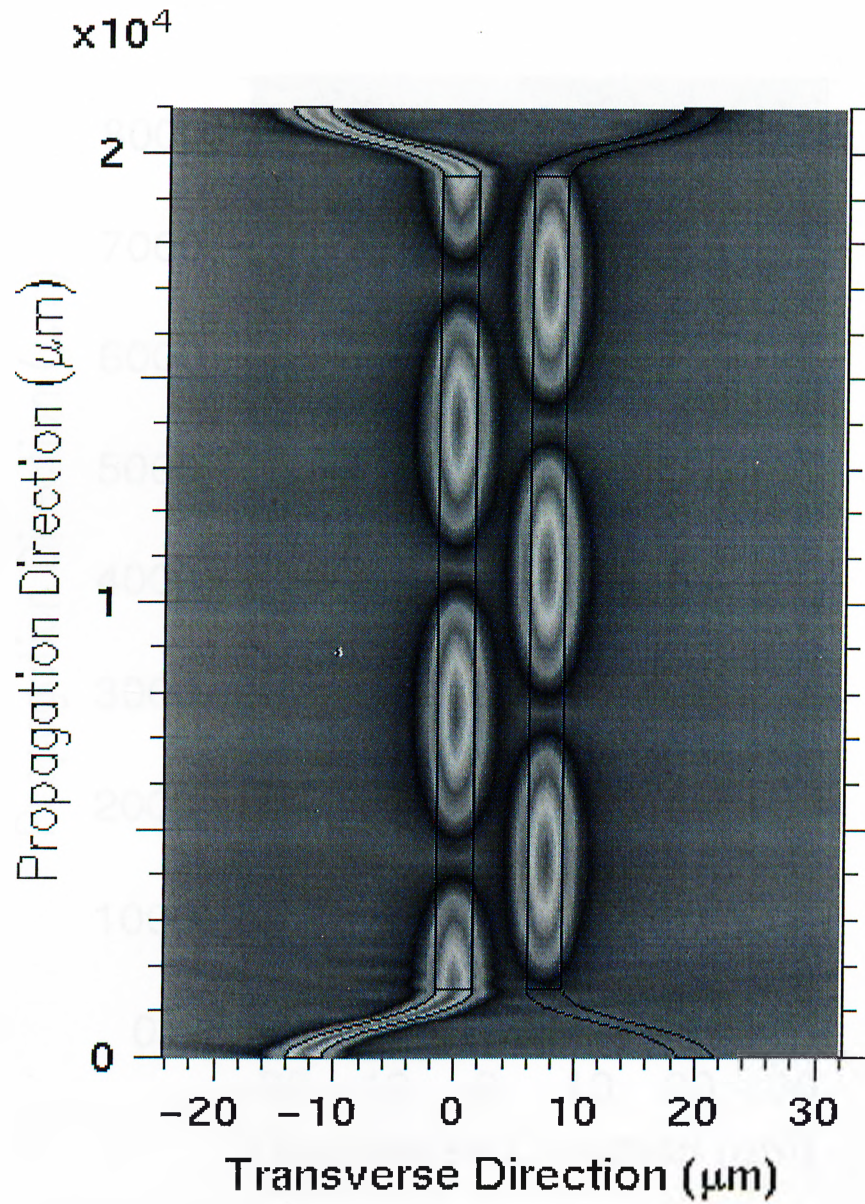

Figure 2.28: Multiple Coupling of TE Mode between the two Waveguides Light couples back and forth if the straight section length is larger than the coupling length.

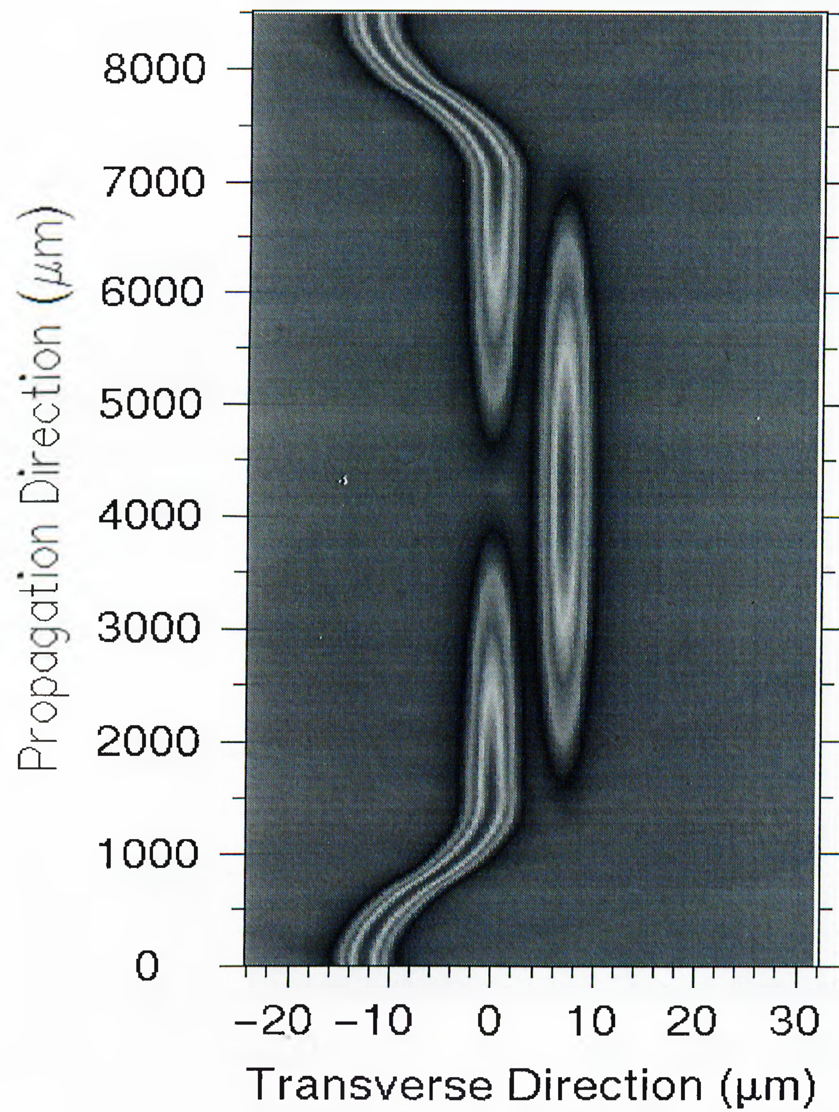

Figure 2.29: Coupling of TE Polarized Light
The straight section length of the coupler is approximately twice the TE coupling length.

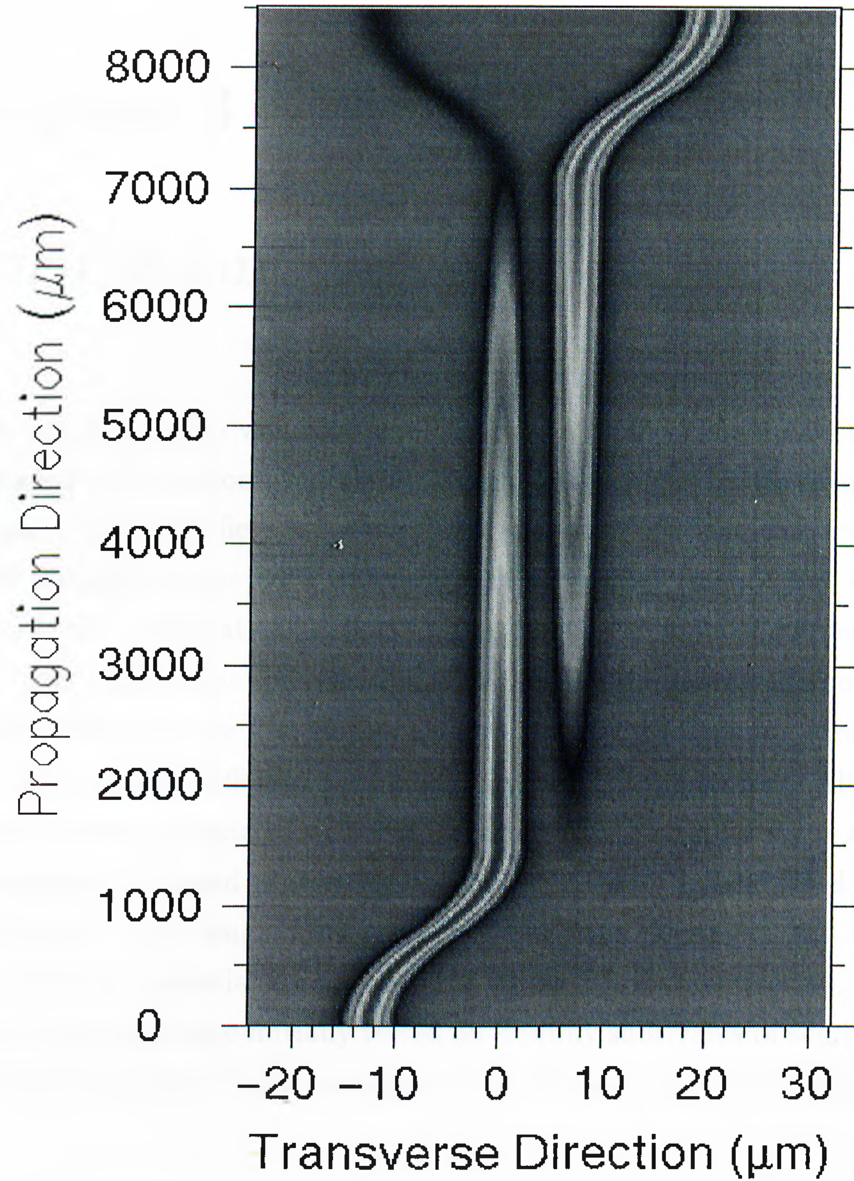

Figure 2.30: Coupling of TM Polarized Light
The straight section length of the coupler is approximately equal to the TM coupling length.

Chapter 3

Fabrication

The fabrication process was conducted in class 100 and class 10000 clean-room environment. Fabrication of straight waveguides with electrodes involved a two layer mask - one light-field for waveguides and one dark-field for electrodes. A series of straight stripes with different widths varying from 2 μm to 100 μm were available. Fabrication of polarization splitter devices, however, involved a three layer mask - one light-field mask again for the waveguide couplers and two dark-field masks for the electrodes and the electrode pads. More than 70 coupler devices with different gaps and lengths were fabricated. Although the fabrication process consisted of three major photolithography steps at most, it required utmost care and experience since the devices to be fabricated were 3 μm in width but 1-2 cm long. This geometry made the alignment and cleanliness issues to be very essential throughout the whole fabrication process. Therefore each and every step were initially tested on dummy substrates of semi-insulating (SI) GaAs consuming a large amount of time allocated for the fabrication.

3.1 Epitaxial Growth

The $Al_xGa_{1-x}As$ layers were Molecular Beam Epitaxy (MBE) grown on 2-inch SI undoped GaAs substrates. The growth uniformity was indicated to be about 3 percent over the whole substrate wafer up to 0.5 cm from the edges. After the

growth, the wafer was cleaved into 14 mm x12 mm and 12 mm x10 mm pieces. The 14 mm x12 mm pieces were used for straight waveguide fabrication whereas the 12 mm x10 mm pieces were used for waveguide coupler device fabrication.

3.2 Sample Cleaning

The cleaved pieces were first of all three-solvent cleaned. During this process pre-cleaned, relatively soft, kevlar tip tweezers were used for sample handling. This way sample edges and epilayer surface were prevented from unintentional scratches. 3-solvent cleaning included acetone (ACE), methanol (METH) and isopropanol (ISO) chemicals to remove the unwanted residuals from the surface of the samples such as dust, organic molecules, i.e. any kind of dirt. First, the samples were ACE blown to remove the macro particles and laid in room temperature pure ACE for 5 minutes. Then, they were METH blown and laid in room temperature METH for 5 minutes. METH is believed to dissolve ACE residue and oily adsorbents from the surface of the samples. The third stage was ISO dip. Samples were first ISO blown and then laid in boiling ($\sim 70^0C$) ISO for 5 minutes. ISO is believed to dissolve METH and the residues. The ISO was removed in de-ionized (DI) water by washing the samples under DI-water flow for 1 minute. Finally, the samples were pure nitrogen blown to remove the water droplets from the surface and kept in clean sample boxes to prevent from further contamination.

3.3 Photolithography

The mask patterns were transferred onto the epi-grown surfaces of the samples by means of photolithography, followed by subsequent etch and metalization processes. Different photoresists (PR) were used for different aims throughout the lithography. The cleaned samples were first baked on hotplate at 105^0C for 3 minutes to dehydrate the samples from the residual water vapor absorbed on the surface. Then the samples were left to cool down for about 5 minutes. The

samples that were ready for photolithography were then positioned on spinner chucks. For the etch patterns AZ4210 PR was filtrated with 2 μm syringe filter and spun on the samples at 5500 rpm. Before the exposure the samples were prebaked on the 95^0C hot-plate for 55 seconds. This PR was the most suitable one for reactive ion etch (RIE) process because it maintained a thickness of $\sim 1.6 - 1.7$ μm and it was possible to obtain 1 μm resolution. Our experience has shown that it was important to have an appreciable thick PR pattern on the samples to endure the long RIE processes. Moreover, it was also important to mask the samples with a high resolution PR while patterning the waveguides since our waveguide mask contained structures as small as 4 μm. After the alignment, samples were exposed with 7.5 mW/cm^2 @ 365 nm Hg lamp for 9 to 12 seconds. Every photolithography step was performed in the vacuum contact mode of the aligner to ensure minimization of the diffraction related resolution problems. In the next step, the exposed samples were developed in 1 : 4 AZ400K : H_2O mixture. The developing time varied in between 45 sec and 55 sec depending on the exposure time. Samples were then rinsed in flowing DI water for a minute and nitrogen blown. Before any etching or metalization processes, there was one more step to emphasize the durability of the PR pattern on the semiconductor surface: post baking. Many processes like metal evaporation and wet etching require a moderate post baking temperature as much as 120^0C and baking time as long as 1 minute. RIE process required considerably high baking temperatures in the range of 180^0C to 200^0C for 3 to 5 minutes. This is due to fact that whole etching process is not just by means of chemical etching but also includes a material independent physical etching counterpart. These issues will be discussed in the RIE etching section.

3.4 Wet Etching

The most widely applied technique in modification of the crystal surface is the wet etching technique. Wet etching can be defined as the etching of crystal surface by chemical reaction between the crystal material and an aqueous acidic or basic

solution. Many kinds of acids and bases are known to react with $Al_xGa_{1-x}As$ material. The etch rates can take values from several tens of Angstroms per minute up to several tens of microns. The etch rate depends on the type of etchant solution, temperature of the solution, Al composition of $Al_xGa_{1-x}As$, and crystallografic orientation. These dependencies have been studied carefully and selective etch conditions for different x compositions and different solution concentrations have been derived by several researchers.

Since wet etch is a chemical etch, the reaction between the active ions and the crystal atoms follows crystallografic planes. When the reaction starts from the surface of the crystal into the crystal, the etch profile is not necessarily straight in vertical direction. Deviations occur from the mask definition. These deviations may be tolerable for shallow etches but for deep-etches they accumulate to intolerable errors. For samples with a thick top cladding layer, large amounts of material is needed to be removed. Such large vertical etch depths are inevitably accompanied by large lateral etch thicknesses which undercut the rib structure beyond acceptable widths.

For thinner top cladding layers wet etching is a strong possibility and is widely used for materials such as $Al_xGa_{1-x}As$ where $x \leq 0.30$ using citric acid solutions.[23] To our knowledge no solutions for controlled removal resulting in smooth surfaces exist for $x \geq 0.40$. In the case of pure AlAs (x=1) and $Al_{0.98}Ga_{0.02}As$ there happened to be no possibility to etch this geometry by wet etch method. Following micrographs reflect this fact better than words. The figures belong to wet etched surfaces of AlAs with citric, hydrochloric and phosphoric acid solutions in the same order.

The etching method in our fabrication is therefore chosen to be the RIE.

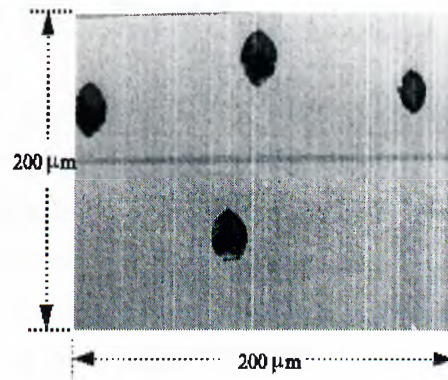

Figure 3.1: Wet Etched Surface of AlAs Crystal in Citric Acid Solution

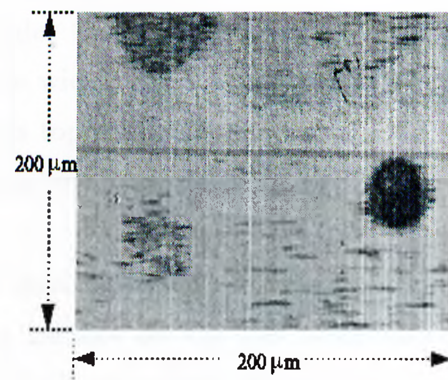

Figure 3.2: Wet Etched Surface of AlAs Crystal in Hydrochloric Acid Solution

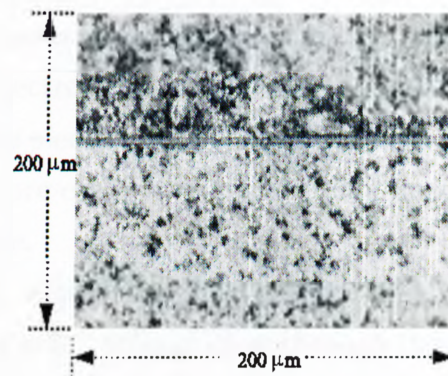

Figure 3.3: Wet Etched Surface of AlAs Crystal in Phosphoric Acid Solution

3.5 Reactive Ion Etching (RIE)

The reactive etching[24] process is a dry plasma etching process in which the semiconductor surface is etched by physically assisted chemical radicals and ions, accelerating from plasma onto the sample surface under a self generating DC bias. The plasma is obtained in a high vacuum chamber by radio frequency (RF) power incident on the etching gases. Before the etchant gases are let into the chamber, the chamber is evacuated by the help of a turbomolecular pump in order to decrease the base pressure below 10^{-6} Torr. The sample to be etched is positioned on a silicon tray on the bottom electrode. The bottom electrode can be cooled by He flow under the Si wafer tray. In GaAs and $Al_xGa_{1-x}As$ etching, $SiCl_4$ and BCl_3 gases are widely used as etchants.[26,27] The gases are let into the chamber from the porous top electrode shower head. In plasma etching both top or bottom electrodes can be powered but in RIE generally the bottom electrode is powered.

RF ionizes the gas molecules and accelerates the resulting free electrons. These electrons making impact on the gas molecules ionize the gas molecules further. This is called electron impact ionization. Electron impact in the gas phase results in production of radicals. Ions and electrons also recombine in gas phase to form excited neutral species. Excited molecules recombine to form ground state neutrals. Thus recombination results in reduction in energy level and resultant photo-emission. This is called the plasma glow. Recombination is enhanced by high pressure and large molecules. The ions in plasma have low energy, where the electrons have high energy. Therefore electrons sustain the plasma and of course the electrons are faster than ions. Thus electrons recombine at grounded surfaces more easily and quickly than ions. A plasma sheath forms at the powered electrode.

Plasma is left with a positive charge and the powered electrode has net negative charge yielding a DC voltage drop through the sheath. This DC voltage leads to ion directionality at the wafer. DC voltage is a self-developing potential difference and is equal to the voltage required to maintain plasma neutrality.

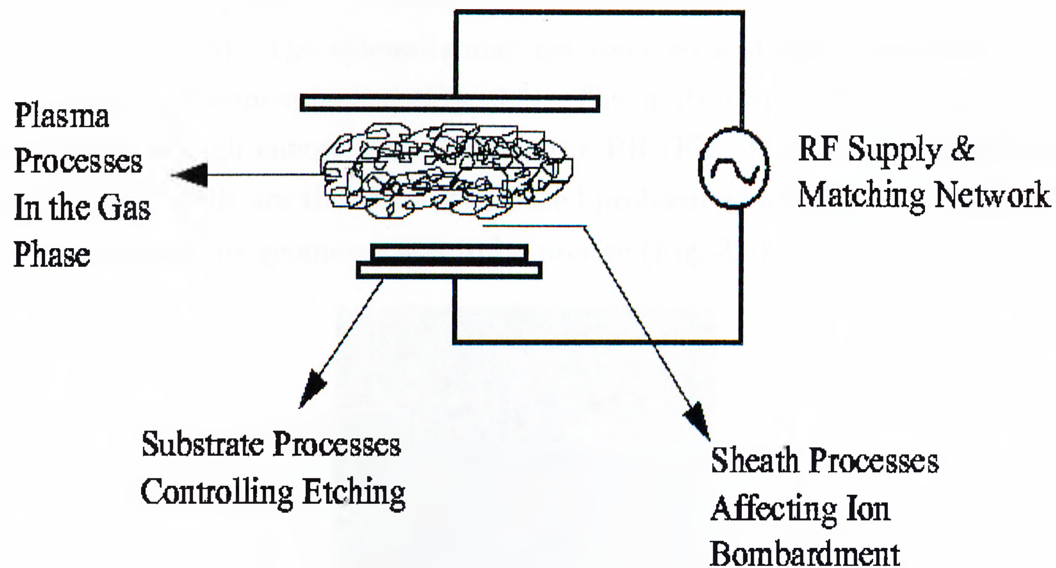

Figure 3.4: Components of RIE System

The plasma sheath has many functions. It accelerates ions to the wafer, makes ions highly directional close to normal incidence, and accelerates electrons back into the glow region. When the ions strike the wafer, they damage the surface, increasing rate of plasma etching by reactive species. Reactive neutrals interact with the surface molecules forming volatile reaction products. This is mainly a chemical etch promoted by physical modification of the surface. Since the ion path modifying the wafer surface is directional, the RIE etching is also directional, i.e. anisotropic. If the ions are dominant in the plasma, then only the exposed surfaces are etched; sidewalls are not etched. Thus photoresist mask pattern defines the etched structure. This can be achieved by lowering the chamber pressure. Lower the pressure, thicker the plasma sheath and thus more energetic the ions.

There are some inevitable side affects of the plasma processing on the etch geometry and rate. As described, RIE process consists physical and chemical components. Although the chemical reactions do not take place in between the reactive neutrals and the PR, the physical deformation of PR by accelerated

ions always takes place. This results in material loss from the photoresist during the etch (Fig. 3.5). The sidewalls may get rounded and the rectangular cross-section may get semi-spherical (Fig. 3.6). The sputtering of PR (Fig. 3.7) and penetration of high energy ions through the PR (Fig. 3.8) are other problems. Wriggled side-walls are the most often faced problem which had to be overcome since our waveguide geometry was to be precise (Fig. 3.9).

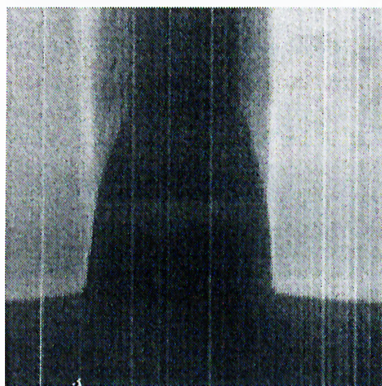

Figure 3.5: Photoresist Loss during the Etch

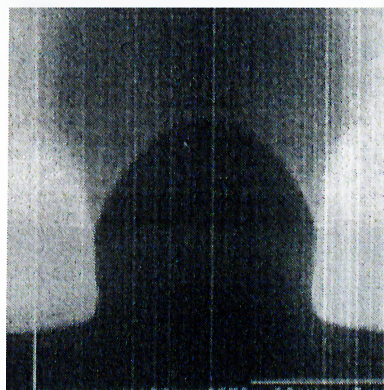

Figure 3.6: Rounded Photoresist Profile

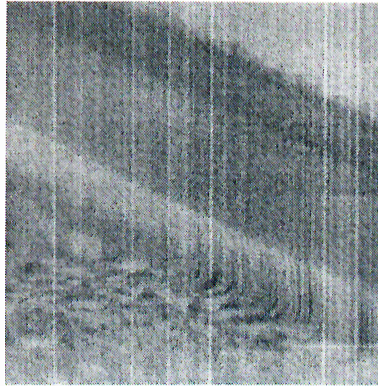

Figure 3.7: Sputtered Photoresist

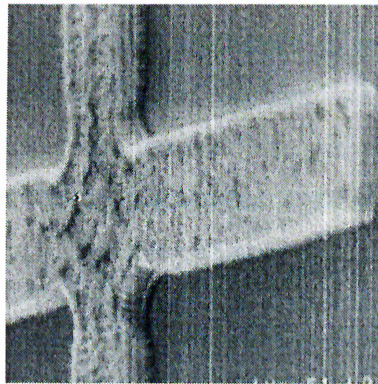

Figure 3.8: Penetration of Energetic Ions

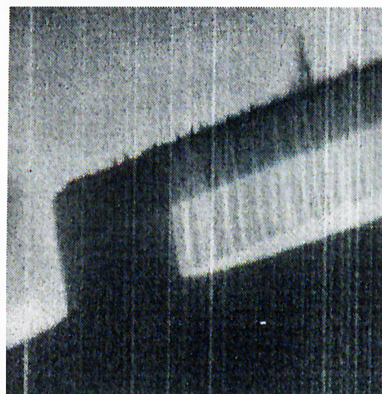

Figure 3.9: Wriggled Sidewalls

The PR mask, therefore needs to be hard baked to withstand this erosion until the desired etch depth is reached in forming the rib. Surface roughness of sidewalls is detrimental to waveguide operation. To minimize this, mask for etching process with good edge definition is required. It was suggested that Ti deposited on a PR layer provides good edge definition. For this aim AZ4210 PR was spun and baked on the sample. After that a thin ($\sim$ 2000 Å) layer of Titanium (Ti) was deposited on the PR by e-beam evaporation. A further layer of PR was used on Ti to define the mask pattern by photolihography. The sample was finally ready for RIE. First the Ti layer, then the bottom PR layer was etched. Ti layer was etched in pure Cl_2 . Without taking the sample out, the previous process gas was pumped out of the chamber and base pressure was let to drop down to $1.0 - 1.5 \cdot 10^{-6}$ Torr. O_2 was introduced into the chamber to etch PR. As a result the waveguide pattern was composed of 2.0 μm PR followed by 0.2 μm Ti layer just before the RIE of the crystal (Fig. 3.10).

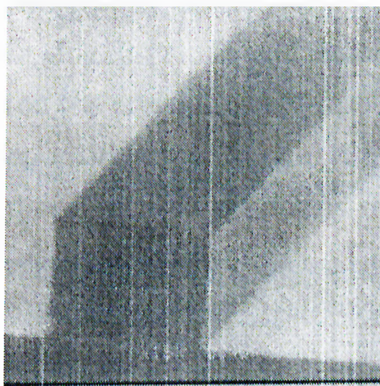

Figure 3.10: Photoresist Covered with Ti prior to RIE of the Rib

Although the pattern definition was much better and the sidewalls were straight with a Ti/PR mask, we faced another problem. The metal mask was getting sputtered on to the entire surface of the wafer. The small Ti particles spread on the crystal surface, resulted in a very interesting, yet destructive etch surface. The surface was named to be grassy (Fig. 3.11).

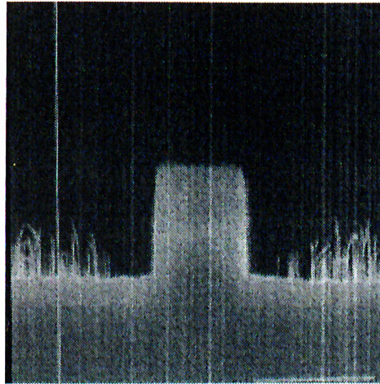

Figure 3.11: Grass Formation

Another idea was to use SiO_2 layer in the place of Ti. The SiO_2 layer was deposited on to the crystal surface directly. The photolithography was done over the SiO_2 and etched by CF_4 gas. The resulting mask was composed of SiO_2 + PR. After that, $Al_xGa_{1-x}As$ layers were RIE etched with CCl_2F_2 gas. But this method did not provide any better results. The etched crystal surface roughness was unacceptable (Fig. 3.12). In addition to this, we experienced one more interesting formation on the crystal surface : polymer deposition (Fig.3.13). The evidence of polymer deposition while the use of freons such as CCl_2F_2 under certain plasma conditions, has been also previously reported.[28]

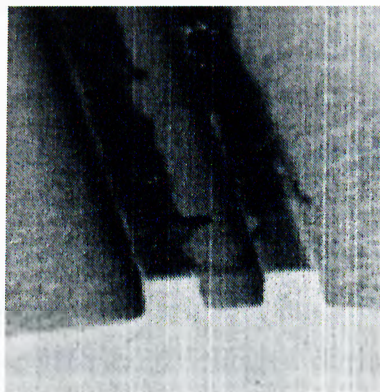

Figure 3.12: Rough Etched Surface

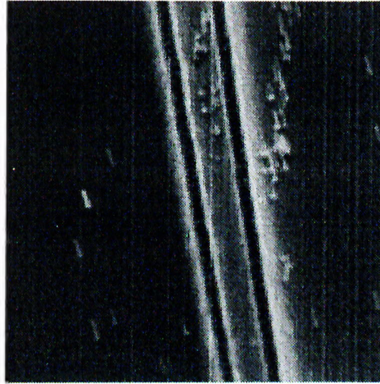

Figure 3.13: Polymer Deposition during RIE

From Figs. 3.5 to 3.13, it can be deduced that stabilization of RIE recipes needs long run times, many pieces of the same crystal to be able to characterize every aspect of RIE, and effort. The recipe that worked best in etching our waveguides is the following. Photolithography was performed with a thick PR - i.e. AZ 4210. After the exposure and development of the PR, sample was post-baked on a 200^0C hot-plate for 5 minutes. Next, it was loaded in the RIE chamber and the chamber was evacuated. For an ideal process, we have waited for the base pressure to drop down below $1.5 \cdot 10^{-6}$ Torr. Then 30 sccm BCl_3 and 20 sccm $SiCl_4$ gases were let into the chamber. The electrode separation was set to 3.2 inches. The chamber pressure was set to 10 mTorr and 150 Watts of RF power was applied. The etch depth was monitored by an interferometric measurement tool.[25] A He-Ne laser was incident on the crystal surface and back-reflected such that the light resonated in crystal cavity. As the surface of the crystal was etched down, the cavity length changed, so that the Fabry-Perot resonances were observed. The outgoing light intensity was measured by a photodiode and the signal was plotted as a function of time. The interference pattern was previously simulated and followed during the etch. This way the etch process was stopped at the desired etch-depth. Fig. 3.14 and 3.15 are SEM micrographs of the etched waveguide profile and sidewalls. Figs. 3.16 and 3.17 display the simulated interference patterns of both WG1 and WG3, and Fig. 3.18 displays the monitored interference pattern of WG3.

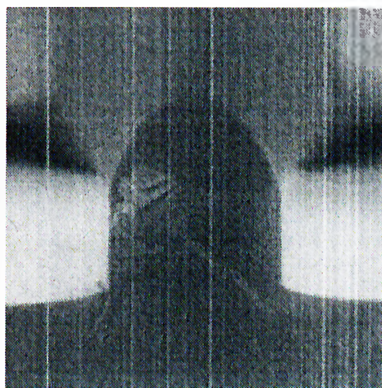

Figure 3.14: RIE Etched Waveguide Profile

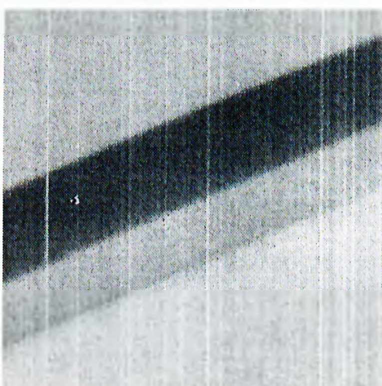

Figure 3.15: RIE Etched Waveguide Sidewalls

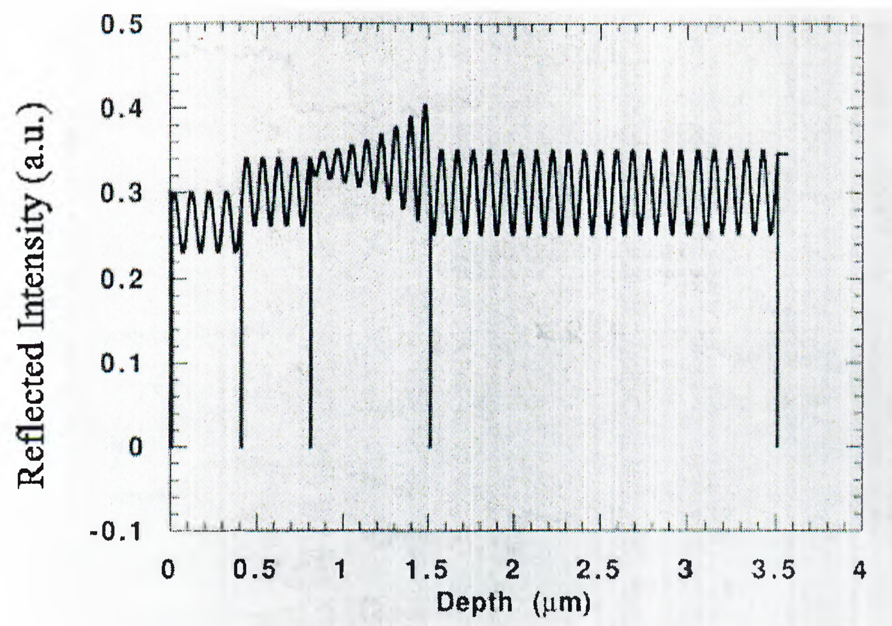

Figure 3.16: Simulation of RIE Interference Pattern for WG1

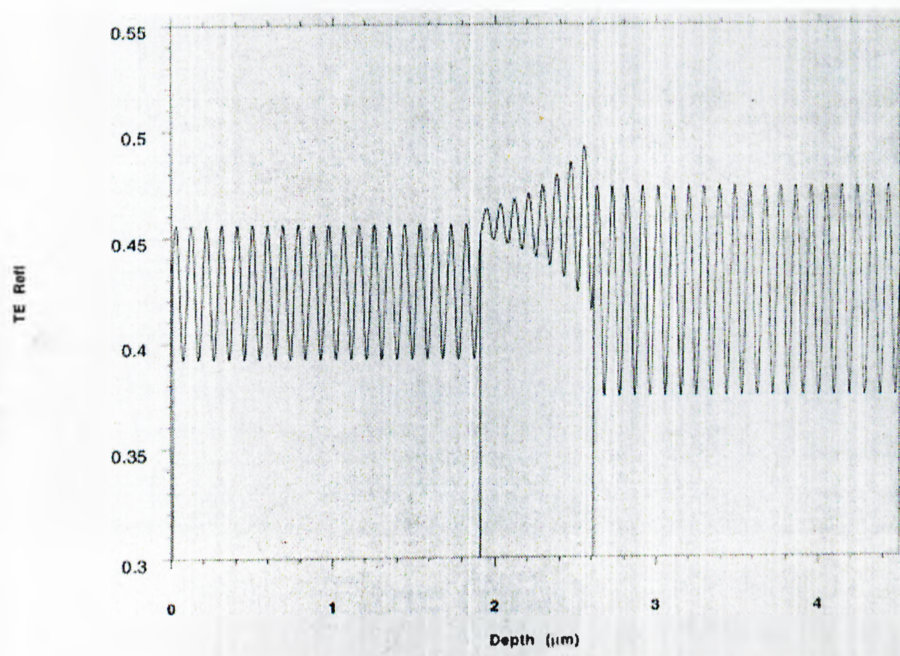

Figure 3.17: Simulation of RIE Interference Pattern for WG3

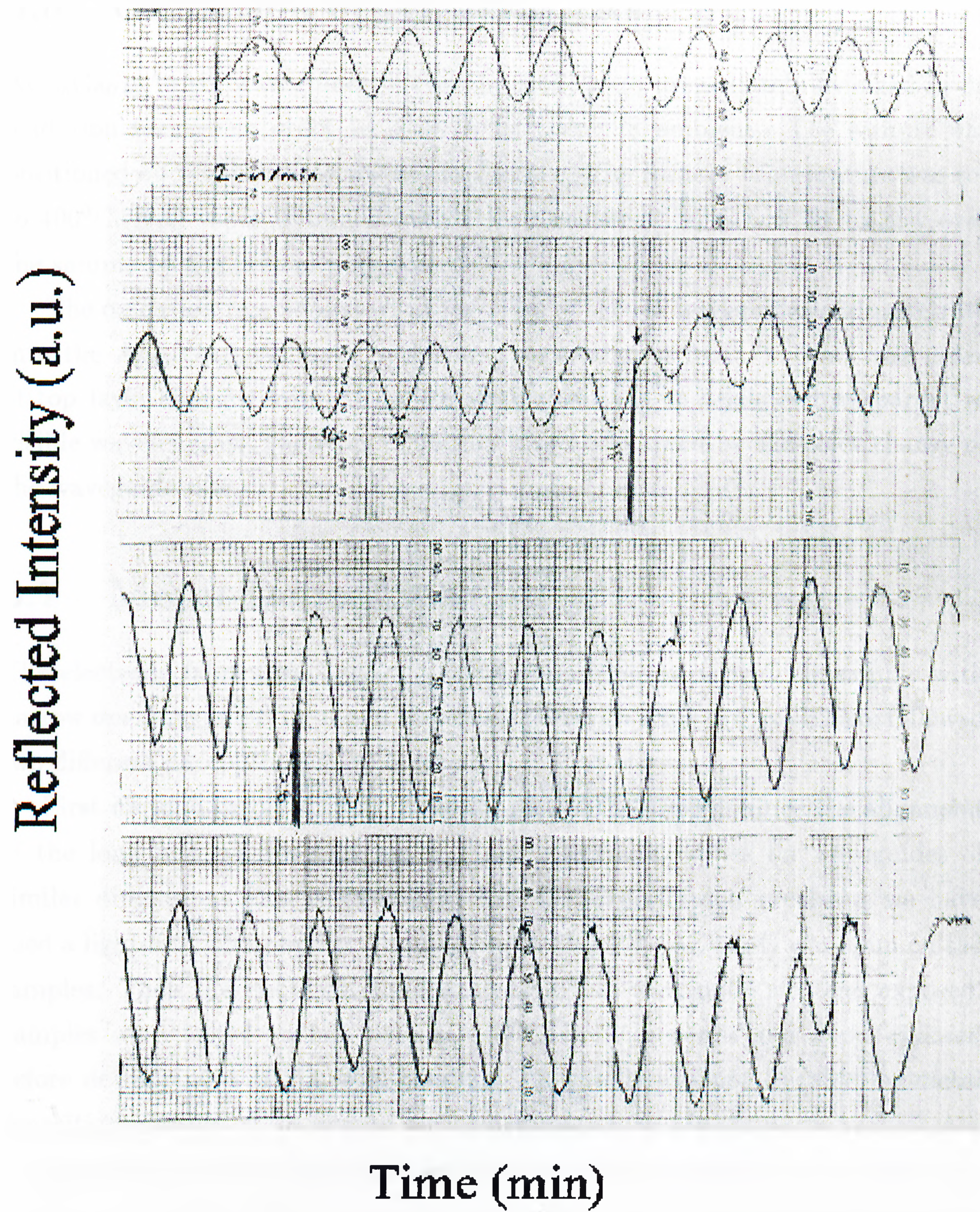

Figure 3.18: Monitored RIE Interference Pattern for WG3

3.6 Oxidation of $Al_{0.98}Ga_{0.02}As$

$Al_{0.98}Ga_{0.02}As$ rib waveguides, etched by RIE, were immediately oxidized in an oxidation furnace in order to prevent oxidation in ambient. The sample was positioned on a quartz tray inside the furnace. The furnace temperature was set to 400^0C. H_2O vapor obtained from a H_2O beaker at 80^0C was let to flow over the sample by the help of pure N_2.

The oxidation reactions start at the sides of the rib waveguides and penetrate into the $Al_{0.98}Ga_{0.02}As$ layer by forming an oxidation front.[29] Since the index of top layer changes from 2.9 to 1.6 after oxidation, it becomes transparent in visible wavelengths. Therefore oxidation may be followed by the color change of the waveguide ribs.

3.7 Metal Deposition

The electrode fabrication involved metal deposition on top of the sample with narrow openings of PR on top of the waveguides. To achieve this we have followed two different photolithography methods.

First method involved image reversal photolithography. Since the alignment of the long and narrow (1.4 cm x 2 μm) electrode stripes on waveguides of similar dimensions (1.4 cm x 4 μm) had to be performed precisely, we have used a light-field photomask. An image reversible PR (AZ 5214) was spun on the samples. Then the electrode mask was aligned on waveguide ribs and exposed. Samples were baked on hot-plate at 110^0C for 55 seconds and flood exposed before development of PR. The resultant PR profile was not suitable for metal deposition and lift-off, as can be seen schematically in Fig. 3.19.

Second method involved the standard dark-field photolithography. Before the development of the PR, the samples were submerged in toluene for 10 minutes. We have obtained PR profiles which were suitable for metal deposition (Fig. 3.20).

Metal deposition process is accomplished by an E-beam evaporator. The operation of e-beam evaporator involves a high vacuum system. The samples to

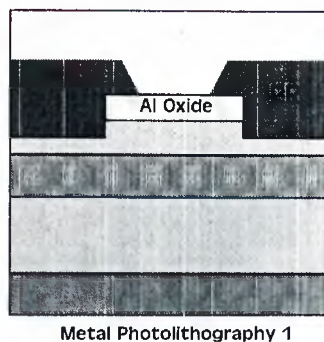

Figure 3.19: Photoresist Profile I

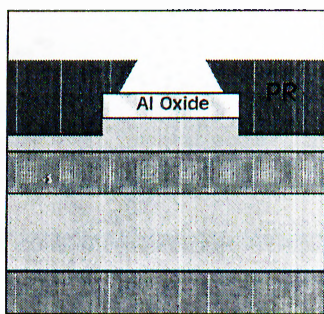

Figure 3.20: Photoresist Profile II

be metal deposited are clamped on a wafer tray and positioned facing down. The deposition thickness is monitored by a detector.

In our case we used three different types of metals : Ti, Pt, Au.
200Å Ti / 200Å Pt / 2000Å Au was deposited on the samples. Thin titanium layer was deposited for its better adhesive properties on semiconductor surface. Platinum provided a barrier for Au diffusion into the semiconductor. Gold was chosen as the main electrode material for its high conductivity.

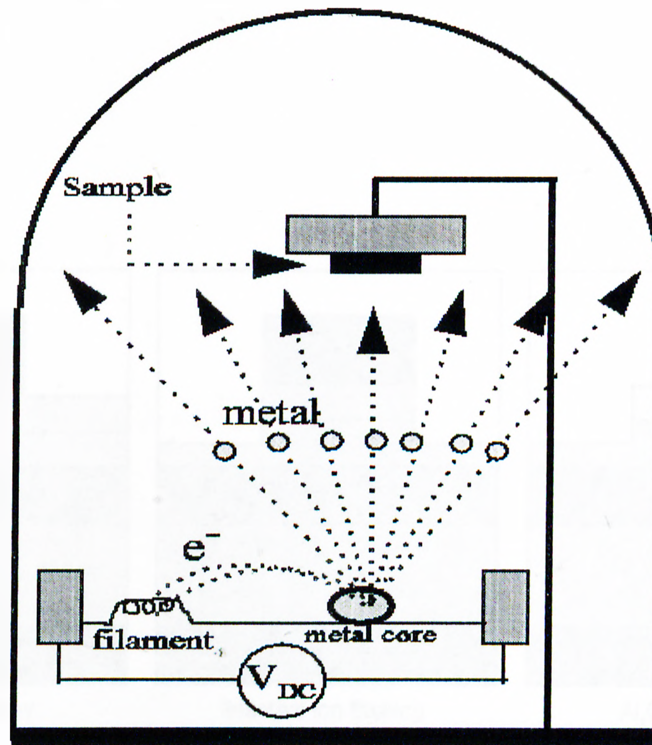

Figure 3.21: E-beam Evaporator

3.8 Lift-off

Metal deposits over the etched surface of the sample, thus the PR gets also covered with metal. In order to lift the unnecessary metal sheet off and clean the sample surface, we immersed the sample in ACE and stirred it overnight. Finally, three-solvent-cleaning of the samples were done before characterization.

Fig. 3.22 sketches the followed fabrication steps.

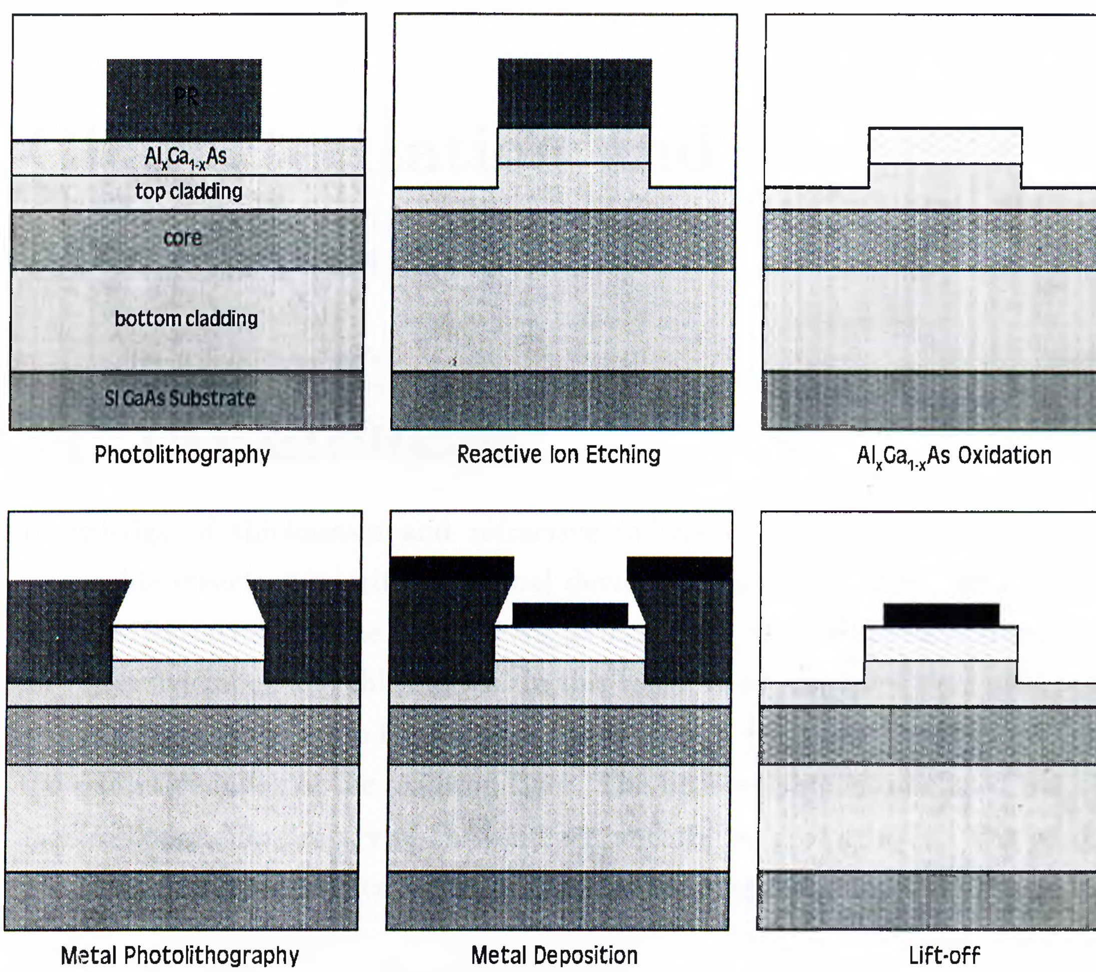

Figure 3.22: Schematic of Fabrication Steps

Chapter 4

Characterization and Measurements

4.1 Characterization

Knowledge of thicknesses and refractive indices of the layers in the optical waveguide structure is critical to final device performance. Thus, both the as-grown MBE layers and the oxidized $Al_{0.98}Ga_{0.02}As$ layers need to be characterized for refractive index and thicknesses. In this work, two techniques were used in an attempt to determine the thickness of the as-grown layers and the thickness and the refractive index of the oxidized layer. The first technique to be used was the spectroscopic ellipsometry of the oxidized and the as-grown layer. The second was in-situ RIE reflectance depth profiling of the as-grown materials.

4.1.1 Spectroscopic Ellipsometry

Spectroscopic ellipsometry[33,34] is a sensitive non destructive thin film measurement technique that uses polarized light. Ellipsometry measures the change in polarization state of light reflected from the surface of the sample, and that information is used to extract the optical constants and thicknesses of the layers under consideration. Ellipsometry works best for film characterization when the

film thickness is not too much smaller or larger than the wavelength of the light used for the measurement. Also roughness features on the sample surface or at film interfaces should be less than $\sim 10\%$ of the probe beam wavelength for the ellipsometric analysis to be valid.

The typical configuration of the ellipsometer is as follows :
Source⇒Polarizer⇒Monochromator ⇒Chopper ⇒Sample⇒Continuously Rotating Analyzer⇒ Chopper⇒Detector

The light source should exhibit a constant output as a function of wavelength over a spectral range extending from UV to NIR. Polarizer should have a high extinction ratio. Monochromator can be a diffraction grating. Detector should be polarization insensitive and linear over a broad range of beam intensity and wavelength. In Fig. 4.1 the schematic of an ellipsometer is shown.

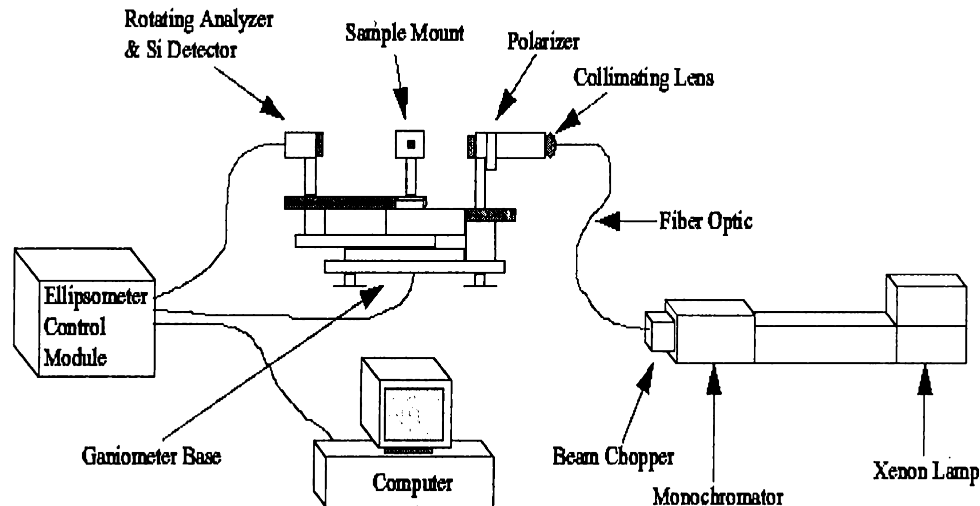

Figure 4.1: The Ellipsometer Instrument

The angle between plane of incidence and analyzer azimuth is variable and set by the user. When a linearly polarized beam enters a rotating analyzer, the detector will generate a periodic signal :

$$V(t) = a\sin(2\omega t)$$

The circularly polarized light would generate :

$$V(t) = DC$$

For elliptical polarization, the detected signal is a sinusoid with a DC offset of the form :

$$V(t) = DC + a\cos(2\omega t) + b\sin(2\omega t) \tag{4.1}$$

The two important quantities measured by the ellipsometer are α and β defined as :

$$\alpha = \frac{a}{DC} = \frac{\tan^2\Psi - \tan^2 P}{\tan^2\Psi + \tan^2 P} \tag{4.2}$$

$$\beta = \frac{b}{DC} = \frac{2\tan\Psi \cdot \cos\Delta \cdot \tan P}{\tan^2\Psi + \tan^2 P} \tag{4.3}$$

Ψ and Δ are the ellipsometric parameters that characterize the sample, and P is the input polarizer azimuth with respect to plane of incidence. The equations 4.2 and 4.3 can be inverted and, Ψ and Δ can be calculated as :

$$\Psi = \tan^{-1}\left(\sqrt{\frac{1+\alpha}{1-\alpha}}|\tan P|\right) \tag{4.4}$$

$$\Delta = \cos^{-1}\left(\frac{\beta}{\sqrt{1-\alpha^2}} \cdot \frac{\tan P}{|\tan P|}\right) \tag{4.5}$$

since the values α, β and P are known. There is no way of calculating the index of refraction and film thickness directly from Ψ and Δ, though the reverse is possible. With the approximate knowledge of n and t, it is possible to obtain these values for a given wavelength and angle of incidence, starting from the derivation of Fresnel reflection coefficients. Details of the fitting procedure is beyond the scope of this work. However, general procedure to obtain n and t of a thin film, is to calculate Ψ and Δ for expected values of n and t as a starting point and iterate the calculations till the deviation between calculated and measured data is small. In other words, it is possible to find the correct values by fitting to the experimental data.

Ellipsometry of as-grown wafers

Before the fabrication processes were applied on the wafers, they were 3-solvent cleaned and their ellipsometric measurements were done to confirm the thickness and x compositions of epi-layers. Starting from an initial model, data was fitted to the measured Ψ and Δ, in good agreement with most of the expected thicknesses and x compositions. One exception was the top cladding layer thickness of the second wafer. It was found to be 1.7 μm thick rather than 1.9 μm as was designed. Nevertheless this deviation was still tolerable to continue on fabrication, as computations showed. These ellipsometric data are shown in Figs. 4.2 and 4.3 for AlAs and thick top-cladding wafers respectively.

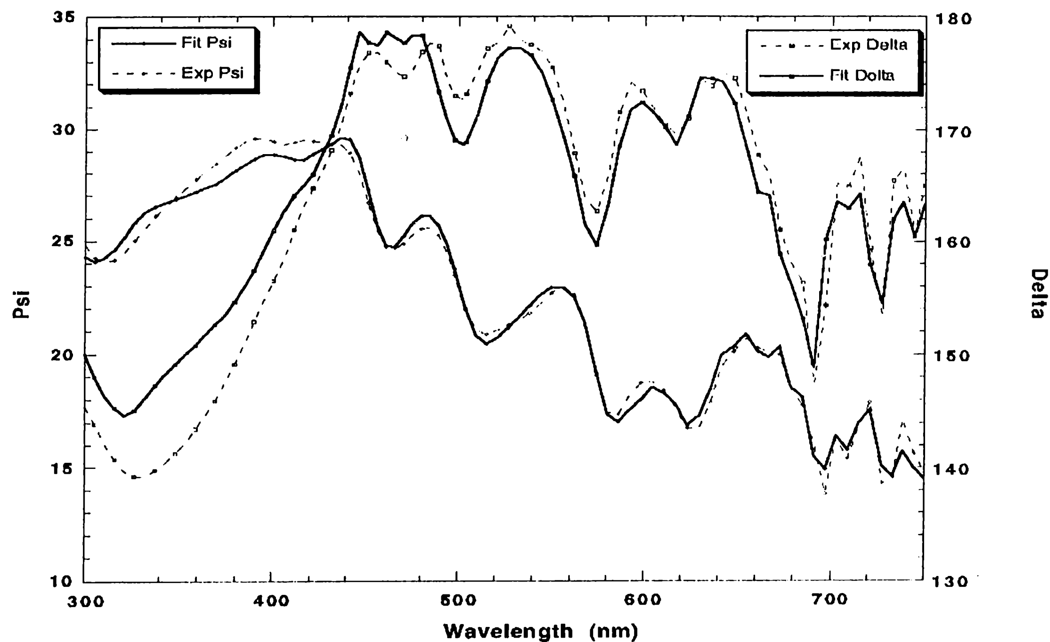

Figure 4.2: Ellipsometric Measurement of the AlAs Wafer

The extracted layer thicknesses and Al compositions of the grown wafers are listed in Tables 4.1 and 4.2.

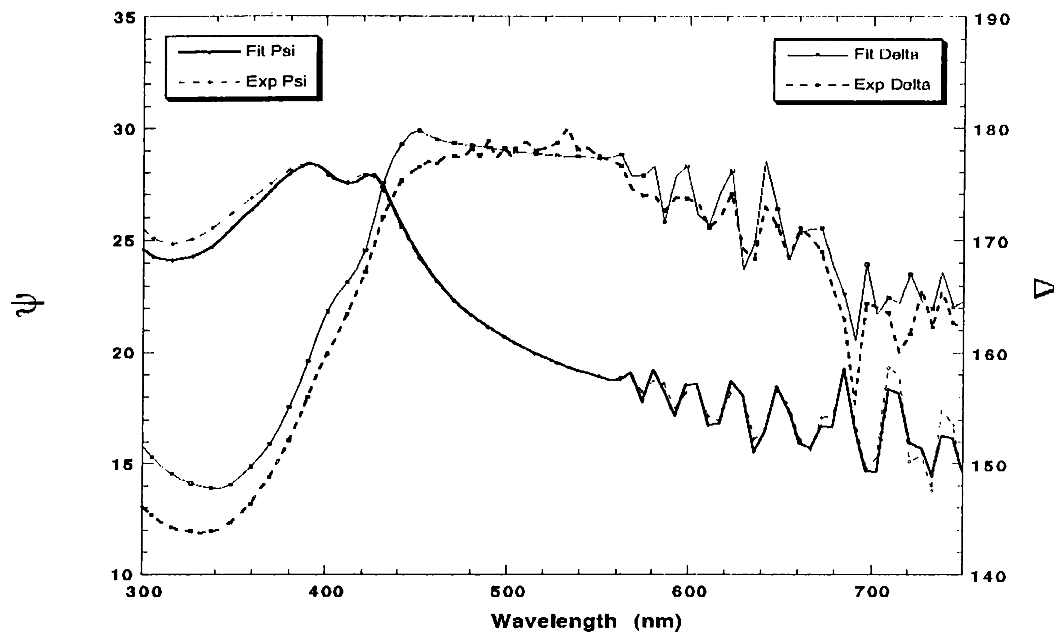

Figure 4.3: Ellipsometric Measurement of the Thick Top-cladding Wafer

GaAs		174 Å
AlGaAs	x=0.98	4151 Å
AlGaAs	x=0.60	4013 Å
AlGaAs	x=0.31	6584 Å
AlGaAs	x=0.60	19908 Å
GaAs		substrate

Table 4.1: The Ellipsometric Data of WG1 wafer

4.1.2 Oxide Characterization

Refractive index of oxidized AlAs is reported to be in the range of 1.54 - 1.8, and commonly assumed to be 1.6.[32] All of the data on the index of refraction of oxidized AlAs layers is measured at a single wavelength. By measuring the index of refraction in a wide range of values it is possible to extract the dispersion of the refractive index and extrapolate to wavelengths of interest such as 1.55 μm. As the index of refraction is an important quantity to be known in waveguide

GaAs		108 Å
AlGaAs	x=0.595	16719 Å
AlGaAs	x=0.31	6667 Å
AlGaAs	x=0.61	20568 Å
GaAs		substrate

Table 4.2: The Ellipsometric Data of WG3 wafer

design, we have decided to attempt to measure the index of refraction of oxidized AlAs.

However trying to position the ellipsometry probe beam on a waveguide rib of 4 μm width would be very difficult. The whole surface of a minimum of 1 cm x 1 cm wafer piece should be oxidized to get reliable ellipsometric data. A much larger area is clearly desirable, as light source in the ellipsometry setup can be apertured only down to 5 mm diameter. Furthermore, to simplify the analysis we decided to use a special sample with only a single layer of AlAs. This sample was nominally composed of 242 nm thick AlAs with a 10 nm GaAs cap to prevent ambient oxidation of AlAs layer. A 10 mm x 10 mm sample was cut from AlAs wafer. As it would take a very long time to oxidize a sample of this size, we have photolithografically defined 3 μm wide trenches with 100 μm wide AlAs mesas on the sample. RIE was used to etch the trenches. After removing the PR mask, sample was cleaved into 7-8 pieces and each piece was oxidized for a different duration. The lateral oxidation-front, developing in AlAs layer can be seen in Figs. 4.4 and 4.5.

Lateral oxidation of AlAs from the edges of the wafer was studied before.[29-31] The maximum oxidation-front propagation was reported to be about 100 μm wide. Lateral oxidation is also possible for $Al_xGa_{1-x}As$ films having x not necessarily exactly equal to 1. The propagation time of the oxide-front depends on x. As can be guessed the oxidation time increases sharply for decreasing x. We demonstrate this dependence in Fig. 4.6, using oxidation of several samples for different oxidation durations.

The knowledge of time dependence of oxidation-front propagation was also

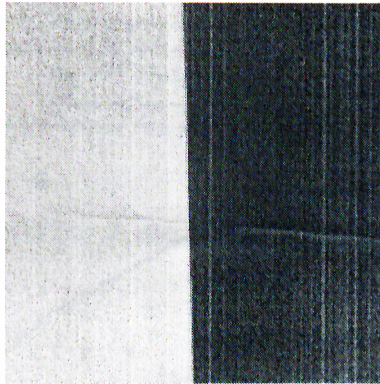

Figure 4.4: Microscope View of AlAs Wafer Edge Oxidized for 20 Minutes
The wafer edge is the interface between the dark and light regions. The bright stripe by the edge is 16 μm wide Al oxide.

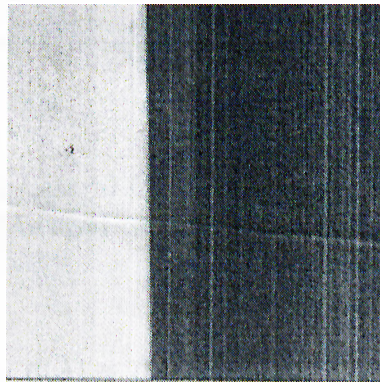

Figure 4.5: Microscope View of AlAs Wafer Edge Oxidized for 60 Minutes
The oxidation front propagates laterally into the AlAs layer. The stripe width is 38 μm.

essential in determination of the time required for the oxidation of waveguides. Unnecessarily long times in the oxidation furnace may result in partial oxidation of other layers in the waveguide structure, which is undesirable.

The final sample for spectroscopic ellipsometry was oxidized at 400^0C for 90 minutes and spectroscopic ellipsometry of both the as-grown and oxidized samples were done. In addition, a single layer of 2300 Å thick AlAs with a 100 Å GaAs cap layer, on GaAs substrate was oxidized. Oxidized AlAs (AlOx) was modeled using Cauchy parameterization which is widely used for transparent solids, where

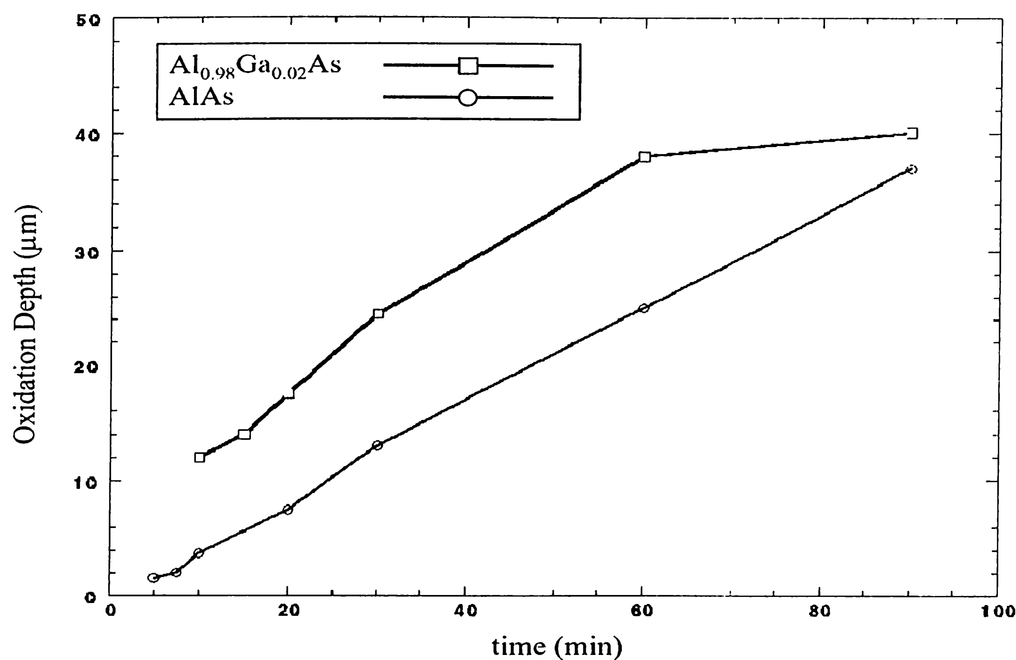

Figure 4.6: Lateral Oxidation Depth versus Time
Note that pure AlAs layer oxidizes faster than $Al_{0.98}Ga_{0.02}As$ layer.

$$n(\lambda) = A + \frac{B}{\lambda^2} + \frac{C}{\lambda^4} + \ldots \tag{4.6}$$

As the AlOx layers are reported to be transparent in the visible range of electromagnetic spectrum, no absorption edge was introduced into the Cauchy model. The modeling of the as-grown sample was done using well known refractive indices of GaAs, AlAs and GaAs oxide. The results for as-grown sample are given in Table 4.3.

GaAsOx	17 Å
GaAs	101 Å
AlAs	2201 Å
GaAs	substrate
Total Thickness	2319 Å

Table 4.3: Ellipsometric Measured Thicknesses of AlAs

The top most layer is a native oxide layer. In the case of AlOx layer, the used fit routine gave consistently worse results when GaAs cap and/or GaAs oxide layer were included in the model. We propose that the GaAs cap layer is fully oxidized and intermixed with the underlying AlOx. The refractive index obtained from the Cauchy model as in Eqn. 4.6 is given as a function of wavelength in Fig. 4.7 with the Cauchy coefficients in Table 4.4.

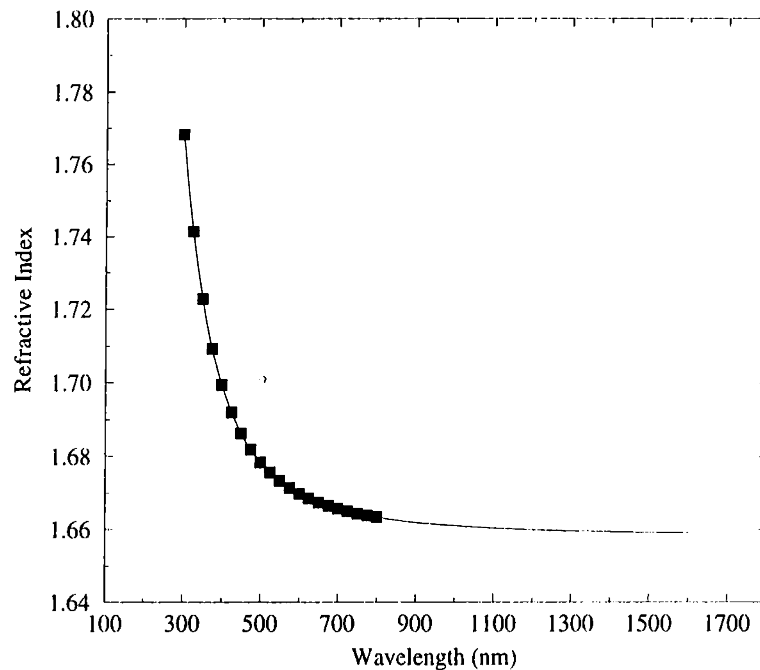

Figure 4.7: Refractive Index of Oxidized AlAs

A	1.6581
B	$2.371 \cdot 10^{-3}$
C	$6.787 \cdot 10^{-4}$
Thickness	2099 Å

Table 4.4: Cauchy Coefficients for AlOx

These results are in very good agreement with the design parameters. This is the first time spectroscopic ellipsometry was done on AlOx layers. As can be seen, the dispersion of the data is quite small at long wavelengths and as is seen from the extrapolation in figure 4.7, n is relatively constant up to 1600 nm. Furthermore, comparison of the as-grown layer thickness with oxidized layer thickness shows a shrinkage of 9.5%. Due to a much smaller unit cell size, large shrinkages in the layer thickness expected for AlOx has not been experimentally observed. Our result is in reasonable agreement with the only measurement in the literature in which a 6.7% shrinkage is reported.[43]

4.1.3 RIE Depth Profiling

This characterization method is a destructive way to obtain information about the formation of the epitaxially grown layer thicknesses. Therefore, some pieces of the wafers have to be spared for RIE characterization. As previously mentioned, it was possible to follow modulated reflectance patterns in RIE for precise in situ control of the etch depth.

By etching an unpatterned, clean sample piece, preferably cleaved close to the center of wafer, all the way down to the substrate, we obtained the full reflectance character of our $Al_xGa_{1-x}As$ layers. Creating the same multi-layer model in a specially designed simulation program that plots the reflectance as a function of depth from the surface of crystal, we simulated this reflectance characteristic. The comparison of the two showed that WG1 wafer was as designed but WG3 wafer was not grown properly. The top cladding layer for WG3 wafer was measured to be about $1.7\mu m$ thick similar to the ellipsometric measurement (Figs. 3.17 and 3.18).

4.2 Measurements

4.2.1 Optical Propagation Loss Measurements

The fabricated waveguides were prepared for measurement by careful cleaving of the input and output facets. After that, they were attached on aluminum sample holder by crystal wax. The holders are designed specially in geometry and size in order to minimize any possible problem due to variety in sample size.

The Measurement System

Measurement setup consists of seven basic parts associated with relevant operating systems. First is the DFB Laser equipped with a temperature controller. The operating wavelength ranges from 1557.360 nm to 1557.710 nm with a peak intensity of 1.470, mW at 1557.500 nm. Operation wavelength is selected and tuned by the temperature controller. The second item is the fiber-optic cable carrying the laser output to the sample. Fiber cable supports single mode, such that most of the light intensity is confined at the fiber core of 8 μm diameter. One end of the fiber is integrated inside the DFB laser, and the other end is fixed on a translation stage near the sample holder by the help of a fiber-chuck. The third item is the 3-loop polarization controller. The laser output is linearly polarized with a high extinction ratio, If the fiber cable is not bent too much or stressed, it maintains the laser polarization. A 3-loop polarization controller is an intentionally bent fiber making three successive loops in a controlled fashion. This is used to rotate the initially TE polarized laser light to TM when needed. The fourth element in the setup are the high precision x-y-z translation stages on which a fiber chuck holder provides angular degree of freedom. These stages have to be finely tunable since the fiber core and the waveguide width are on the order of a few micrometers. The fifth element is the microscope lens. The choice of microscope lens should depend on the numerical aperture, in order to be able to collect most of the light coming out of the waveguide output facet. This is important; because the outgoing light

diverges too much, since the difference in the refractive index of air and effective index of waveguide is large as in our case. The sixth item is the polarizer. The polarizer should have an high extinction ratio to perform polarization dependent measurements accurately. The seventh and the last part describing the basic construction of measurement setup is the detector. A wide spectrum of detector types are used in our measurements. In measurements, involving fast detection of intensity modulation, high speed detectors like InGaAs photodiode were used. For cw measurements, Ge photodetectors were used. For alignment and mode shape visualization, we have used IR cameras connected to monitors. The IR camera images of a zeroth order and a first order waveguide mode can be seen in Figs. 4.8 and 4.9.

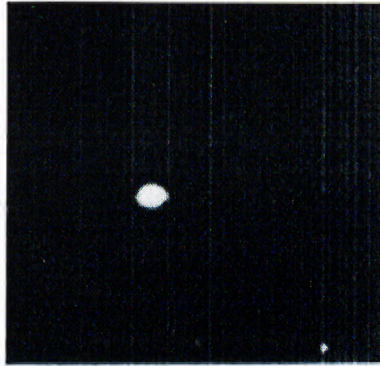

Figure 4.8: The Zeroth Order Mode of AlAs Waveguide

Figure 4.9: The First Order Mode of AlAs Waveguide

Other than those fundamental parts, we made use of some complimentary equipment. For the coarse alignment of the sample, a field microscope was attached on the optical table. Several lenses and neutral density filters were also used. The measurement area was kept free of stray light during data acquisition. A sketch of measurement setup is shown in figure 4.10.

Results of Loss Measurements

Loss measurements are performed by the use of Fabry-Perot resonances technique at multiple waveguide lengths. This way, the facet reflectivities are measured directly along with the loss coefficients rather than assuming a predicted or calculated value. The loss values of 15 different waveguides of the same length

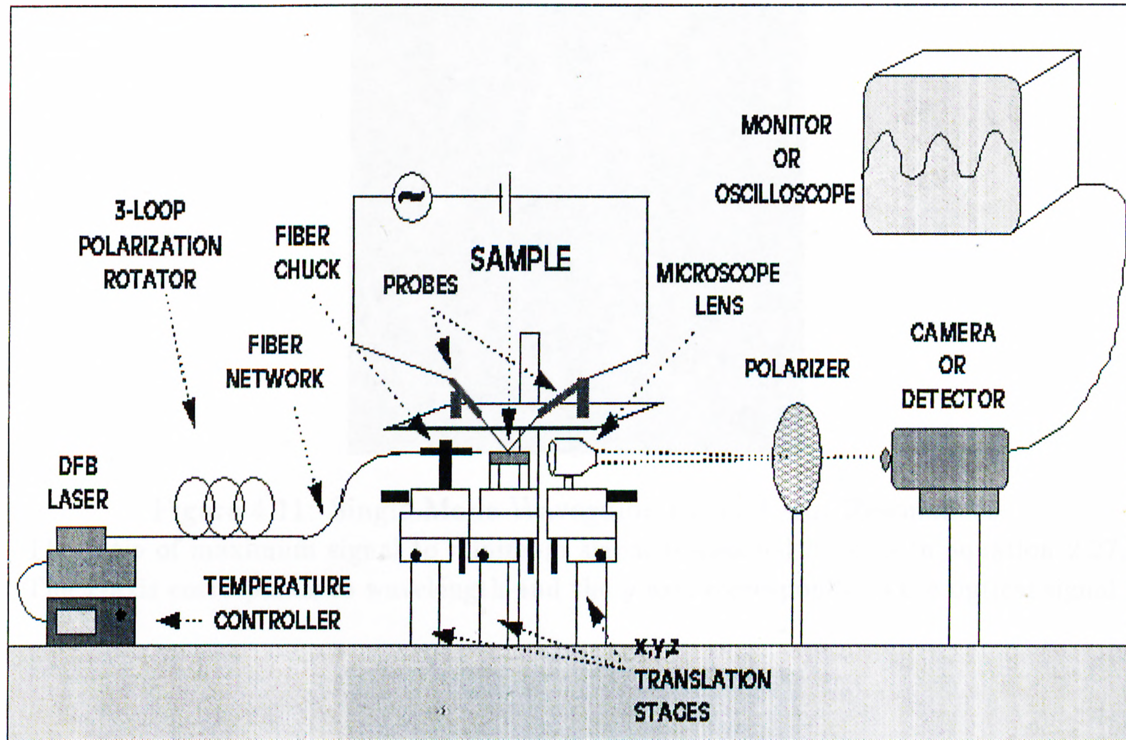

Figure 4.10: Loss Measurement Setup

on the same sample were averaged. Figs. 4.11 and 4.12 show the Fabry-Perot resonances of a single mode and a double mode waveguide.[10]

Waveguides composed of three kinds of configurations were examined in loss measurements. These are : 400 nm $Al_{0.98}Ga_{0.02}As$/400 nm $Al_{0.61}Ga_{0.39}As$ top cladding waveguides (WG1), 400 nm $Al_{0.98}Ga_{0.02}As$ oxide/$Al_{0.61}Ga_{0.39}As$ top cladding waveguides (WG2) and 1700 nm $Al_{0.61}Ga_{0.39}As$ top-cladding waveguides (WG3).

WG1 waveguides were not oxidized before metal deposition, thus they are susceptible to oxidation in air unless the waveguides are covered with a protective isolation layer to keep $Al_{0.98}Ga_{0.02}As$ layer away from forming native oxide in ambient. Therefore, we have chosen benzocyclobutane (BCB) polymer to cover the sample, because it was durable, solid when cured, and had a low refractive index. The refractive indices of BCB and its photo-definable version

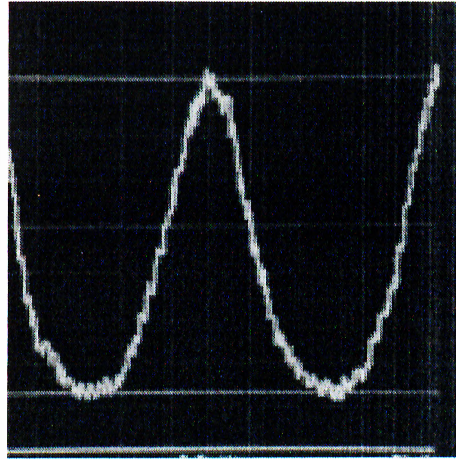

Figure 4.11: Single Mode Waveguide Fabry-Perot Resonances
The ratio of maximum signal to minimum signal is denoted by κ as in equation 2.27. The x-axis corresponds to wavelength and the y axis corresponds to the optical signal.

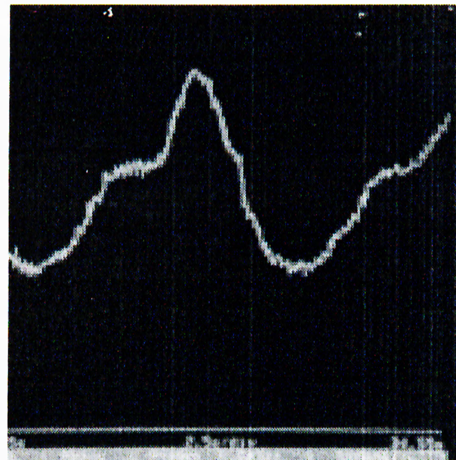

Figure 4.12: Double Mode Waveguide Fabry-Perot Resonances
The x-axis corresponds to wavelength and the y axis corresponds to the optical signal

PDBCB, were measured by ellipsometry and were found to be 1.5335 and 1.5365 respectively. These values are close to the refractive index of air with respect to waveguide effective index. Fig. 4.13 shows a cleaved facet of BCB covered WG1 waveguide.

BCB was spun on the sample like photoresist. Then it was cured in 200^0C oven

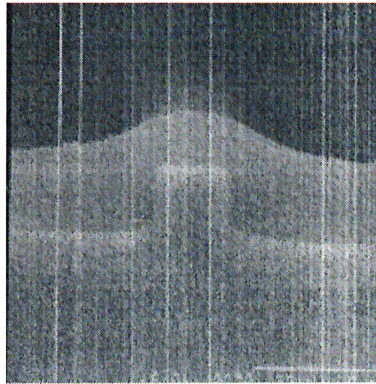

Figure 4.13: SEM Picture of a BCB Covered $Al_{0.98}Ga_{0.02}As$ Waveguide Rib
The rib width is 4 μm.

in nitrogen ambient overnight. The curing process resulted in a durable BCB on the sample. Finally, the sample was cleaved and mounted to the measurement setup.

After the total loss values were measured, the sample was cleaved into two different length pieces, and the measurements were repeated for these two unequal smaller length waveguides. The total loss was plotted as a function of waveguide length. The propagation loss coefficients for as-grown (WG1) waveguides were calculated to be 6.0 dB/cm for TM and 3.7 dB/cm for TE polarized light.

The oxidized waveguides (WG2), did not require the usage of BCB. They were cleaved after the metal deposition and lift-off processes. Following the same technique, the loss coefficients for oxidized waveguides were measured as 1.0 dB/cm for TM and 0.6 dB/cm for TE polarizations. Fig. 4.14 shows the experimental data and the linear fit to the data for WG1 and WG2 waveguides. The fit determines the facet reflectivities by extrapolating y-axis.

The difference of the loss coefficients for oxidized and as-grown samples can be easily distinguished by noting the slopes of the linear fits in the figure.

The loss measurements of deep-etched waveguides with a thick top-cladding (WG3), also yielded lower loss values than the WG1 waveguides, as expected. The measured TM loss coefficient was 2.1 dB/cm and TE loss coefficient was 1.5 dB/cm, still being twice as higher than the oxidized waveguide loss coefficients.

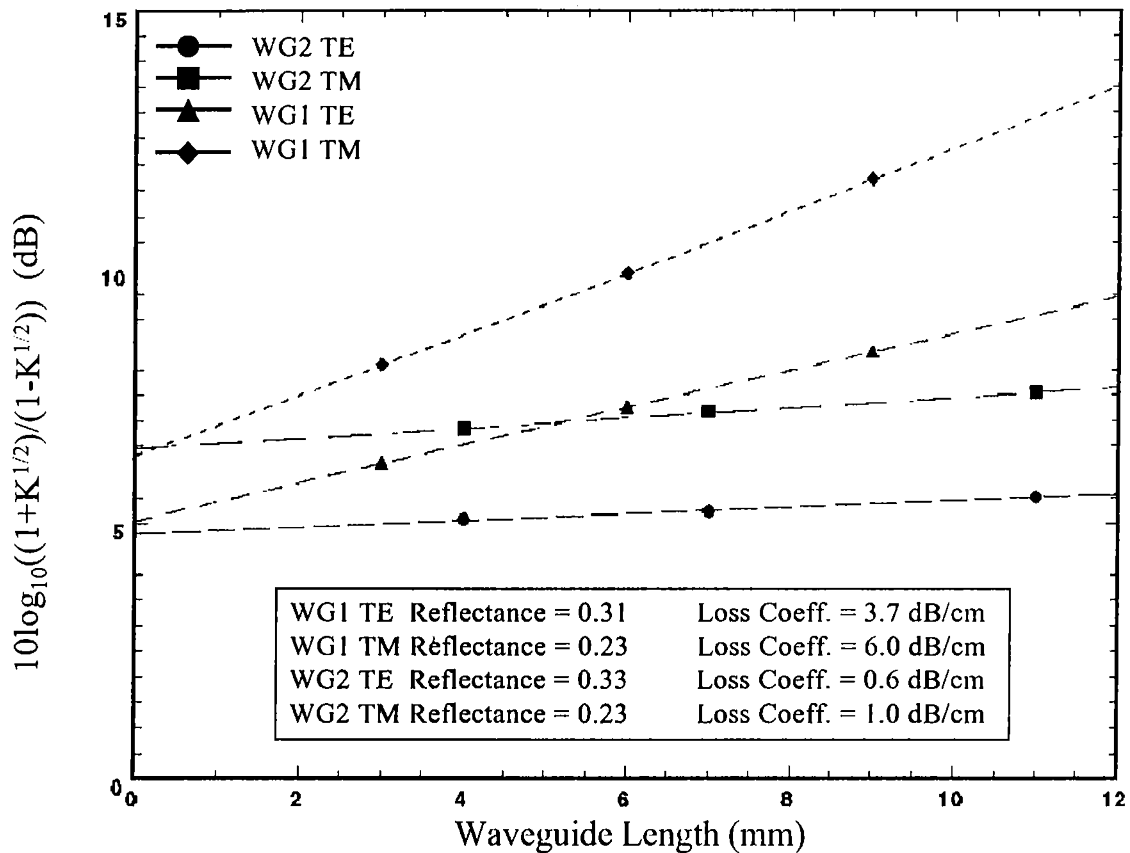

Figure 4.14: The Loss Coefficients and Facet Reflectivities of WG1 and WG2 Waveguides

The measured loss data is displayed in Fig. 4.15. Thus, increasing the top cladding thickness to 1.7 μm reduces the loss by a factor of 3 for TM mode, introduction of a much thinner but lower index material such as AlOx reduces the TM mode loss by a factor of 6. This is a major improvement over present waveguides. It is well known that, in general, RIE leaves behind a non negligible surface roughness. Fine tuning of various parameters such as gas composition, pressure, RF power are required to obtain acceptable smooth surfaces. The loss values obtained for TE and TM modes on WG2 shows that our RIE process produces very smooth surfaces.

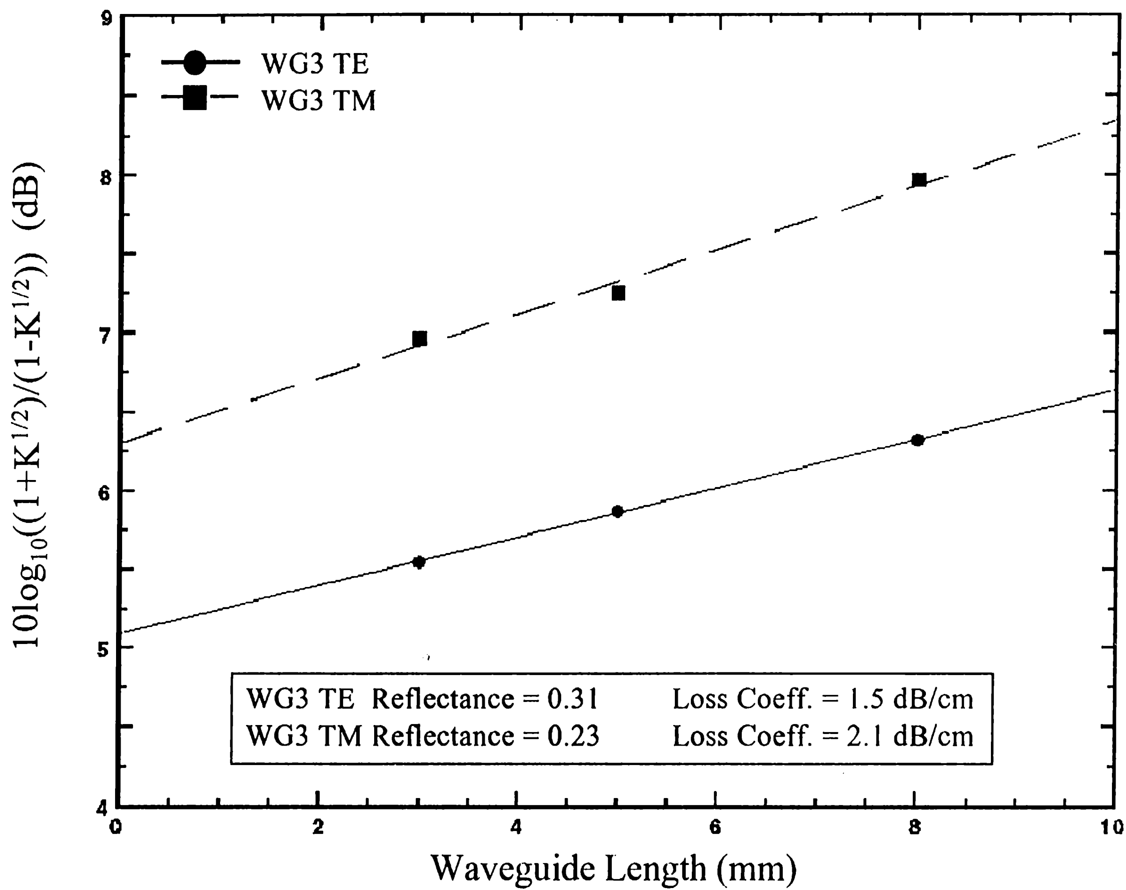

Figure 4.15: The Loss Coefficient and Facet Reflectivity of WG3 Waveguides

4.2.2 Characterization of Polarization Splitters

A major problem in integrated optics is the polarization control of light throughout an optical system. Polarization splitters are 2 x 2 devices that output different polarization states to different output ports. Thus, when either TE or TM polarized light is injected into an input port, TE and TM polarized light is output to separate output ports. However, even with perfect designs and the best of fabrication technologies tunability of the polarized light intensity at the output is found to be necessary to improve the extinction ratio. But, metal electrodes on the ribs of waveguides for application of tuning voltages induce excess propagation loss for TM mode and renders the device inoperable. Recent

advances on MOSFETs with thin oxidized $Al_xGa_{1-x}As$ layers as gate material offers the possibility of using oxidized $Al_xGa_{1-x}As$ layers in polarization splitters. However, thicknesses required to minimize TM loss is much greater than (by a factor of 8) those in MOSFETs and thus makes this application a challenge. We have therefore attempted to fabricate an optical coupler for polarization splitting using a previously designed mask to investigate the possibility of utilizing oxidized $Al_xGa_{1-x}As$ layers in polarization splitters for both active and passive operation.

The coupling length measurements were performed on the same setup that was used in loss measurements (Fig. 4.10). The beam from the coupler output ports was collected with a microscope lens and focused on the IR camera. The camera image was followed by a monitor connected to the camera. The fine alignment of the setup was accomplished by maximizing the image contrast on the monitor. The intensity of the optical field has been measured by a video image analyzer that produced an x-y cross on the monitor screen. The cross marks were positioned on the waveguide mode image on the monitor and the readings were recorded. The following photographs show the optical field coming from the ports of a waveguide which is, totally coupled to the left-hand side waveguide of the coupler (Fig. 4.16), half-way coupled (Fig. 4.17) and back-coupled (Fig. 4.18).

TE or TM polarized light is launched from either one of the input ports of the coupler and polarized light intensity at both output ports are measured. For both polarizations the ratio of the light intensity at one of the ports to the total light intensity from both ports is plotted as a function of straight coupling section length. The power transfer function (Eqn. 4.7) based on coupled mode theory is least squares fitted to the data as in Figs. 4.19 and 4.20, and parameterized as :

$$\frac{I_{cross}}{I_{total}} = \sin^2\left(\frac{l}{L_c}\right) \tag{4.7}$$

where I_{cross} is the optical field intensity measured at output port opposite to the insertion port, I_{total} is the total intensity at both output ports, L_c is the coupling length and l is the straight section length of the coupler.

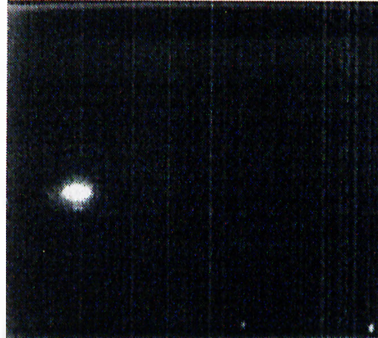

Figure 4.16: Optical Field Output at the Left Output Port

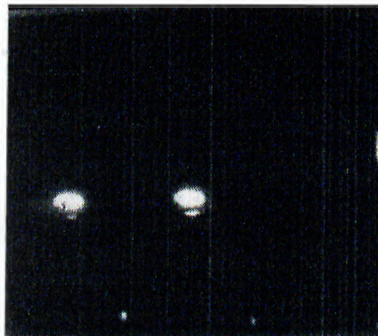

Figure 4.17: Optical Field Half-and-half at Both Output Ports
Separation between the two output ports is 32 μm on the sample, and 4 cm on the monitor

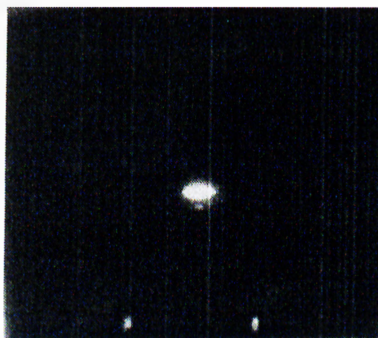

Figure 4.18: Optical Field Output at the Right Output Port

The measured coupling ratio data of WG2 for two different waveguide gaps are shown in Figs. 4.19 and 4.20. Also the coupling lengths that were extracted from

the least squares fit to coupling ratio data of WG2 is plotted in Fig. 4.21. The coupling length ratios for WG2 polarization splitters, determined experimentally and simulated with effective index and BPM methods, are given in Table 4.5 for comparison. The experimental and theoretical results are in good agreement.

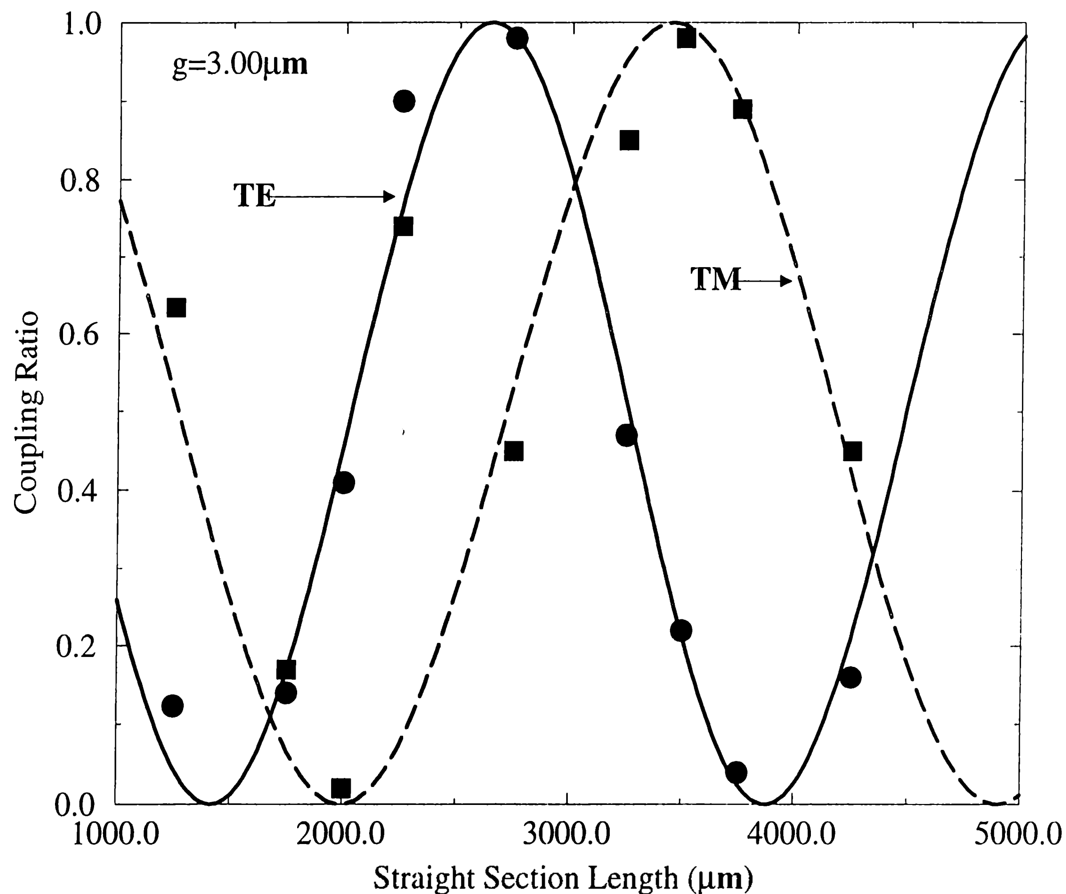

Figure 4.19: Coupling Ratio of WG2 Polarization Splitter for gap = $3.00\mu m$

The measured TM/TE extinction ratios are 12.4 dB for a gap of 3.00 μm between the straight section of the waveguides and 7.5 dB for a gap of 3.25 μm. Further analysis of gap = 3.25 μm coupling ratio data shows that with straight section lengths of approximately 4750 μm, extinction ratios as high as 20 dB

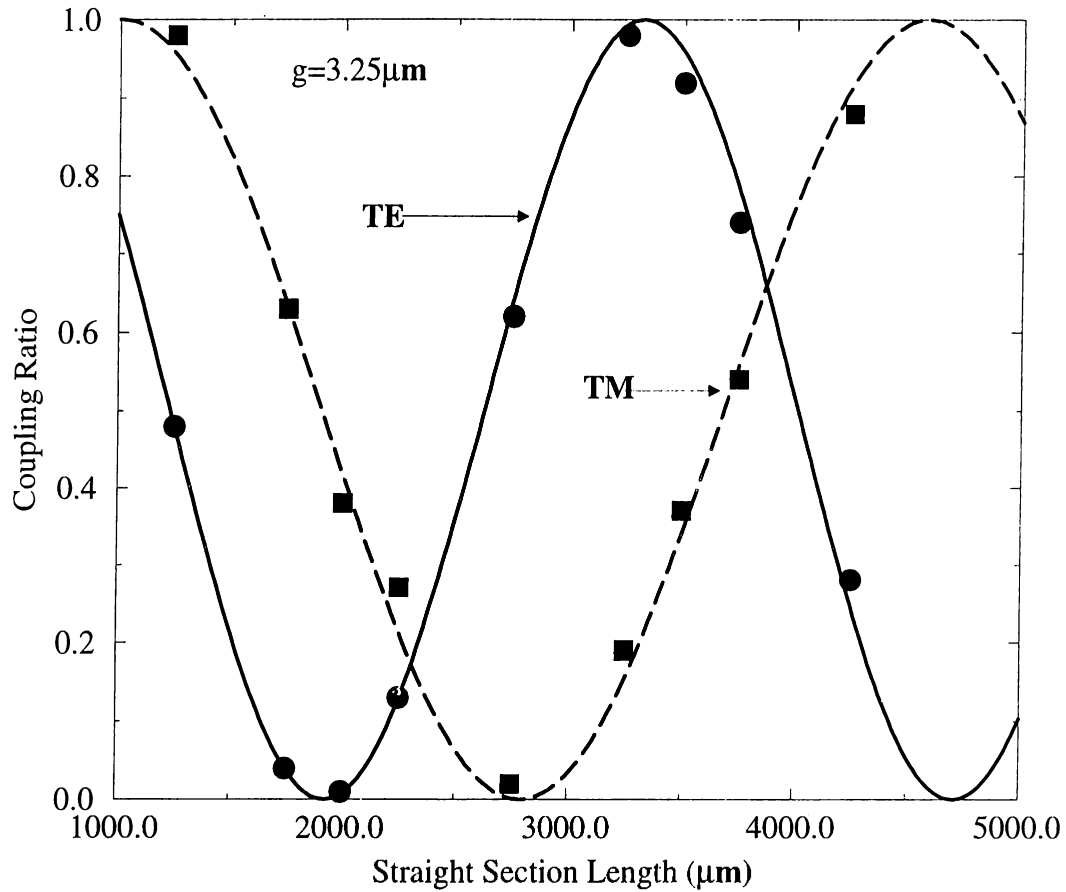

Figure 4.20: Coupling Ratio of WG2 Polarization Splitter for gap = $3.25\mu m$

Gap	3.00 μm	3.25 μm	3.50 μm
Experiment	1.27	1.20	1.14
Effective Index	1.29	1.24	1.20
Beam Propagation	1.30	1.26	1.22

Table 4.5: Coupling Length Ratios of WG2 Determined by Experiment, Effective Index Method, and BPM

are possible. TE/TM (TM/TE) extinction ratio is a measure of how well the polarization splitting is achieved by the device. This value can significantly be increased by optimizing the straight section length of the coupler and the gap (g) in between the waveguides of the coupler. The other way is to tune the TE (TM)

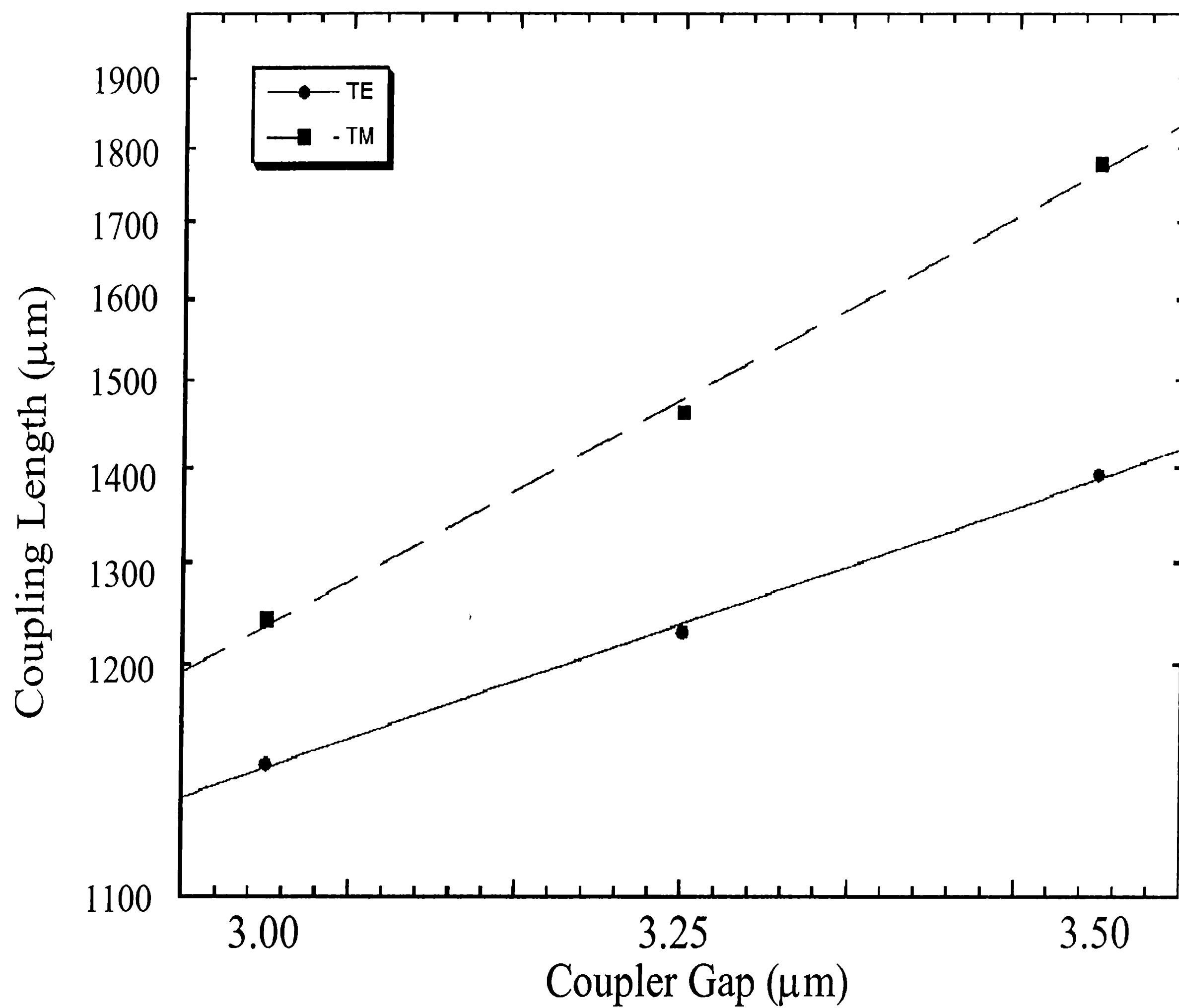

Figure 4.21: Coupling Lengths of WG2 Polarization Splitters

transfer function by applying voltage between the electrodes of the waveguides.

4.2.3 AC and DC Bias Measurements

In order to test the possibility of applying bias voltages through the oxidized $Al_xGa_{1-x}As$ top cladding layers, WG2 type polarization splitters were biased with both DC and AC voltages. Before applying any voltage to the electrodes, I-V characterization of the MOS contacts were done, and reverse breakdown

voltages larger than 45 Volts were obtained. The high contact quality enabled us to apply voltages larger up to 60 V.

Unfortunately, we were not able to create any change in the TE/TM (TM/TE) extinction ratio by applying DC voltages to WG2 type polarization splitters. This was probably due to large amount of charge still remaining at the interface of oxidized $Al_xGa_{1-x}As$ which screened the applied field. Oxidation of $Al_xGa_{1-x}As$ produces Al_2O_3 as well as several other byproducts, including elemental As.[32] While it is assumed that part of the As reacts to form AsH_3 which is volatile, significant amounts may remain in the material depending on exact oxidation conditions. Previous work on MOSFETs with thin (50 nm) layers of oxidized $Al_xGa_{1-x}As$ suggests that low (400^0C) oxidation temperatures improve MOSFET characteristics. With this in mind, we oxidized our samples at 400^0C for 10 minutes. However, the results were not positive. Arsenic is a well known donor atom and excess arsenic is known to pin the Fermi level at GaAs Schottky diodes. Furthermore, while AlO_x preserves its crystallografic nature, several other byproducts such as As_2O_3, Ga_2O and their hydroxides as well as the voids that form both in and at the $AlO_x/Al_{0.61}Ga_{0.39}As$ interface may cause Fermi Level pinning preventing DC modulation of the polarization splitter. Considering that the thickness of the oxidized layer is much larger than those used in MOSFET, optimization of the oxidation process, perhaps followed by post oxidation treatments may be necessary. Hydrogen plasma treatments, vacuum annealing may be feasible approaches and needs to be explored further.

We have, however, attempted to improve oxidized AlGaAs layer quality by oxidizing it for much longer times in the hopes of providing enough time for reaction byproducts such as AsH_3 to out diffuse and eliminate much of the elemental and oxidized As. Thus, a separate polarization splitter sample was oxidized for 75 minutes at 400^0C. This sample showed signs of oxidation of underlying $Al_{0.61}Ga_{0.39}As$ as well but did not perform any differently.

We have applied AC bias of maximum 40 V (p-p) at frequencies from 1 kHz to 100 kHz. We were able to modulate the TE polarized light by 10% at 10 kHz up to 100 kHz. Light modulation by applied electric field can be seen in figures 4.22

and 4.23. The light intensity modulation[35] is in phase with the applied voltage at one output port, where it is out of phase at the other port. This shows the TE transfer from one waveguide to the other was enhanced by the applied field.

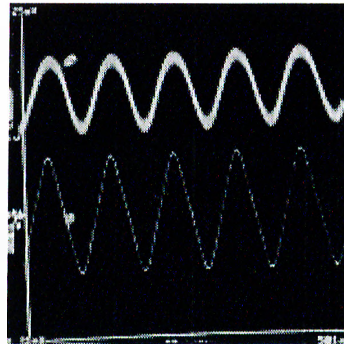

Figure 4.22: TE Modulation at One Output Port of the Waveguide
The upper curve in the figure corresponds to optical signal and the lower curve corresponds to applied voltage. The x-axis corresponds to time and y-axis corresponds to optical signal. Note that the optical signal and the applied voltage are in phase.

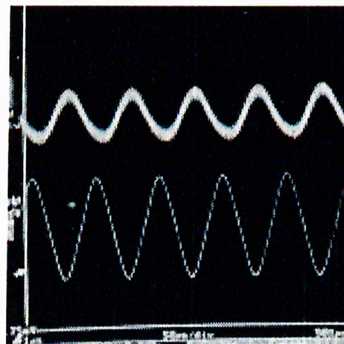

Figure 4.23: TE Modulation at the Other Output Port of the Waveguide
The x-axis corresponds to time and y-axis corresponds to optical signal. Note that they are out of phase.

Chapter 5

Conclusions

A major aim of this work was to reduce excess propagation loss of the TM mode of an optical rib waveguide due to metal electrodes. In this work two approaches were explored. One in which the thickness of the top cladding layer was dramatically increased (WG3). The other, where a low index material (AlOx) was introduced as part of the top cladding layer (WG2). As a part of the second method, the index and the thickness of the as-grown wafers, and the AlOx wafer, were determined by spectroscopic ellipsometry. The spectroscopic ellipsometry evaluation of as-grown waveguide wafers were, in a sense, a control of the nominal growth parameters. Spectroscopic ellipsometry along with RIE depth profiling provided crucial information on the amount of the material to be etched in order to maintain single mode operation. Spectroscopic ellipsometry also provided critical data on the dispersion of the refractive index of AlOx and the resulting shrinkage after the oxidation step. It is found that the Cauchy model gave a slowly varying index of refraction throughout most of the visible and near infrared region of the EM spectrum. The index of refraction of AlOx at 1.55 μm has been taken as 1.66 which is in close agreement with previous measurements at 632 nm. The obtained shrinkage percentage (9.5%) is larger than the only available data (6.7%). The small discrepancy may be attributed to different sample preparation conditions.

The propagation loss of existing $Al_xGa_{1-x}As$ optical waveguides with metal

electrodes have been significantly reduced particularly for TM polarized state of light. We have found that the TE mode optical loss is also reduced further. Comparison of the loss measurement results for all these waveguides yields interesting insight into the benefits of the AlOx layer in waveguide operation. The loss values for waveguide taken as standard (WG1) were 6.0 dB/cm and 3.7 dB/cm for TM and TE modes respectively. While some of this loss is due to RIE induced sidewall roughness, the difference in loss between different polarizations clearly indicates the excess metal induced loss. Increasing the top cladding layer (WG3) decreases these numbers significantly down to 2.1 dB/cm and 1.5 dB/cm for TM and TE polarizations. Assuming that the TE mode is mostly isolated from the metal electrode (confirmed by 1-D finite difference simulations), we attribute most of the loss for TE polarization to sidewall roughness. While the difference between different polarizations shows that, even when the top cladding layers is as thick as 1.7 μm, a residual excess TM loss due to metal electrode remains. The simulated data for loss coefficients for TE and TM modes were consistently smaller than the measured values since the simulations do not include the loss due to scattering from imperfections.

The comparison between the measurement results for unoxidized and oxidized waveguides demonstrate how powerful our idea works. The TE loss coefficient drops to 0.6 dB/cm from 3.7 dB/cm which means a total of 3.1 dB/cm reduction, whereas the TM loss coefficient drops to 1.0 dB/cm from 6.0 dB/cm meaning a 5.0 dB/cm reduction. Obviously, the isolation of optical field from the electrodes by inserting an oxide layer blocks the absorption of field by the metal surface. This becomes particularly important for TM mode. There is one more interesting consequence of the oxide layer in WG2, that comes as a natural advantage over the other waveguides. When the optical field is quenched in top most oxide layer, the surface roughness experienced by the optical field also becomes ineffective. In contrast, in WG3 waveguides, the optical field distribution is nearly the same as WG1 waveguides (as opposed to WG2), resulting in higher propagation loss due to sidewall roughness of the rib. The higher loss (1.5 dB/cm, TE) observed in WG3 than that of WG2 (0.6 dB/cm, TE), can mostly be attributed to the

above fact.

The isolation of the metal electrodes on waveguides could also be possible by deposition of a low-index film on top of the guides such as SiO_2 but $Al_xGa_{1-x}As$ oxidation has many advantages over that method. The major advantage of $Al_xGa_{1-x}As$ oxidation with respect to low-index dielectric film deposition is the quality of fabrication. In the case of SiO_2 deposition, the interface between the low-index layer and the top cladding layer would be full of surface states which would not enable us to apply electric field through the core layers that carry most of the optical energy. However, the growth of $Al_{0.98}Ga_{0.02}As$ on $Al_{0.61}Ga_{0.39}As$ do not intrinsically suffer from interface states since they are lattice matched. Another advantage in insertion of $Al_{0.98}Ga_{0.02}As$ layer on the sample at the growth step is the reliability and the consistency of film quality. The results on MOSFET operation with the thin layers of gate AlOx layer is proof that it is possible to have high quality interfaces that support electric field application to the underlying semiconductor.

It should be noted that oxidized $Al_{0.98}Ga_{0.02}As$ thickness of $0.4\mu m$ used in this work is significantly higher than that in previous studies. Such thick layers of oxidized $Al_{0.98}Ga_{0.02}As$ are found to be crack free and resulted in very high quality waveguides as long as 1 - 2 cm. This is the first time such thick surface layers have been successfully oxidized and found to be mechanically stable. Nevertheless, $Al_{0.98}Ga_{0.02}As$ oxidation method has a disadvantage. If the Al concentration of the underlying $Al_xGa_{1-x}As$ layers are also high, during the oxidation of the top layer other layers will also get oxidized, which is not desired.

The polarization splitters exhibit some interesting properties. It is easy to visualize the polarization splitting strength (TE/TM or TM/TE extinction ratio), by diractly inspecting the coupling ratio versus straight section length plot. In our case, we have reached the maximum TE/TM extinction ratio at the output ports of the couplers as high as 12.4 dB for g=3.00 μm and 7.5 dB for g=3.25 μm. In fact, from the data for g=3.25 μm, we can extrapolate the extinction ratio to over 20 dB at $\sim$5000 μm for the straight section. Our intentions in fabricating polarization splitters were to investigate the effects of

AlOx on polarization splitter performance only. A polarization splitter with a higher extinction ratio can be designed such that the ratio of coupling lengths of TE and TM polarizations are $\frac{n}{n+1}$, where n is an integer. It should be noted that the optical field starts coupling to the neighboring guide at the curved sections, before it reaches the straight sections. Therefore, x-axis of the coupling ratio plots do not correspond to the actual coupling lengths. The values for the coupling length have been extracted from the fit coefficients to Eq. 4.7.

As shown earlier in Chapter 2, various design parameters effect the performance of a polarization splitter, such as lateral top cladding thickness, core thickness, and rib width. Parameters such as core thickness are fixed during the MBE growth process. On the other hand fabrication can induce uncertainty in the rib width and lateral top cladding thickness. In fact, we observed that on a 14 mm x 10 mm sample, variations on RIE etch depth as high as ± 50 nm were observed. We also found that surrounding the sample with blank pieces of clean GaAs reduces etch depth variations. While both the BPM and effective index calculations are in good agreement (Table. 4.3) with experimental values, uncertainties in all of the above parameters contribute to the difference.

Our results for DC voltage tuning of the polarization splitters were negative. This, we attribute to the charge still remaining in and at the interface of AlOx/$Al_{0.61}Ga_{0.39}As$. First, this result may seem unexpected in the face of recent MOSFET operations with thin AlOx layer. However, it should be kept in mind that the AlOx layer we employ, is almost eight times thicker with respect to those used in MOSFETs. Hence, it is plausible that further processing is required to improve interface characteristics. These treatments may include hydrogen plasma treatment and/or vacuum annealing. We believe that any improvement obtained by these treatments will also improve the modest result obtained in AC operation as well. However, in the light of our encouraging results, we conclude that utilization of $Al_xGa_{1-x}As$ (x=0.02) oxidation, provides significant reduction of metal induced loss coefficient in optical waveguides and opens the way for many optical devices, an example of which is the polarization splitter discussed in this work. Further work needs to be done to improve the electrical characteristics

of AlOx layers, and perhaps find ways to use thinner layers by clever choice of design parameters.

Bibliography

[1] R. G. Hunsperger, "Integrated Optics", Berlin: Springer-Verlag, (1995)

[2] R. März, "Integrated Optics", Boston: Artech House Publishers, (1994)

[3] H. P. Zappe, "Introduction to Semiconductor Integrated Optics", London: Artech House Publishers, (1995)

[4] A. R. Billings, "Optics, Optoelectronics and Photonics", New York: Prentice Hall, (1993)

[5] R. G. Hunsperger, "Photonic Devices and Systems", New York: Marcel Dekker, Inc., (1994)

[6] N. Bouadma, J. Liang, R. Levenson, S. Grosmaric, P. Boulet, S. Sainson, "Integration of a Laser Diode With a Polymer-Based Waveguide for Photonic Integrated Circuits", IEEE Photonics Technology Letters, **6**:10, (1994)

[7] R. Walker, "High-Speed III-V Semiconductor Intensity Modulators", IEEE Journal of Quantum Electronics, **27**:3, (1991)

[8] L. A. Coldren, S. W. Corzine, "Diode Lasers and Photonic Integrated Circuits", New York: John Wiley & Sons, Inc., (1995)

[9] E. Marom, O. G. Ramer, S. Ruschin, "Relation Between Normal-Mode and Coupled-Mode Analyses of Parallel Waveguides", IEEE Journal of Quantum Electronics, **QE-20**:12, (1984)

[10] H. Takeuchi, K. Oe, "Low-Loss Single-Mode GaAs/AlGaAs Miniature Optical Waveguides with Straight and Bending Structures", Journal of Lightwave Technology, **7**:7, (1989)

[11] Y. T. Byun, K. H. Park, S. H. Kim, S. S. Choi, T. K. Lim, "Single-mode GaAs/AlGaAs W waveguides with a low propagation loss", Applied Optics, **35**:6, (1996)

[12] Y. T. Byun, K. H. Park, S. H. Kim, S. S. Choi, T. K. Lim, "Efficient sigle-mode GaAs/AlGaAs W waveguide phase modulator with a low propagation loss", Applied Optics, **37**:3, (1998)

[13] R. J. Deri, M. A. Emanuel, "Consistent formula for the refractive index of $Al_xGa_{1-x}As$ below the band edge", J. Appl. Phys., **77**:1, (1995)

[14] Y. Chung, N. Dagli, "An Assessment of Finite Difference Beam Propagation Method", IEEE Journal of Quantum Electronics, **26**:8, (1990)

[15] Y. Chung, N. Dagli, "Analysis of Z-Invariant and Z-Variant Semiconductor Rib Waveguides by Explicit Finite Difference Beam Propagation Method with Nonuniform Mesh Configuration", IEEE Journal of Quantum Electronics, **27**:10, (1991)

[16] W. P. Huang, C. L. Xu, S. K. Chaudhuri, "Application of the Finite Difference Vector Beam Propagation Method to Directional Coupler Devices", IEEE Journal of Quantum Electronics, **28**:6, (1992)

[17] P. Sansonetti, E. C. Caquot, A. Carenco, "Design of Semiconductor Electrooptic Directional Coupler with the Beam Propagation Method", Journal of Lightwave Technology, **7**:2, (1989)

[18] W. P. Huang, C. L. Xu, "Simulation of Three Dimensional Optical Waveguides by a Full-Vector Beam Propagation Method", IEEE Journal of Quantum Electronics", **29**:10, (1993)

[19] R. G. Walker, "Simple and Accurate Loss Measurement Technique for Semiconductor Optical Waveguides", Electronics Letters, **21**:13, (1985)

[20] Y. T. Byun, K. H. Park, S. S. Choi, T. K. Lim, "Comparison of Propagation Loss of Single-Mode GaAs/AlGaAs Waveguides in a Three- and Five-Layer Structure", Jpn. J. Appl. Phys., **34**:2-8B, (1995)

[21] A. R. Sugg, E. I. Chen, N. Holonyak, Jr., K. C. Hsieh, J. E. Baker, N. Finnegan,"Effects of low-temperature annealing on the native oxide of $Al_xGa_{1-x}As$", J. Appl. Phys., **74**:6, (1993)

[22] R. C. Alferness, "Guided-Wave Devices for Optical Communication", IEEE Journal of Quantum Electronics, **QE-17**:6, (1981)

[23] H. J. Lee, M. S. Tse, K. Radhakrishnan, K. Prasad, J. Weng, S. F. Yoon, X. Zhou, H. S. Tan, S. K. Ting, Y. C. Leong, "Selective wet etching of a $GaAs/Al_xGa_{1-x}As$ heterostructure with citric acid-hydrogen peroxide solutions for pseudomorphic $GaAs/Al_xGa_{1-x}As/In_yGa_{1-y}As$ heterojunction field effect transister fabrication", Materials Science and Engineering B, **35**:230-233, (1995)

[24] M. A. Lieberman, A. J. Lichtenberg, "Principles of Plasma Discharges of Materials Processing", New York: John Wiley & Sons, Inc., (1994)

[25] G. A. Vawter, J. F. Klem, G. R. Hadley, S. H. Kravitz, "Highly accurate etching of ridge-waveguide directional couplers using *in situ* reflectance monitoring and periodic multilayers", Appl. Phys. Lett., **62**:1, (1993)

[26] Y. Z. Juang, Y. K. Su, S. C. Shei, B. C. Fang, "Comparing reactive ion etching of III-V compounds in $Cl_2/BCl_3/Ar$ and $CCl_2F_2/BCl_3/Ar$ discharges", J. Vac. Sci. Technol. A, **12**:1, (1994)

[27] D. E. Ibbotson, D. L. Flamm, V. M. Donnelly, "Crystallografic etching of GaAs with bromine and chlorine plasmas", J. Appl. Phys., **54**:10, (1983)

[28] Y. K. Su, Y. Z. Juang, S. C. Shei, B. C. Fang, "A Study of Selective and Nonselective Reactive Ion Etching of GaAs/AlGaAs Materials", Solid-State Electronics, **36**:12, (1993)

[29] M. Ochiai, G. E. Giudice, H. Temkin, J. W. Scott, T. M. Cockerill, "Kinetics of thermal oxidation of AlAs in water vapor", Appl. Phys. Lett., **68**:14, (1996)

[30] E. I. Chen, N. Holonyak, Jr., and S. A. Maranowski, "$Al_xGa_{1-x}As$-GaAs metal-oxide semiconductor field effect transistors formed by lateral water vapor oxidation of AlAs", Appl. Phys. Lett., **66**:20. (1995)

[31] A. Fiore, V. Berger, E. Rosencher, N. Laurent, S. Theilmann, N. Vodjdani, J. Nagle, "Huge birefringence in selectively oxidized GaAs/AlAs optical waveguides", Appl. Phys. Lett., **68**:10, (1996)

[32] E. F. Schubert, M. Passlack, M. Hong, J. Mannerts, R. L. Opila, L. N. Pfeiffer, K. W. West, C. G. Bethea, G. J. Zydzik, "Properties of Al_2O_3 optical coatings on GaAs produced by oxidation of epitaxial AlAs/GaAs films", Appl. Phys. Lett., **64**:22, (1994)

[33] C. M. Herzinger, H. Yao, P. G. Snyder, F. G. Celii, Y. C. Kao, B. Johns, J. A. Woollam, "Determination of AlAs optical constants by variable angle spectroscopic ellipsometry and a multisample analysis", J. Appl. Phys., **77**:9, (1995)

[34] WVase32 Software Manual, "A Short Course in Ellipsometry", Lincoln: J. A. Woollam Co., Inc., (1996)

[35] F. K. Reinhart, R. A. Logan, W. R. Sinclair, "Electrooptic Polarization Modulation in Multielectrode $Al_xGa_{1-x}As$ Rib Waveguides", IEEE Journal of Quantum Electronics, **QE-18**:4, (1982)

[36] R. C. Alferness, "Electrooptic Guided-Wave Device for General Polarization Transformations", IEEE Journal of Quantum Electronics, **QE-17**:6, (1981)

[37] L. B. Soldano, A. H. de Vreede, M. K. Smit, B. H. Verbeek, E. G. Metaal, F. H. Groen, "Mach-Zehnder Interferometer Polarization Splitter in InGaSaP/InP", IEEE Photonics Technology Letters, **6**:3, (1994)

[38] P. Granestrand, L. Thylen, B. Stoltz, "Polarization Independent Switch and Polarization Splitter Employing $\Delta\beta$ and $\Delta\kappa$ Modulation", Electronics Letters, **24**:18, (1988)

[39] F. J. Leonberger, C. O. Bozler, "GaAs directional-coupler switch with stepped $\Delta\beta$ reversal", Applied Physics Letters, **31**:3, (1977)

[40] H. Yanagawa, H. Mak, Y. Kamata, K. Ucki, "High Extinction Guided-Wave Optical Polarization Splitter", IEEE Photonics Technology Letters, **3**:1, (1991)

[41] J. P. van der Ziel, A. C. Gossard, "Absorption, refractive index, and birefringence of AlAs-GaAs monolayers", Journal of Applied Physics, **48**:7, (1977)

[42] F. K. Reinhart, R. A. Logan, "Interface Stress of $Al_xGa_{1-x}As/GaAs$ layer structures", J. Appl. Phys., **44**:7, (1973)

[43] R. D. Twesten, D. M. Follstaedt, K. D. Choquette, R. P.Schenider, Jr., "Microstructure of Laterally Oxidized $Al_xGa_{1-x}As$ Layers in Vertical Cavity Lasers", Appl. Phys. Lett., **69**:1, (1996)

[44] G. L. Li, R. B. Welstand, W. X. Chen, J. T. Zhu, S. A. Pappert, C. K. Sun, Y. Z. Liu, P. K. L. Yu, "Novel Bias Control of Electroabsorption Waveguide Modulator", IEEE Photonics Technology Letters, **10**:5, (1998)

[45] "CRC Handbook of Chemistry and Physics", D. E. Lide, Ed., Boca Raton: CRC Press, Inc., (1993)